Kinematics of active deformation and possible segmentation of seismic slip along the foothills of the Western Kunlun (China).

C. Guilbaud, Martine Simoes, J. van der Woerd, G. Baby, L. Barrier, H. Li, J. Pan

Kinematics of Active Deformation and Possible Segmentation of Seismic Slip along the Foothills of the Western Kunlun (China).

C. Guilbaud [1], M. Simoes [1], J. Van der Woerd [2], G. Baby [1,3], L. Barrier [1], H. Li [4,5], and J. Pan [4,5]

[1] Université Paris Cité, Institut de physique du globe de Paris, CNRS, F-75005 Paris, France
[2] Université de Strasbourg, CNRS, ENGESS, Institut Terre et Environnement de Strasbourg, UMR 7063, F-67000 Strasbourg, France.
[3] Physical Science and Engineering Division, King Abdullah University of Science and Technology, Thuwal, Saudi Arabia
[4] Key Laboratory of Continental Dynamics of Ministry of Natural Resources, Institute of Geology, Chinese Academy of Geological Sciences, 100037 Beijing, China
[5] Jiangsu Donghai Continental Deep Borehole Crustal Activity National Observation and Research Station, 222300 Jiangsu, China

Corresponding author: Martine Simoes (simoes@ipgp.fr)

Key Points:

- Slip rate on the blind footwall ramps beneath the Hotan anticline estimated to 1.2-2.8 mm/yr.
- Similar slip rate on the blind ramps all along the foothills, but possible structural and kinematic segmentation of active deformation.
- Moderate seismicity along the foothills, but possibly large rare earthquakes rupturing the wide frontal thrust sheet.

Abstract

The Tibetan Plateau stands as a prominent topographic feature at the Earth's surface, characterized by intense seismic activity, in particular along its bounding mountain ranges. To the northwest, the Western Kunlun Range has received increasing attention since the 2015 Pishan earthquake but its kinematics of deformation remain to be properly documented. Here, we analyse the terrace record of active deformation along the Karakash River, where it crosses the Hotan anticline. We date terraces using in-situ produced cosmogenic isotopes, and show that terrace incision and uplift are spatially correlated with blind duplex ramps beneath the anticline. From there, we quantify the slip rate of the overall duplex to be 1.2-2.8 mm/yr over the last ~250 kyr. Our data are not able to resolve the detailed kinematics on each blind ramp and we cannot exclude that several of them are active at places along the anticline. By comparing to available data, we propose that the system of blind structures all along the foothills of the Western Kunlun has an overall slip rate of ~2 mm/yr. However, the way this slip rate is partitioned on the various blind ramps is expected to vary along strike. The structural segmentation of the foothills may therefore explain the moderate recorded seismicity in this region. Because this slip is transmitted upward and forward onto the Mazar Tagh wide and geometrically simple frontal thrust sheet, we question the possibility of large – but rare – earthquakes rupturing this structure.

1 Introduction

The modern Tibetan Plateau results from the collision between India and Eurasia since the early Cenozoic (e.g. [*Allegre et al.*, 1984; *Kapp and DeCelles*, 2019]). Its building-up and deformation has stood as a great field case to better understand the mechanics of the continental lithosphere (e.g. [*England and Houseman*, 1989; *P. Tapponnier et al.*, 2001]), as well as earthquake mechanics as it features numerous major active faults and is a place of intense seismic activity. As such, numerous studies have attempted to quantify the kinematics of deformation of major continental faults, with particular attention on major strike-slip faults (e.g. [*Lacassin et al.*, 2004; *Meriaux et al.*, 2004; *Phillips and Searle*, 2007; *Replumaz et al.*, 2001; *Van Der Woerd et al.*, 2000; *P Z Zhang et al.*, 2007], among many others), but also on the mountain ranges forming the edges of the Plateau, such as the Himalayas to the south (e.g. [*Bollinger et al.*, 2006; *Lavé and Avouac*, 2000; *Long and Robinson*, 2021; *Yin and Harrison*, 2000], among many others), the Longmen Shan to the east (e.g. [*Hubbard and Shaw*, 2009; *Pitard et al.*, 2021; *Royden and al*, 1997]), and the Qilian Shan to the north-east (e.g. [*P Tapponnier et al.*, 1990; *Yin et al.*, 2008; *Zuza et al.*, 2016]). The 2001 Mw 7.8 Kokoxili (e.g., [*Lasserre et al.*, 2005; *Vallée et al.*, 2008]), the 2008 Mw 7.9 Wenchuan (e.g., [*Liu-Zeng et al.*, 2009; *X Xu et al.*, 2009]), and the 2015 Mw 7.8 Gorkha (e.g., [*Grandin et al.*, 2015; *Hubbard et al.*, 2016]) earthquakes are some recent examples of major earthquakes rupturing either one of these major continental strike-slip faults or the thrusts that support the mountain ranges bounding the Tibetan Plateau.

In contrast, the Western Kunlun Range, at the northwestern edge of the Plateau, has remained much less studied and the first-order tectonic framework still remains to be properly and consistently documented. The Western Kunlun forms a prominent topographic feature to the southwest of the Tarim Basin in its foreland (Figure 1). Modern deformation rates are hardly resolvable from geodesy [*Guilbaud et al.*, 2017; *H Wang et al.*, 2011] across this mountain range. Nonetheless, crustal-scale mass-balance and structural cross-sections, indicate at least ~70 km of Cenozoic shortening that were probably mostly accommodated by the blind structures all

along the foothills [*Baby et al.*, 2022; *Laborde et al.*, 2019]. Even though available published sections across these structures may not be all self-consistent and therefore directly comparable (e.g. [*Baby et al.*, 2022; *Guilbaud et al.*, 2017; *X Jiang et al.*, 2013; *Laborde et al.*, 2019; *Li et al.*, 2016; *Sun et al.*, 2019; *C-Y Wang et al.*, 2013]), lateral variations may exist with a pronounced decrease in Cenozoic crustal shortening to the east of the mountain range, from ~64 km down to ~35 km eastward at the longitude of the Hotan anticline [*Baby et al.*, 2022] (Figure 1) or even less at the eastern termination of the range, at the transition towards the Altyn Tagh strike-slip range [*Laborde et al.*, 2019]. In terms of recent active tectonics, only a couple attempts at quantifying the kinematics of active deformation across the mountain front from deformed young (Quaternary) geomorphic markers have been carried out since the 2015 Mw 6.4 Pishan earthquake [*Guilbaud et al.*, 2017; *J Xu et al.*, 2020]. They indicate a recent shortening rate of ~0.5 to 3.9 mm/yr over the last ~300 kyr, but these data remain limited to the epicentral area of the Pishan earthquake. Further east along the mountain front, significantly lower shortening rates of <0.5 mm/yr were deduced across the Hotan anticline over the last 8-9 Myr from structural cross-sections and growth strata analysis [*Baby et al.*, 2022]. Additional constraints are therefore needed to further enlarge our view on the recent kinematics of shortening all along the foothills of the Western Kunlun, and to better understand the seismic potential of this region [*Guilbaud et al.*, 2017].

Additionally, structural investigations suggest that slip on the blind thrust ramps forming the folds of the Western Kunlun foothills is transferred northward into the Tarim Basin, indicating that the deformation front of the range is located at the Mazar Tagh ridge, i.e., ~150-180 km north from the main topographic mountain front (e.g [*Baby et al.*, 2022; *Chen et al.*, 2022; *Guilbaud et al.*, 2017; *Laborde et al.*, 2019; *Lu et al.*, 2016; *Wittlinger et al.*, 2004] (Figure 1c). This extremely large frontal thrust sheet has a remarkably simple geometry, showing little to no internal deformation, above a ~4°S dipping decollement underlying the whole southwestern Tarim Basin. This clearly contrasts with the apparent structural segmentation of the mountain front, as deduced from the surface geology of the various folds forming the foothills (Figure 2). Together with recorded seismicity, deformed recent geomorphic features clearly indicate that the blind ramps forming the mountain front are active [*Ainscoe et al.*, 2017; *Guilbaud et al.*, 2017; *J Xu et al.*, 2020; *Y Zhang et al.*, 2023], and by structural and kinematic deduction, that this is also the case for the wide Mazar Tagh thrust sheet [*Guilbaud et al.*, 2017]. Given the dimensions and the structural simplicity of this structure (Figure 1c), potential large continental earthquakes with magnitudes M>8 could be suspected. A better quantification of possible lateral variations in shortening and slip rates on the various blind structures of the mountain front is expected to indirectly help better assess how much slip and slip rate is transmitted forward onto the Mazar Tagh thrust.

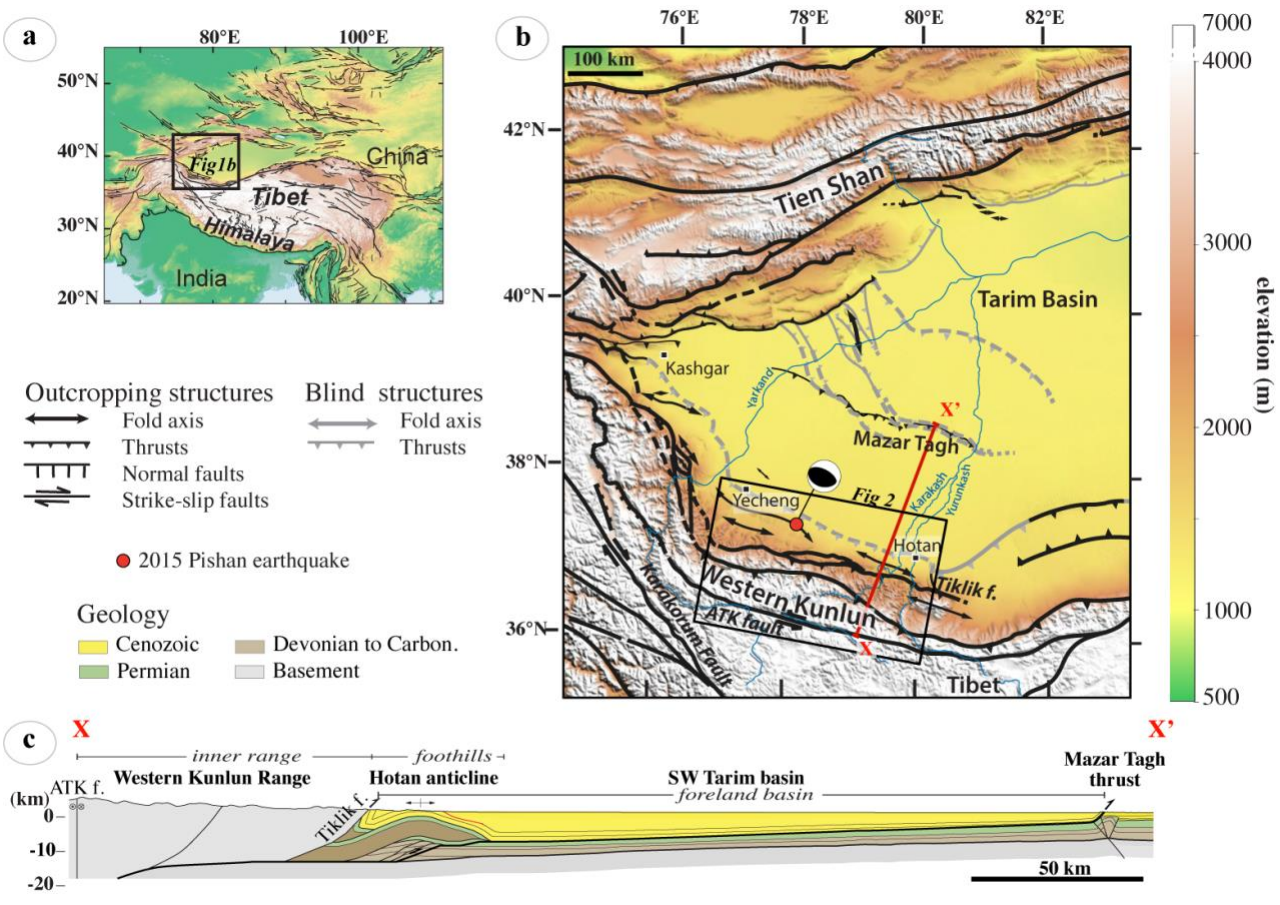

Figure 1. Location and structural context of the Western Kunlun Range. Topography is from the SRTM30 Digital Elevation Model. (a) General location in Asia, in the context of the Indo-Eurasian collision. Frame locates Figure 1b. (b) Topography and structural context of the Western Kunlun Range and southwestern Tarim Basin. The Western Kunlun Range overthrusts the southwestern rim of the Tarim Basin. Structural framework is taken from [*Laborde et al.*, 2019]. Frame locates the geological map of Figure 2. ATK Fault: Altyn-Tagh Karakash strike-slip fault; Tiklik F.: Tiklik thrust fault. (c) Geological cross-section across the Western Kunlun Range, at the level of the Hotan anticline (after [*Baby et al.*, 2022]). Section XX' is located on Figure 1b. The Western Kunlun Range extends from the Altyn-Tagh Karakash strike-slip fault to the south, to its deformation front at the Mazar Tagh thrust to the north. The Tiklik fault separates the inner range from the outer range and southwestern Tarim foreland basin [*Laborde et al.*, 2019]. The Hotan anticline is one of the structures of the foothills, in the outer range.

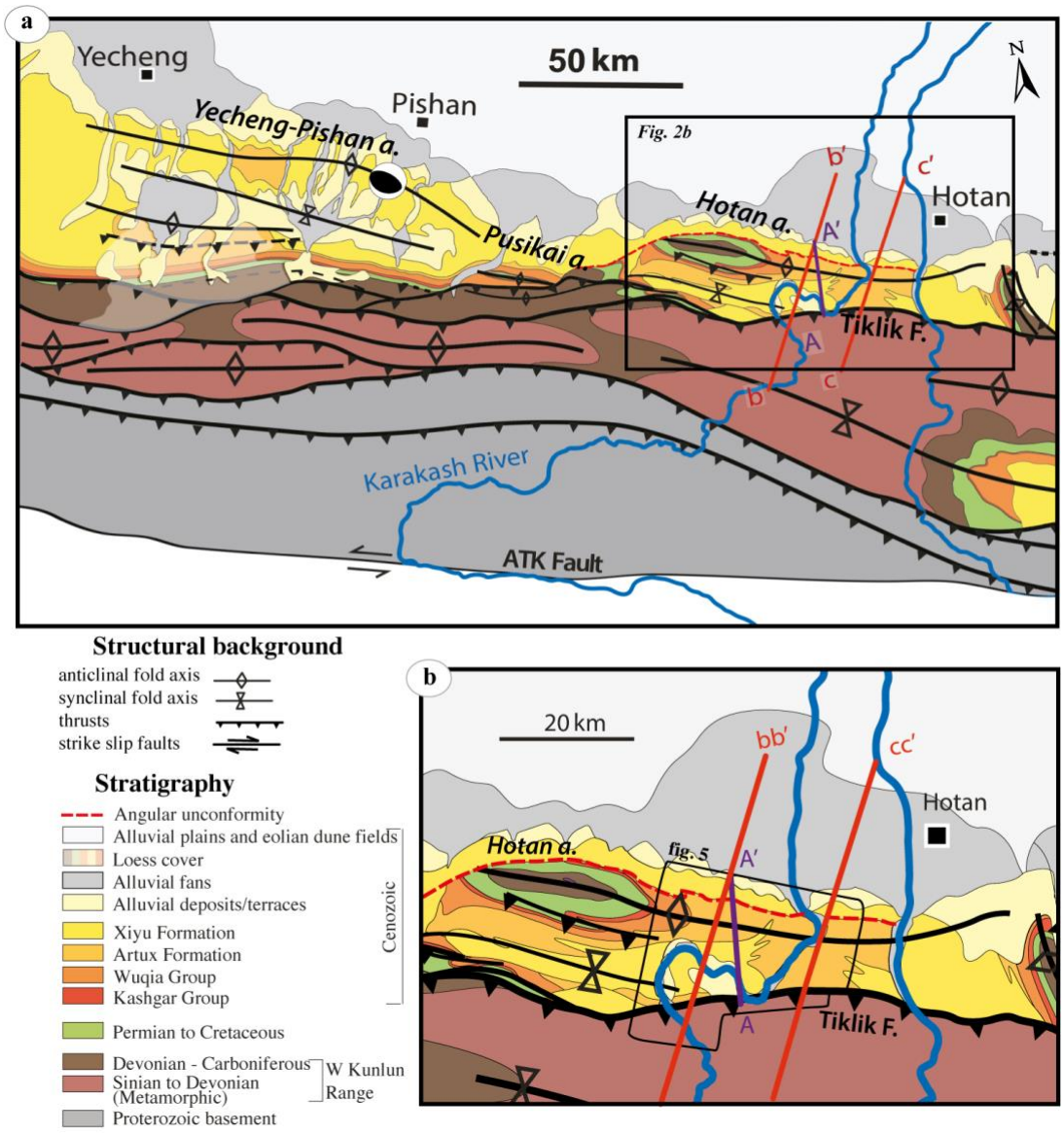

Figure 2. Geological map of the study area. (a) Geological map of the Western Kunlun inner and outer ranges (location reported on map of Figure 1b). The inner range is constituted of Proterozoic to Paleozoic metamorphic basement, and is separated from the outer range by the Tiklik fault (F.: fault). The outer range and the structure of its foothills encompass Permian to Cenozoic series, folded in a series of anticlines and synclines along the mountain front, such as the Yecheng-Pishan, Pusikai or Hotan anticlines (a.: anticline). Structural cross-sections bb' and cc' (after [*Baby et al.*, 2022]) (Figure 3) are located. ATK Fault: Altyn-Tagh Karakash fault. (b) Geological map of the Hotan anticline. The Hotan anticline shows a strong lateral variability as it exhumes and deforms variable stratigraphic levels, from the Cenozoic Xiyu formation to the east down to the Paleozoic to the west. The northern limb of the anticline is characterized by the presence of an erosional unconformity at the base of the Xiyu Formation. Section AA', on which our morphological observations are projected (Figure 6), is also reported. The polygonal frame locates the geomorphological map of Figure 5.

Here we propose to further explore these questions on the recent and potentially seismic deformation of the Western Kunlun Range by quantifying the recent slip rate on the blind ramps beneath the Hotan anticline. More precisely, we carry a morpho-tectonic analysis, in which we map, date and analyze the deformation recorded by fluvial terraces along the Karakash River where it flows out of the inner mountain range and crosses the anticline. By extension, this analysis is also applied to the nearby Tiklik thrust where a scarp has been evidenced in the field. From there, we quantify fault slip rates over the last ~250 kyr. These results are then compared to longer-term estimates and variations on these estimates inferred from structural geology across the Hotan anticline. They are also combined with existing data on recent fault slip rates from the Pishan area to complement our view on the kinematics of active deformation all along the Western Kunlun Range and southwestern Tarim Basin.

2 Geological and kinematic context

2.1 Geological setting

2.1.1 The Western Kunlun Range

The Western Kunlun Range is located along the southwestern edge of the Tarim Basin, and extends over ~700 km from Kashgar to Hotan (Xinjiang, China) (Figure 1). It is divided in two main segments of different orientations: 1) one trending approximately northwest-southeast to the west, between the cities of Kashgar and Yecheng, in structural and stratigraphic continuity with the northeastern Pamir Range, and 2) another segment trending approximately west-east to the east, between the cities of Yecheng and Hotan. Hereafter, we only focus on this latter portion of the Western Kunlun Range, where the deformation front has been described as extending far north into the Tarim Basin (e.g, [*Chen et al.*, 2022; *Guilbaud et al.*, 2017; *Laborde et al.*, 2019; *Lu et al.*, 2016; *Wittlinger et al.*, 2004]).

The Western Kunlun from Yecheng to Hotan presents very high elevations in the internal part of the range, with peaks reaching altitudes over 5000-6000 m. Altitudes drop to ~1200 m within the Tarim foreland basin. The Western Kunlun mountain range develops between the Altyn Tagh-Karakash strike-slip fault to the south, and the Mazar Tagh emerging frontal thrust ramp to the north (Figure 1c). North of the Karakash fault, the inner mountain range is composed of imbricates of a Paleo-Proterozoic metamorphic basement, separated by thrust faults proposed to root into a deep crustal decollement [*Laborde et al.*, 2019; *Matte et al.*, 1996; *Wittlinger et al.*, 2004]. Further north, the Tiklik fault separates the inner range from the outer range (Figure 1c). In the outer range, the Paleozoic to Cenozoic sedimentary cover of the Tarim Basin is deformed in a fold-and-thrust belt characterized by blind upper-crustal duplexes, as inferred from both seismic profiles and field observations [*Baby et al.*, 2022; *Guilbaud et al.*, 2017; *X Jiang et al.*, 2013; *Laborde et al.*, 2019; *Li et al.*, 2016; *Lu et al.*, 2016; *C-Y Wang et al.*, 2013]. The thrusts of these duplex stacks connect an intermediate decollement level located within Upper Cambrian gypsiferous shales to a shallower decollement within the Paleogene evaporitic series at the base of the Cenozoic sediments (e.g. [*Laborde et al.*, 2019]). This shallow decollement reaches the surface ~180 km farther north into the Tarim Basin, at the latitude of the Mazar Tagh emerging ramp, forming this way a uniquely wide frontal thrust sheet with little to no internal deformation (e.g., [*Chen et al.*, 2022; *Guilbaud et al.*, 2017; *Laborde et al.*, 2019; *Lu et al.*, 2016; *Wittlinger et al.*, 2004]) (Figure 1c).

The metamorphic Protero-Paleozoic basement of the inner range recorded the earlier complex deformation history of the region during the Ordovician and Silurian closure of the Proto-Tethys [*Matte et al.*, 1996; *Mattern and Schneider*, 2000]. In contrast, the outer range and Tarim Basin did not record this previous deformation episode, and is mostly constituted of a Proterozoic igneous basement overlain by Neoproterozoic to Paleozoic marine calcareous and terrigenous sediments (e.g., [*Laborde et al.*, 2019]). This difference in stratigraphy between the inner and outer ranges suggests that the localization of deformation along the present mountain front is at least partly controlled by inherited Paleozoic structures [*Baby et al.*, 2022; *Laborde et al.*, 2019].

Late Paleozoic to Cenozoic marine to continental sedimentary series characterize the sedimentary cover of the outer range (Figure 2). Cenozoic thicknesses reach up to ~9 km nearby Yecheng [*Metivier and Gaudemer*, 1997], as the sediments produced by the erosion of the Western Kunlun Range and other surrounding mountains have been trapped inside the subsiding endorheic Tarim Basin. The Cenozoic strata are subdivided in four main lithostratigraphic units from early Paleogene up to present (e.g., [*Bosboom et al.*, 2014; *Laborde et al.*, 2019; *Wei et al.*, 2013]): the Kashgar and Wuqia Groups, and the Artux and Xiyu Formations. The Kashgar Group is composed of marine limestones, siltstones, gypsum and marls dating from Paleocene to Eocene. The Wuqia Group, consisting mostly of sandstones, siltstones and claystones, is marking the transition from marine to continental deposits. Then, the Artux Formation, made up of similar lithologies, is marked by the appearance of the first conglomerate layers. Finally, the Xiyu Formation is mostly composed of conglomerates, interbedded with some sandy layers. This upward coarsening of the Cenozoic series is interpreted to be related to the progressive thrusting of the Western Kunlun mountain wedge over the flexural Tarim Basin [*Laborde et al.*, 2019], as suggested in other mountain ranges worldwide [*Charreau et al.*, 2009; *Dubille and Lavé*, 2015; *Simoes and Avouac*, 2006].

2.1.2 The Hotan anticline and Tiklik thrust

The Hotan anticline is one of the folds forming the mountain front of the Western Kunlun Range. It is located to the south-southwest of the city of Hotan (Figure 2). This ~110 km long and ~20 km wide anticline has an overall N110° direction to the west, turning N90° at its eastern termination. To the east, the Hotan anticline is crossed by two large rivers, the Karakash and the Yurunkash rivers (Figure 2).

The surface geology of the Hotan anticline reveals significant lateral variations. At its eastern termination, only the upper Cenozoic series outcrops, and a lateral facies transition can be observed from the Artux to the Xiyu formations (Figure 2b). Laterally, the whole Cenozoic to Mesozoic series, down to Paleozoic limestones and metamorphic phyllites, is progressively exhumed from east to west [*Baby et al.*, 2022] (Figure 2b). Along the northern forelimb of the Hotan anticline, the Xiyu Formation is deposited unconformably over the older formations with a basal erosive contact [*Baby et al.*, 2022; *X Cheng et al.*, 2017; *X Jiang et al.*, 2013] (Figure 2b). South of the anticline, the Tiklik fault separates the inner and outer ranges of the Western Kunlun (Figure 2b).

Several cross-sections based on the interpretation of seismic reflection profiles and of one borehole have been proposed across the Hotan anticline [*Baby et al.*, 2022; *X Cheng et al.*, 2017; *X Jiang et al.*, 2013]. Of particular interest here, the recent work of [*Baby et al.*, 2022] explores the lateral variations in the sub-surface structure of the anticline, in line with the observed lateral

variations in surface geology. They interpret the anticline as resulting from a broad ramp fault-bend anticline over the Hotan thrust, subsequently folded by a footwall duplex. All these structures are blind and form the Hotan thrust system (Figure 3). The Hotan thrust involves Paleozoic phyllites and develops at a probable stratigraphic contrast between the Paleozoic metamorphic series of the Western Kunlun Range and the coeval sedimentary units of the Tarim Basin [*Baby et al.*, 2022; *Laborde et al.*, 2019]. In contrast, the underlying duplex only implies structures neo-formed within the Tarim sedimentary series. These thrusts connect the two regional decollement layers: the Cambrian decollement and the one at the base of the Cenozoic series. The geometry of layers imaged in seismic profiles implies that an intermediate decollement level may be locally present at the base of the Permian [*Baby et al.*, 2022] (Figure 3). In our subsequent analysis, we will rely on the sub-surface structure of the Hotan anticline as described in the cross-sections bb' and cc' of [*Baby et al.*, 2022] (Figures 2-3). Locally, at the scale of these two geological sections, the underlying footwall duplex has orientations that differ slightly from the N110 axis of the Hotan anticline (Figure 2). By considering the structural data of [*Baby et al.*, 2022], we find that the frontal duplex ramps locally have a N95°-N100° direction.

Total shortening across the Hotan anticline amounts to 35-40 km, and is diversely partitioned along-strike between the Hotan thrust and the footwall duplex [*Baby et al.*, 2022]. The footwall duplex mostly developed to the west, uplifting and exhuming the deeper series forming the anticline of the Hotan thrust ramp, and is absent at the eastern extremity of the fold (Figures 2b-3). From the analysis of growth strata preserved in the forelimb of the anticline, [*Baby et al.*, 2022] suggested that deformation started by 16 Ma (or possibly earlier), in line with previous work [*X Cheng et al.*, 2017]. The transition from the basement Hotan thrust ramp to the footwall duplex is recorded in growth layers, and appears diachronous along-strike, with an eastward propagation of the duplex, together with the forward propagation of structures into the Tarim Basin.

Thermochronological data indicate that fast exhumation of the basement in the hanging wall of the Tiklik fault occurred sometime during the Late Oligocene and Early Miocene, and has been more moderate since then [*X Cheng et al.*, 2017]. These data record ~4-9 km of exhumation, that may translate into >2-12 km of shortening, depending on how surface uplift and paleo-elevations have evolved [*X Cheng et al.*, 2017]. The recent activity of this thrust remains undocumented.

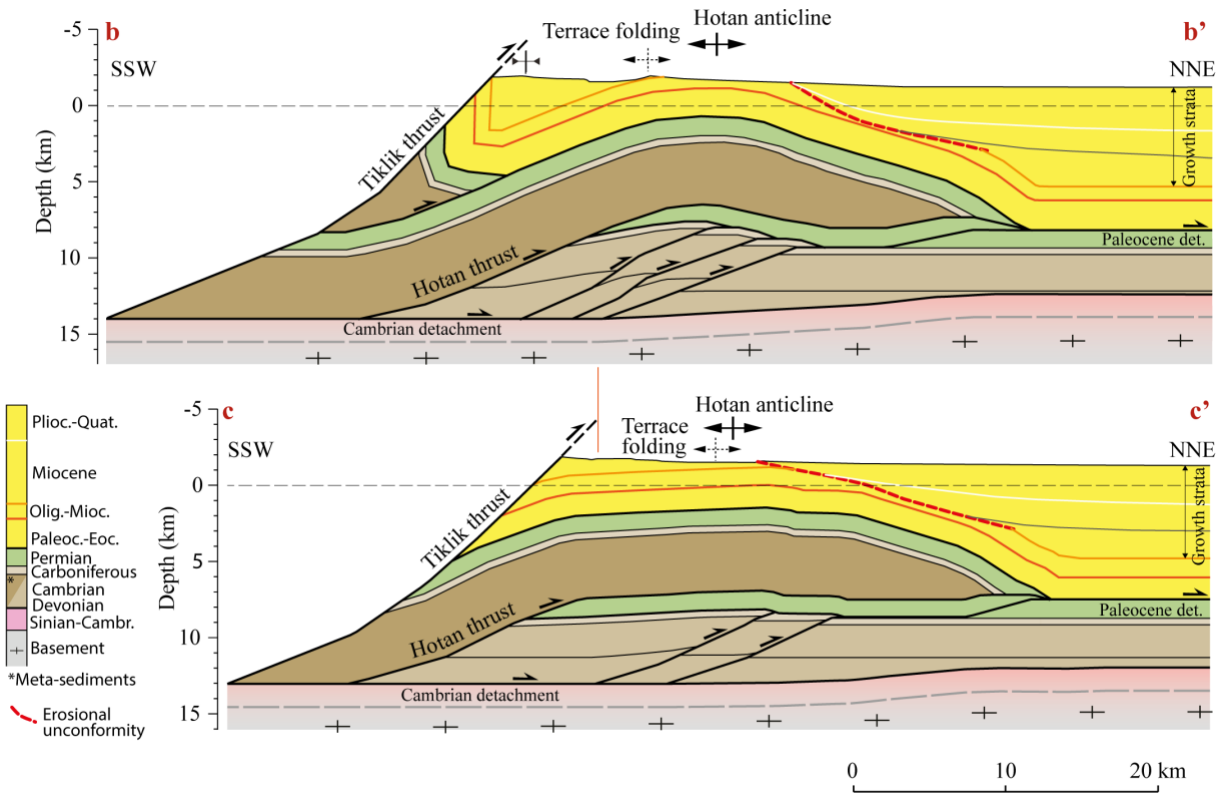

Figure 3. Structural geometry of the Hotan anticline (location of sections on Figure 2). Sections bb' and cc' are taken from [*Baby et al.*, 2022]. In this study, we only consider the sections that are closest to our site of investigation along the Karakash River and to the section AA' used for our morphological and morphotectonic interpretations (Figure 2b). The Hotan anticline results from a broad ramp anticline over the Hotan thrust, subsequently folded by the ramps of a footwall duplex. Axis of terrace folding (Figures 5-6) projected on structural sections bb' and cc'.

2.2 Kinematics of crustal shortening across the Western Kunlun Range

A total Cenozoic shortening of ~55-100 km across the Western Kunlun Range was estimated by crustal mass balance budgets [*Baby et al.*, 2022; *Laborde et al.*, 2019]. Considering a probable age of ~20-23 Ma for the initiation of the Cenozoic reactivation of the mountain range, as suggested from thermochronology (e.g., [*Cao et al.*, 2015; *X Cheng et al.*, 2017; *Sobel and Dumitru*, 1997; *E Wang et al.*, 2003]) and the dated coarsening of the sediments within the foreland basin [*Blayney et al.*, 2019; *X-D Jiang and Li*, 2014; *Metivier and Gaudemer*, 1997; *Zheng et al.*, 2015], a long-term average shortening rate of ~2.4-5 mm/yr is obtained. This value is comparable, in its lower bound though, with the long-term (over several million years) shortening rates deduced from the structure and kinematics of some of the structures of the outer range, such as the Yecheng-Pishan [*Guilbaud et al.*, 2017; *Sun et al.*, 2019; *J Xu et al.*, 2020] or the Hotan [*Baby et al.*, 2022] anticlines, in line with the idea that most of the Cenozoic crustal shortening across the Western Kunlun Range has been absorbed in the foothills [*Baby et al.*, 2022]. Based on the analysis of growth strata, [*Baby et al.*, 2022] suggested that shortening rates across the Hotan anticline may have significantly decreased from ~5 mm/yr to <0.5 mm/yr by

~8-9 Ma. Such deceleration has not yet been documented or corroborated elsewhere along the mountain range.

Data on recent kinematics (i.e., over the last 100s kyrs), at the shorter time scale of several seismic cycles, are too scarce along the mountain front to be compared to long-term estimates. The 2015 Mw 6.4 Pishan earthquake ruptured the most frontal blind ramp of the Yecheng-Pishan anticline [*Li et al.*, 2016; *Lu et al.*, 2016] and attracted some attention on this particular structure where several flights of fluvial terraces are preserved and record recent tectonic uplift [*Ainscoe et al.*, 2017; *Guilbaud et al.*, 2017; *J Xu et al.*, 2020]. Due to the disputed ages of some of these terraces, the analysis of these geomorphic markers of deformation suggests fault slip rates ranging from 0.5 to 3.9 mm/yr over the last ~300-500 kyr [*Guilbaud et al.*, 2017; *J Xu et al.*, 2020; *Y Zhang et al.*, 2023]. As any slip on the blind ramps of the mountain front is to be transferred forward onto the Paleocene decollement all the way northward to the Mazar Tagh emerging ramp (Figure 1c), such slip rate values are also expected to be found there. A tentative estimate of >0.9 mm/yr from an uplifted (but poorly dated) terrace has been proposed on the Mazar Tagh [*Pan et al.*, 2010].

Existing estimates of recent shortening and fault slip rates are therefore limited to draw a clear and complete picture of the recent kinematics of shortening across the Western Kunlun mountain front. More specifically, these data are absent in the particular case of the Hotan anticline even though they would allow for exploring the idea of a recent deceleration of shortening rates as proposed by [*Baby et al.*, 2022], or for investigating possible lateral variations along the mountain front, by comparison with the results obtained in Pishan [*Guilbaud et al.*, 2017; *J Xu et al.*, 2020].

3 Geomorphology of the Karakash River across the Hotan anticline and Tiklik thrust

To investigate the recent kinematics of uplift and shortening of the Hotan anticline and Tiklik fault, we conduct a geomorphological analysis of a site located along the Karakash River, where it crosses these various structures. The Karakash River is one of the largest rivers flowing out of the Western Kunlun Range, with a total drainage area of ~19000 km2 extending well beyond the Altyn-Tagh / Karakash fault at the rear of the mountain range (Figure 1b).

In our study area, the river crosses the Tiklik fault and flows out of the high-relief inner range, meanders and follows its course behind and then across the Hotan anticline (Figure 2). It then flows north into the Tarim Basin and forms a relatively large (>500 km2) active alluvial fan. From the inner range to the alluvial fan, several fluvial terraces were incised and preserved (Figure 4).

3.1 Data and Methods

3.1.1 Field and satellite observations

We map fluvial terraces within our study site using high-resolution (0.5 m) Pléiades images. A high-resolution digital elevation model (DEM) is computed using the open-source software suite MicMac developed by the Institut de physique du globe de Paris (IPGP, France) and the Institut national de l'information géographique et forestière (IGN, France) [*Rosu et al.*,

2015; *Rupnik et al.*, 2017]. In some areas of the images where very smooth, bright and white surfaces are located, the resultant DEM is not well-defined due to poor image correlation.

Therefore, these areas are excluded from our analysis. The DEM is subsequently down-sampled to a 2m-resolution. To complement these data and cover a larger zone, a 30m-resolution ALOS World 3D DEM together with the satellite images from the Google Earth database are also used. Observations on satellite images and DEMs are completed by field observations during four different field surveys in 2003, 2005, 2017 and 2019, with a cumulated on-site stay of ~7-9 days due to limited field permits. A topographic profile across the Tiklik fault scarp is measured in the field using a theodolite.

3.1.2 Mapping and correlation of fluvial terraces

Fluvial terraces are abandoned former river beds and as such, they appear in the field as relatively planar surfaces, delimited by risers, above and along the present-day river bed (Figure 4). The relative altitudes of the various terraces reflect their relative ages, the higher terraces being the older ones. Some of the mapped surfaces are complex as they may correspond to more than one fluvial terrace. Indeed, lateral erosion by the Karakash River reveals that in some cases, the loess or colluvial cover hides several generations of imbricated erosional fluvial strath terraces (Figure 4a). This is the case in particular for our highest, and therefore oldest identified surfaces. To avoid these issues, we will mostly rely on the lowest, and therefore youngest surfaces. Because, terrace surfaces may be locally covered by colluvium from higher levels (Figures 4 b-e), we will mostly consider in our quantitative analysis their altitudes nearest to their riser, i.e. at distance from other higher terraces and closest to the present river.

The terrace record is discontinuous along the river, so that terrace patches are correlated with each other using local across- and along-topographic profiles. Such correlation is subsequently verified or completed with chronological constraints obtained from the dating of some terrace patches (Section 4). Because of the presence of a fault scarp along the trace of the Tiklik fault (Figure 4e), we consider the possibility that the terrace record may be disrupted and therefore discontinuous across this fault. Therefore, correlation of terraces and their attributed relative ages is first performed separately on either side of the fault, and then combined together in our final map using the obtained absolute ages of terraces.

3.1.3 Computing terrace incision

Terrace elevations are extracted from available DEMs to compute terrace incision above the present-day Karakash River. Incision is calculated along the long-distance profile of the river course (Figure S1 in supplementary information). Because the river meanders and changes its main flowing direction as it is deflected eastwards behind the Hotan anticline, the river course is simplified by considering four segments of average similar flowing direction to compute terrace incision (Figure 5, inset). When defining these main river segments, we verify that the average long river profile is relatively simple and linear in each one of these segments (Figure S1). Some terrace patches are preserved within major river meanders, i.e., at the intersection between two main river segments. In this case, we compute the incision of these terraces along each one of the two considered river segments separately, and deduce from there the range of their incision when combining both results. In these cases, we find that incision is determined with a ~25-30 m

maximum uncertainty corresponding to the difference in river elevation on either side of these major meanders. Once calculated, incision is projected perpendicular to the axis of tectonic structures to finally derive incremental uplift.

3.2 Geomorphological response to active tectonics along the Karakash River

The Tiklik thrust has a clear morphological expression where the Karakash River flows out of the inner range, with a ~14 m high scarp disrupting fluvial terraces (Figure 4e), testifying that the fault is active. Downstream from this scarp, the river first flows northward, is then deflected southeastward along the backlimb of the Hotan anticline, and finally flows once again northward to cross the anticline at its eastern termination (Figure 5). Major meanders are indeed located over the backlimb of the Hotan anticline (Figures 5 and 6a). This change in the overall river flow direction and its deflection towards the fold lateral termination is interpreted as related to the uplift of the Hotan anticline, as similarly observed in other contexts (e.g., [*Benedetti et al.*, 2000; *Burbank et al.*, 1996; *Lavé and Avouac*, 2000]), most probably in line with the eastward propagation of folding over time [*Baby et al.*, 2022].

Six levels of fluvial terraces are identified and mapped within our study area, labeled T1 to T6 from the lowermost and youngest to the topmost and oldest mapped surface (Figure 5). The three uppermost terrace levels (T4 to T6) are scarcely preserved and form highly discontinuous patches, but the remnants of the three other lower and younger levels (T1 to T3) are abundant and relatively well-preserved along the river course. From field observations, we cannot discard the possibility that other secondary generations of terrace levels are hidden below the highest and oldest surfaces, as they are covered with loess and colluvium (Figures 4a and c). Our field surveys also indicate that terraces are mostly strath terraces, with < 10 m of fluvial deposits (cobbles, pebbles and/or sand) above the basal erosional strath surface (Figure 4d), indicating ongoing active incision. Only locally, immediately downstream of the Tiklik fault trace and where a syncline is described in the underlying geology behind the Hotan anticline, fill terraces are suspected in the field. There, fluvial deposits are observed over > 10 m, with no clear observation of the substratum beneath these sediments (Figures 4e and 5). To the north-east of the investigated site, the Karakash River crosses the Hotan anticline and aggrades to form a large alluvial fan (Figures 5 and 6a). These observations clearly indicate that the pattern of river incision and aggradation follows the structural pattern of the Tiklik thrust and of the Hotan anticline. Accordingly, active tectonics is found to exert a first-order control on the morphology of our study site.

The incision pattern is relatively well-defined and continuous throughout the whole area for terraces T1 to T3, and more scattered for the higher mapped levels. For a comparison with sub-surface geology, terrace incision is projected perpendicular to structures (Figure 6b). As the orientations of the Hotan anticline (as defined from surface geology, Figure 2) and footwall duplex are slightly different, we tested both directions. When a projection perpendicular to the Hotan anticline is considered (i.e., along a N24° axis), two zones of higher incision appear, which are not directly comparable to underlying structures. Alternatively, we find a better correlation between the pattern of terrace incision and the underlying geology when projecting all data perpendicular to the direction of the footwall duplex ramps. More specifically, the best correlation between all terrace data and the underlying geology (Figures 6b-c) is found when

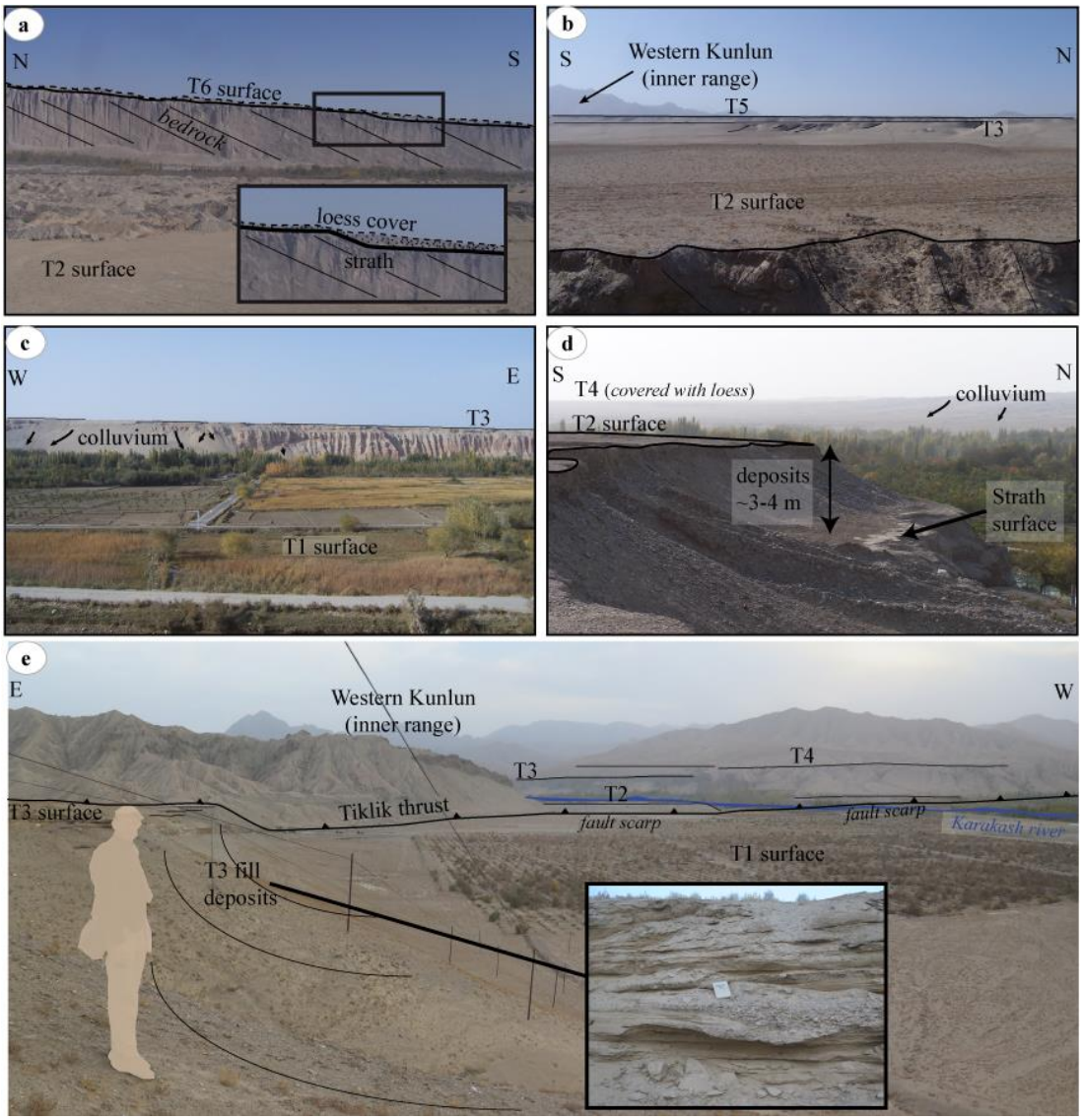

Figure 4. Field pictures of the investigated fluvial terraces. These pictures are located on the morphological map of Figure 5 (numbering of pictures as in the map). (a) Planar surface of T6, on the left bank of the Karakash River. Even though continuous, this surface possibly hides, in the details, several generations of incisional terraces, as illustrated by the step in the basal strath and overlying fluvial deposits subsequently covered by loess (detail picture). (b) Planar surfaces of terraces T2, T3 and T5, on the right bank of the Karakash River. (c) Planar surfaces of terraces T1 and T3. T1 presently mostly hosts agricultural activities. Laterally, the terrace riser of T3 is hidden and covered by colluvial deposits (left side of the picture). (d) T2 terrace, illustrating the strath erosional basal surface, covered by ~3-4 m of fluvial deposits. (e) View over the Tiklik thrust fault and scarp, where the Karakash River flows out of the Western Kunlun inner range. The ~14 m high thrust scarp separates terrace T2 upstream from terrace T1 downstream. Downstream of the Tiklik thrust, terraces are identified as aggradational from their thick fill deposits, as illustrated here for T3. Inset: detail view on the fill deposits of T3, with field notebook for scale.

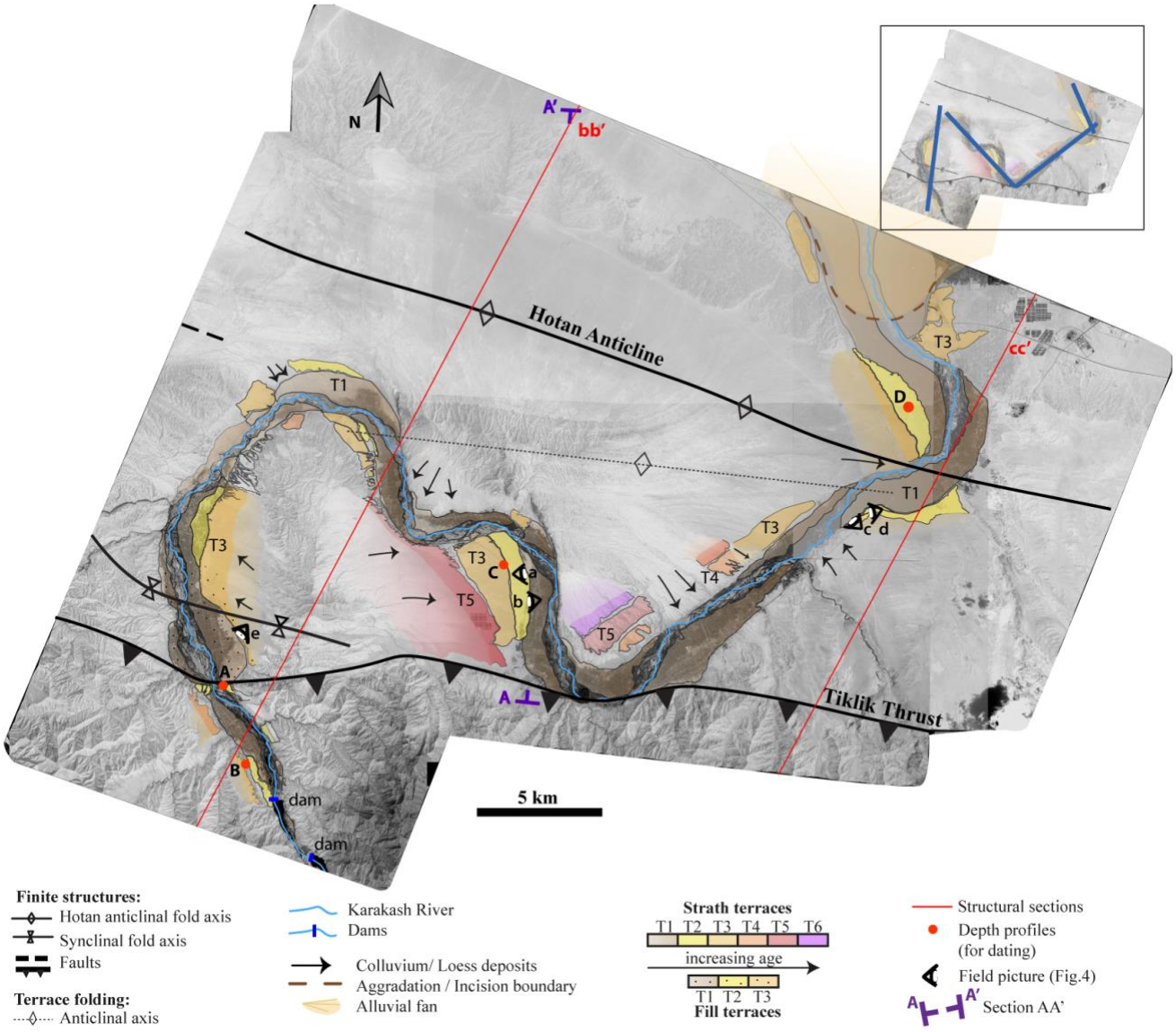

Figure 5. Map of the investigated site (location of map on Figure 2b). Various terrace levels are mapped along the Karakash River where it flows out of the Western Kunlun inner range, crossing the Tiklik thrust and the Hotan anticline. They are identified in the field as fill terraces immediately downstream of where the river crosses the Tiklik thrust (Field picture e, Figure 4e), and strath terraces elsewhere (Field picture d, Figure 4d). Four depth profiles within some of these terrace levels (sites A to D) have been sampled to date them using in-situ produced cosmogenic isotopes (Figure 7). Terrace incision is calculated all along the river course, by discretizing the river into four main flowing segments (upper right inset). A combined long-distance profile of the river and terraces can be found in Figure S1 (supplementary information). Incision is then projected on profile AA' (Figure 6), which is perpendicular to the direction of footwall duplex ramps and of terrace folding.

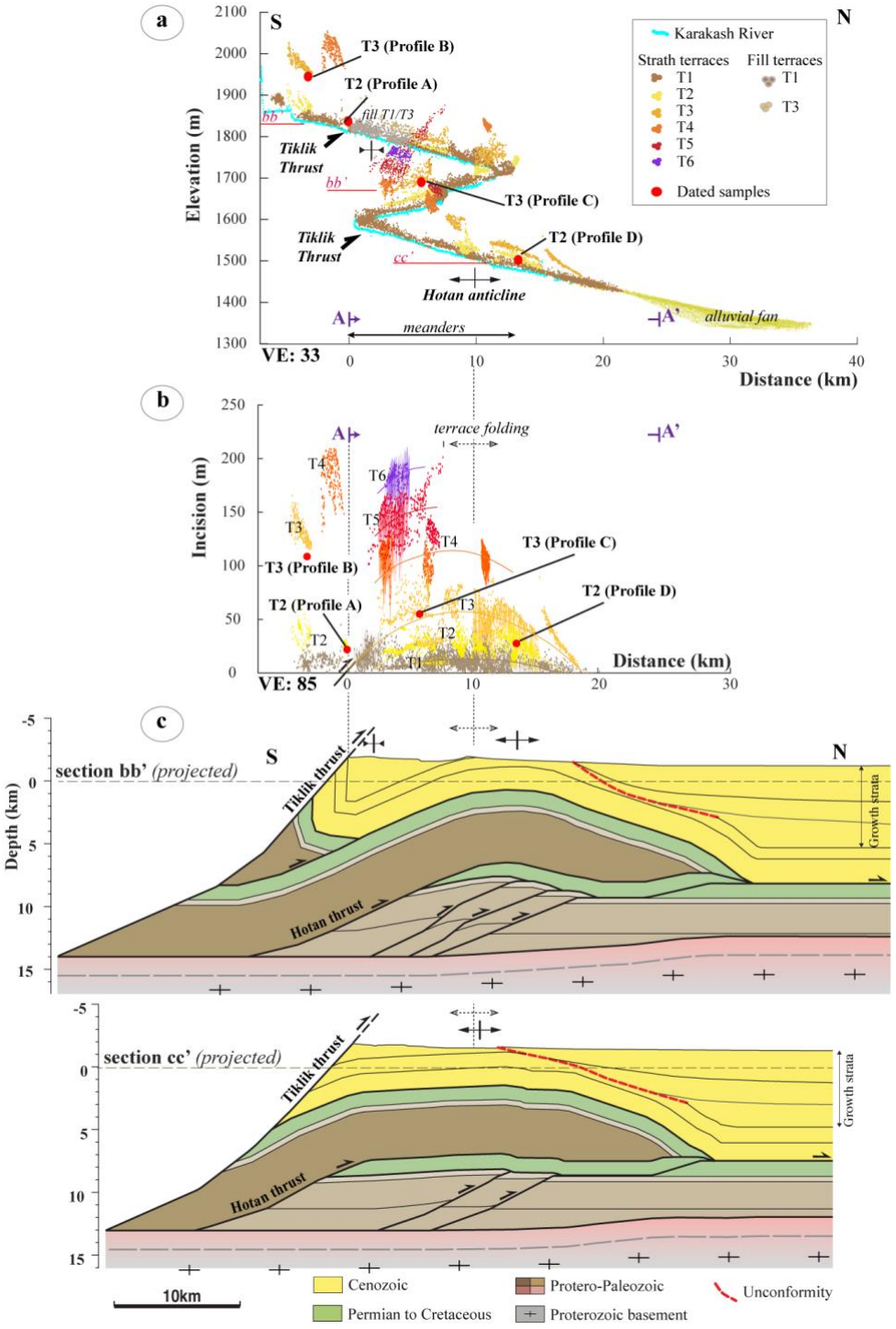

Figure 6. Projected terrace elevation and incision compared to the structural geometry of the Hotan anticline. All the data are projected parallel to profile AA' (Figures 2 and 5), and the origin of horizontal distances is set to where the Karakash River flows out of the Western Kunlun inner range and crosses the Tiklik thrust. VE: vertical exaggeration. (a) Projected river and terrace elevations. Main river meanders locate at km 0 and 10 along the section and are illustrated by the alternation of southward and northward changes in river flow, accompanied by a significant

(Figure 6) change in river elevation. Terrace levels are color-coded as in the map of Figure 5. Location of sampled depth profiles (A to D) are reported together with correlated terrace levels. Various structural features encountered along the Karakash River course are reported along the projected river profile, together with the intersections of the river course with structural sections bb' and cc'. (b) Projected terrace incision for documented strath terraces. Terraces are color-coded as in Figure 6a. Terrace incision is determined all along the longitudinal river profile (inset of Figure 5), before being projected. Transparent colored vertical lines indicate the possible range of incision values where the river meanders. Even though not continuous in particular for terrace levels higher than T3, the terrace record indicates folding, with a broad zone of higher incision by km 10. Terrace folding appears spatially correlated with thrusting over the frontal ramps of the footwall duplex (Figure 6c). (c) Structural sections bb' and cc' from [*Baby et al.*, 2022] (Figure 3), projected onto section AA'.

projecting all data along section AA’ oriented N05° (in purple on Figure 5), slightly oblique to the direction of the frontal duplex ramps. This minor obliquity may be related to data uncertainties, or rather relate to the combined eastward and forward propagation of duplexes over time, as this direction coincides with that obtained when kinematically relating the penultimate duplex ramp along section bb’ to the most frontal one along section cc’. When considering all data projected along AA’, incision is highest and delineates a broad ~10-15 km wide terrace anticline in the area of the major river meanders, along the backlimb of the main Hotan anticline (Figure 6). There is therefore a slight spatial discrepancy between the finite structure seen from surface geology and the morphological expression of active deformation. In fact, surface geology is mostly dominated by thrusting over the Hotan thrust along the Karakash River (Figure 3), whereas incision spatially coincides better with the location of the underlying duplex (Figure 6), indicating that these blind footwall ramps have been active over the time span represented by the terrace record.

Slip on the duplex ramps is to be transferred northward and upward to the frontal smaller blind ramp north of the anticline, and then into the Paleogene decollement. The frontal small blind ramp, connecting an intermediate decollement within the Permian and the base of the Cenozoic series, spatially coincides with the active alluvial fan of the Karakash River (Figures 5 and 6a) where growth layers have been described in seismic profiles [*Baby et al.*, 2022] (Figures 3 and 6c). This further supports the recent activity of the blind structures in the footwall of the Hotan thrust.

4 Ages of terraces along the Karakash River

4.1 Data and Methods

4.1.1 Approach

Cosmogenic nuclides, such as ^{10}Be or ^{26}Al, are produced in situ in quartz minerals due to the exposure of near surface rocks to cosmic radiation, and undergo radioactive decay with time (e.g., [*Lal*, 1991]). Because of the attenuation of cosmic radiation across the rock mass, the production of nuclides decreases exponentially with depth. The nuclide concentration in surface rocks can be expressed as:

$$C(z,t) = C(z,t_0).e^{-\lambda t} + \sum_i \frac{P_i}{\lambda+\mu_i\varepsilon} e^{-\mu_i z}(1-e^{-(\lambda+\mu_i\varepsilon)t}) \quad (1)$$

where C is the concentration of atoms (atoms.g^{-1}), z is the depth (cm), t is the exposure time (yr), λ is the radioactive decay of the considered nuclide (yr^{-1}), P is the production rate at the surface (atoms.g^{-1}.yr^{-1}), μ is the attenuation coefficient (cm^{-1}), ε is the surface erosion rate (cm.yr^{-1}), and i represents the production pathways for neutrons and muons (e.g., [*Braucher et al.*, 2003; *Brown et al.*, 1992; *Gosse and Phillips*, 2001; *Lal*, 1991]). $C(z,t_0)$ corresponds to the initial concentration of atoms when exposure initiated, inherited from a prior exposure or transport history. Attenuation μ_i is determined as the ratio ρ/Λ_i , where ρ is the density of the material (g.cm^{-3}) and Λ_i the attenuation length (g.cm^{-2}) of the considered cosmic particle i (neutron or muon). Provided that parameters related to attenuation, production and radioactive decay are known, modeling the nuclide concentrations along a depth profile of an exposed surface is commonly used to derive the exposure age of the surface, as well as the average erosion rate and the initial inheritance (e.g., [*Anderson et al.*, 1996; *Guilbaud et al.*, 2017; *Hidy et al.*, 2010; *Repka et al.*, 1997; *Yang et al.*, 2019]).

4.1.2 Collected samples and analyses

To date the abandonment of terraces using in situ produced ^{10}Be, we collected samples along depth profiles in four of the mapped fluvial terraces. During field campaigns in 2003 and 2005, we sampled two terraces located in the hanging wall of the Tiklik thrust (Figure 5). Sampled terrace deposits are here formed of boulders and cobbles. At site A, a ~1.65 m deep profile was sampled into the man-made refreshed riser of the lower T2 terrace (Figure 7). At site B, a ~2.1 m deep profile was sampled along the steep riser wall of the highest terrace (terrace T3) (Figure 7). For this site, the top sample of the profile is constituted of amalgamated surface pebbles from the terrace surface (such surface sample could not be collected on the surface of T2 at site A due to reworking). Further downstream, two terraces located over the limbs of the Hotan anticline have also been sampled in 2017 and 2019 for dating. At site C, a profile was realized into terrace T3, in the backlimb of the Hotan anticline. Amalgamated pebbles from 5 cm-thick horizons and a sand sample were collected along a ~2 m-deep recently man-made excavation (Figure 7). The top sample is constituted of amalgamated surface pebbles. Finally, at site D, a fourth depth profile was collected along a recently man-made excavation into terrace T2, in the downstream portion of the river (Figure 5). This profile is ~3.3 m deep, and 5 cm-thick sand and amalgamated gravel horizons were collected from bottom to top (Figure 7). This profile is completed by two other deeper samples, accessible from nearby excavations (within ~100 m from the main profile) into the same terrace, at 4.5 and 6.7 m below the terrace surface (Figure 7).

Chemical analyses of samples from profiles A to C were prepared at the Cosmogenic Isotope Laboratory of the University of Strasbourg (ITES, Strasbourg, France) and at the Centre Européen de Recherche et d'Enseignement des Géosciences de l'Environnement (CEREGE, Aix-en-Provence, France). Samples from profile D were prepared at the Purdue Rare Isotope Measurement Laboratory (PRIME Lab, Purdue University, USA). Most Accelerator Mass Spectrometer (AMS) measurements were performed at the French ASTER facility (CEREGE, Aix-en-Provence, France). Only two measurements were conducted at the Lawrence Livermore National Laboratory (LLNL, Livermore, USA). We obtained 40 measurements of ^{10}Be concentrations and 17 measurements of ^{26}Al concentrations. All analytical results are reported in Table 1. Further analytical details can be found in supplementary material (Text S1 and Table S1).

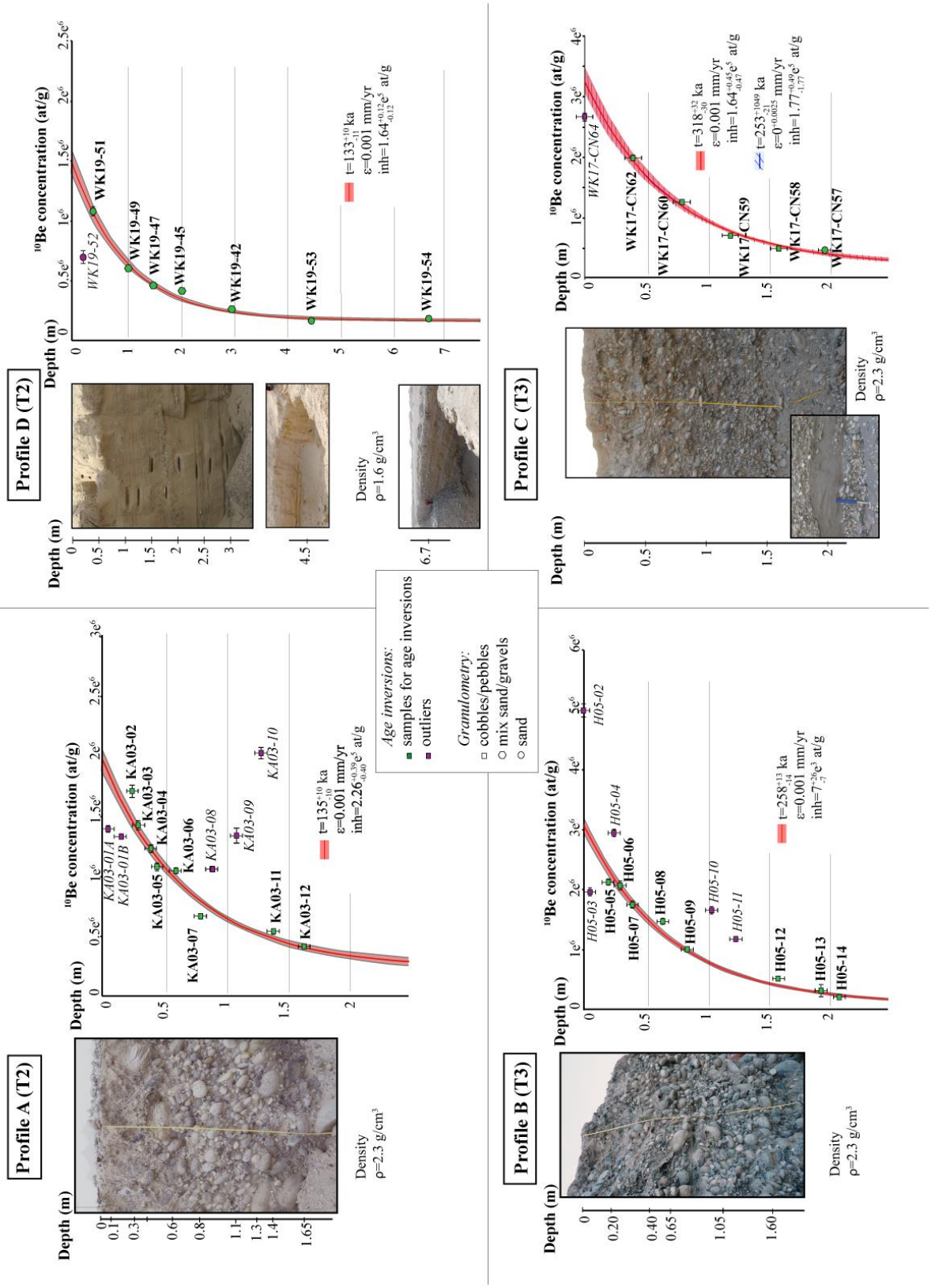
Profile A (T2)
Profile B (T3)
Profile C (T3)
Profile D (T2)
Depth (m)
^{10}Be concentration (at/g)
Density
ρ=2.3 g/cm^3
ρ=1.6 g/cm^3
t=135$^{+10}_{-10}$ ka
ε=0.001 mm/yr
inh=2.26$^{+0.39}_{-0.40}$e^5 at/g
t=258$^{+13}_{-14}$ ka
ε=0.001 mm/yr
inh=7$^{+26}_{-7}$e^3 at/g
t=318$^{+33}_{-30}$ ka
ε=0.001 mm/yr
inh=1.64$^{+0.45}_{-0.47}$e^5 at/g
t=253$^{+1049}_{-21}$ ka
ε=0$^{+0.0025}_{-0}$ mm/yr
inh=1.77$^{+0.49}_{-1.77}$e^5 at/g
t=133$^{+10}_{-11}$ ka
ε=0.001 mm/yr
inh=1.64$^{+0.12}_{-0.12}$e^5 at/g
KA03-01A
KA03-01B
KA03-02
KA03-03
KA03-04
KA03-05
KA03-06
KA03-07
KA03-08
KA03-09
KA03-10
KA03-11
KA03-12
H05-02
H05-03
H05-04
H05-05
H05-06
H05-07
H05-08
H05-09
H05-10
H05-11
H05-12
H05-13
H05-14
WK17-CN57
WK17-CN58
WK17-CN59
WK17-CN60
WK17-CN62
WK17-CN64
WK19-42
WK19-45
WK19-47
WK19-49
WK19-51
WK19-52
WK19-53
WK19-54
Age inversions:
samples for age inversions
outliers
Granulometry:
cobbles/pebbles
mix sand/gravels
sand

Figure 7 ^{10}Be concentration with depth along the four depth profiles A to D. A field picture is provided for each depth profile, at scale with the graphs illustrating the measured concentrations with depth. Multiple pictures indicate that some of the samples were taken laterally from the main depth profile (Profiles D and C). The densities used for the age inversions have been determined from the average grain size (cobbles, gravels, sand) found all along the profiles. They are reported for each depth profile. The grain size of the samples is also reported by various symbols. Samples considered for age inversions are reported in green, and outliers in purple. Best-fit solutions of the age inversions when erosion is fixed (Model 1) are plotted (red line, with red confidence interval), and the associated parameters are indicated. In the case of profile C, the best-fit solution in the case that erosion is also inverted (Model 2, blue line and hatched interval) is also indicated. Analytical details for all samples in Table 1 and model parameters for age inversion in Table 2.

4.1.3 Age determination

The exposure time (taken for the time of abandonment of the terraces) is determined from the modeling of the ^{10}Be concentrations along depth profiles A to D, following equation (1) and using the parameters detailed below. Even though the ^{26}Al concentration has been measured for 17 of our 40 samples, we do not model it. The available ^{26}Al concentrations are rather used to question the reliability of ^{10}Be measurements whenever the ^{26}Al/^{10}Be ratio significantly departs from the theoretical production ratio of 6.61 [*Braucher et al.*, 2011].

The radioactive decay λ of ^{10}Be is set to 5.13 10-7 yr^{-1} (^{10}Be half-time of 1.35 10^6 yrs) [*Chmeleff et al.*, 2010; *Korschinek et al.*, 2010]. The production rate *P* varies as a function of time and space, depending on the solar activity and on the Earth's magnetic field. Here, we however use the time constant scaling scheme "St" [*Lal*, 1991; *Stone*, 2000] found to be satisfactory [*Balco and Rovey*, 2008; *Borchers et al.*, 2016], with a production rate of 4.01±0.33 atoms.g^{-1}.yr^{-1} at sea level and at high latitudes to calculate the expected local ^{10}Be production rate at our study site. To derive the slow and fast muonic production rates, we followed [*Braucher et al.*, 2011] and scaled the rates with atmospheric pressure ignoring the latitudinal effect. Here, a production rate ranging between 11.71 and 14.94 atoms.g^{-1}.yr^{-1} is determined, assuming that the present river base level represents the altitude of terraces when folding initiated. We use attenuation lengths Λ of 160 g.cm^{-2}, 1500 g.cm^{-2}, and 4320 g.cm^{-2} for neutron, and slow and fast muons, respectively [*Balco*, 2017; *Braucher et al.*, 2011; *Marrero et al.*, 2016]. The density ρ of the sampled terrace profile is set to 2.3 g.cm^{-3} when these terraces are constituted of boulders and pebbles (Sites A, B and C), and to 1.6 g.cm^{-3} when they are constituted of finer material such as sand or gravels (Site D). We first set the erosion rate ε to 10^{-6} m.yr^{-1} (Model 1), following the value obtained from terraces known to be in erosional steady-state in Pishan (see supplementary material in [*Guilbaud et al.*, 2017]). Erosion is also tested as a free parameter (Model 2). Further details on how these various parameters were determined are provided in supplementary material (Text S2).

Equation (1) is first inverted for time (exposure age *t*) and inheritance ($C(z,t_0)$) by minimizing the misfit between a theoretical curve and the observed data, following a χ^2 criterion:

$$\chi^2 = \sum_{i=1}^{n} \left(\frac{C_i - C(z_i,t)}{\sigma_{C_i}} \right)^2 \quad (2)$$

Sample	Rock type	Thickness (cm)	Depth (cm)	10Be (1e5 at/g qtz)	26Al (1e5 at/g qtz)	26Al/10Be
Profile A (36.88743°N, 79.41021°E, 1837 m) - Terrace T2						
KA03-1A	cobble	5	5	13.966 ± 0.395		
KA03-1B	cobble	5	15	13.343 ± 0.342		
KA03-2	cobble	5	25	17.102 ± 0.589	94.256 ± 3.094	5.51
KA03-3	cobble	5	30	14.274 ± 0.475	78.749 ± 2.605	5.52
KA03-4	cobble	5	40	12.331 ± 0.428		
KA03-5	cobble	5	45	10.822 ± 0.413	70.137 ± 2.547	6.48
KA03-6	cobble	5	60	10.482 ± 0.338		
KA03-7	cobble	5	80	6.69 ± 0.198	39.459 ± 1.467	5.90
KA03-8	cobble	5	90	10.611 ± 0.336		
KA03-9	cobble	5	110	13.437 ± 0.71	44.86 ± 2.193	3.34
KA03-10	cobble	5	130	20.295 ± 0.641		
KA03-11	cobble	5	140	5.447 ± 0.211	36.035 ± 1.51	6.62
KA03-12	cobble	5	165	4.155 ± 0.135		
Profile D (36.99381°N, 79.72292°E, 1500 m) - Terrace T2						
WK19-52	sand	5	20	7.294 ± 0.59		
WK19-51	sand	6	39	11.301 ± 0.417		
WK19-49	gravels	5	105	6.292 ± 0.233		
WK19-47	sand/gravels	5	153	4.826 ± 0.208		
WK19-45	sand /gravels	5	207	4.332 ± 0.23		
WK19-42	sand /gravels	4	300	2.713 ± 0.126		
WK19-53	sand	5	450	1.722 ± 0.064		
WK19-54	sand	5	670	1.897 ± 0.074		
Profile B (36.85861°N, 79.42104°E, 1944 m) - Terrace T3						
H5-2	amalgamated qtz vein pieces	2	0	49.892 ± 1.14		
H5-3	cobble	6	5	19.665 ± 0.707		
H5-4	cobble	6	20	21.284 ± 0.544		
H5-5	cobble	6	25	29.43 ± 0.831	143.33 ± 4.273	4.87
H5-6	cobble	6	30	20.725 ± 0.749	157.137 ± 5.305	7.58
H5-7	cobble	6	40	17.517 ± 0.628	109.146 ± 4.003	6.23
H5-8	cobble	9	65	14.717 ± 0.513		
H5-9	cobble	6	85	9.972 ± 0.442	50.795 ± 2.234	5.09
H5-10	cobble	6	105	16.575 ± 0.635		
H5-11	cobble	6	125	11.713 ± 0.38	59.222 ± 2.416	5.06
H5-12	cobble	7	160	5.161 ± 0.18		
H5-13	cobble	6	195	3.098 ± 0.123	17.307 ± 0.744	5.59
H5-14	cobble	10	210	2.123 ± 0.074		
Profile C (36.93355°N, 79.53800°E, 1691 m) - Terrace T3						
WK17CN-64	amalgamated qtz vein pieces	1	0	26.61 ± 0.679	172.539 ± 4.223	6.48
WK17CN-62	amalgamated pebbles(n≥50)	7	40	19.809 ± 0.52	121.646 ± 3.292	6.14
WK17CN-60	amalgamated pebbles(n≥50)	7	80	12.502 ± 0.35	74.505 ± 1.997	5.96
WK17CN-59	amalgamated pebbles(n≥50)	7	120	6.931 ± 0.222	46.64 ± 1.696	6.73
WK17CN-58	amalgamated pebbles(n≥50)	7	160	4.791 ± 0.143		
WK17CN-57	sand	5	198	4.54 ± 0.159	18.396 ± 1.524	4.05

Table 1 Sampling and isotopic data for all collected samples for cosmogenic analysis. Depth profiles labeled A to D and interpreted terrace levels are indicated and located with geographic coordinates and altitudes at the surface. All the samples taken along these profiles are reported with their depth along the profile, their granulometry or sample characteristics (qtz: quartz; n: number of amalgamated samples). Sampled thickness is integrated vertically along the profile. Complete analytical details are provided in supplementary material (Table S1).

where C_i are the concentrations measured at depth z_i with an uncertainty σ_{Ci}, and $C(z_i,t)$ is the predicted concentration at the same depths using equation (1). Acceptable values for exposure time and inheritance are defined according to various possible confidence intervals: (1) as obeying the condition defined by: $\chi^2 < \chi^2{}_{min} + 1$ (e.g., [*Bevington and Robinson*, 2003; *Braucher et al.*, 2009; *Charreau et al.*, 2017; *Saint-Carlier et al.*, 2016; *Yang et al.*, 2019]; and (2) within a 1σ– or (3) 2σ-confidence interval.

For comparison, these inversions for exposure age and for inheritance in the case of a fixed erosion rate of 10^{-6} m.yr^{-1} (Model 1) are completed by another set of inversions where erosion rates are set free and inverted (Model 2). Ages from Model 1 will be preferred, as erosion is in this case well-defined from a nearby site by steady-state terraces, and Model 2 will be mostly informative. All results are presented in Table 2. The variation of the χ^2 criterion as a function of the various tested parameters, as well as the possible trade-offs between inverted parameters are illustrated in the case of both Models 1 and 2 in supplementary material (Text S2, Figures S2-S9).

4.2 Ages of fluvial terraces

4.2.1 Age inversions

All samples are included in the modeling, except for (1) surface amalgams or samples from stratigraphic levels observed to be perturbed along the depth profiles, such as most often close to the terrace surface (cryoturbation, fissures, etc); and (2) samples whose ^{10}Be content appears too high relative to the overall visually expected exponential decay with depth. Even though disregarded in the inversion of the depth profiles, these samples defined as outliers from stratigraphic, sampling or analytical arguments, are reported with our results for comparison (Figure 7).

^{26}Al/^{10}Be ratios are not used *a priori* to define outliers in the modeling of ^{10}Be concentrations along depth profiles, but are rather taken *a posteriori* as informative of possible complexities. Indeed, these ratios are known for only one third of the samples, and any departure from the expected production ratio could be related to a complexity impacting either the ^{10}Be or the ^{26}Al concentration. Overall, most ^{26}Al/^{10}Be ratios are relatively close to the expected production ratio (Table 1), signifying simple exposure histories. Only 2 samples show low ratios (<3.5). One is a clear outlier along profile A (sample KA03-9) because of a ^{10}Be concentration too high in view of the overall trend at depth (Figure 7); the other is a sand lens along profile C (sample WK17-CN57), when all other samples of this profile are amalgamated pebbles with consistent ^{26}Al/^{10}Be ratios. Because the ^{10}Be concentration of the sand lens is visually within the expected exponential decrease with depth, we have no valuable reason to exclude it from our

605 modeling. All other samples considered as outliers from field or analytical reasons have
606 consistent $^{26}Al/^{10}Be$ ratios.

607

Sampled profiles *(Interpreted terrace level)*	Parameters	Explored Range	Model 1 - fixed erosion rate: Results Model 1 — best fit	interval 1σ min	interval 1σ max	interval 2σ min	interval 2σ max	interval χ2min+1 min	interval χ2min+1 max
A (*T2*)	Age (kyr)	80 - 600	**135**	129	141	125	145	131	139
	Erosion (mm/yr)	fixed to 0.001	**0.001**	-	-	-	-	-	-
	Inheritance (at/g)	10 000 - 300 000	**226 000**	202 000	250 000	186 000	265 000	211 000	241 000
B (*T3*)	Age (kyr)	100 - 600	**258**	250	266	244	271	253	264
	Erosion (mm/yr)	fixed to 0.001	**0.001**	-	-	-	-	-	-
	Inheritance (at/g)	0 - 300 000	**7 000**	0	23 000	0	33 000	0	17 000
C (*T3*)	Age (kyr)	100 - 600	**318**	299	337	288	350	306	330
	Erosion (mm/yr)	fixed to 0.001	**0.001**	-	-	-	-	-	-
	Inheritance (at/g)	0 - 300 000	**164 000**	136 000	192 000	117 000	209 000	146 000	182 000
			without common outliers and deep sand sample						
	Age (kyr)	100 - 600	**359**	336	383	322	399	344	374
	Erosion (mm/yr)	fixed to 0.001	**0.001**	-	-			-	-
	Inheritance (at/g)	0 - 300 000	**66 000**	26 000	105 000	0	130 000	40 000	92 000
D (*T2*)	Age (kyr)	80 - 600	**133**	127	139	122	143	129	137
	Erosion (mm/yr)	fixed to 0.001	**0.001**	-	-	-	-	-	-
	Inheritance (at/g)	10 000 - 300 000	**164 000**	157 000	171 000	152 000	176 000	159 000	168 000

Sampled profiles *(Interpreted terrace level)*	Parameters	Explored Range	Model 2 - free erosion rate: Results Model 2 — best fit	interval 1σ min	interval 1σ max	interval 2σ min	interval 2σ max	interval χ2min+1 min	interval χ2min+1 max
A (*T2*)	Age (kyr)	80 - 3000	**123**	116	1 353	113	3000	120	325
	Erosion (mm/yr)	0 - 0.01	**0**	0	0.0055	0	0.006	0	0.005
	Inheritance (at/g)	0 - 300 000	**228 000**	64 000	260 000	0	274 000	183 000	245 000
B (*T3*)	Age (kyr)	100 - 600	**258**	209	292	205	297	231	264
	Erosion (mm/yr)	0 - 0.01	**0.001**	0	0.0015	0	0.0015	0.0005	0.001
	Inheritance (at/g)	0 - 300 000	**7 000**	0	54 000	0	64 000	0	30 000
C (*T3*)	Age (kyr)	100 - 1500	**253**	238	1100	232	1302	246	486
	Erosion (mm/yr)	0 - 0.01	**0**	0	0.0025	0	0.0025	0	0.002
	Inheritance (at/g)	0 - 300 000	**177 000**	10 000	210 000	0	226 000	128 000	194 000
			without common outliers and deep sand sample						
	Age (kyr)	100 - 1500	**278**	260	664	253	1060	269	639
	Erosion (mm/yr)	0 - 0.01	**0**	0	0.002	0	0.0025	0	0.002
	Inheritance (at/g)	0 - 300 000	**85 000**	0	132 000	0	154 000	0	110 000
D (*T2*)	Age (kyr)	80 - 2000	**124**	117	621	114	1 661	121	289
	Erosion (mm/yr)	0 - 0.01	**0**	0	0.008	0	0.0085	0	0.007
	Inheritance (at/g)	0 - 300 000	**166 000**	115 000	175 000	81 000	179 000	144 000	170 000

608

609 **Table 2** Ages obtained from the inversion of depth profiles A to D (Figures 5 and 7). Interpreted
610 terrace levels are reported for all depth profiles. In Model 1, we invert for age and inheritance,
611 and consider a fixed erosion rate of 0.001 mm/yr. In the case of Model 2, the erosion rate is also
612 inverted. The best-fitting solutions are indicated with the minimum and maximum limits of
613 various confidence intervals (1σ, 2σ and χ^2_{min}+1). Two model runs are reported for the inversion
614 of profile C. The first one considers all samples, except outliers disregarded following commonly
615 defined criteria for all profiles (here: surface amalgamated samples). The second one also
616 excludes the deep sampled sand layer. See text and supplementary material for further details.

617

618 Inversion results are reported in Table 2 and represented in Figure 7 for depth profiles A
619 to D. We here favor age results derived from models with erosion rates fixed to a well-
620 established regional value (Model 1), and conservatively consider 2σ confidence intervals. An
621 age of 135 ± 10 ka is found for the abandonment of terrace T2 from profile A, and 258 +13/-14
622 ka for that of T3 from profile B, upstream and south of the Tiklik thrust. Downstream,

abandonment of terrace T2 is dated to 133 +10/-11 ka from profile D, and that of terrace T3 to 318 +32/-30 ka from profile C. Inheritance varies from 0-33 000 atoms.g^{-1} (Profile B, T3) to 186 000-265 000 atoms.g^{-1} (Profile A, T2) and remains overall limited (up to ~10% of the concentration at the surface). The variability in inheritance does not seem to relate simply to terrace age, distance from the range front, or granulometry (sand, pebbles or cobbles) as sometimes observed (e.g., [*Belmont et al.*, 2007; *Carretier et al.*, 2009; *Lupker et al.*, 2017]). In models where erosion is inverted (Model 2), similar best-fit ages are obtained, but the range of acceptable ages is most often asymmetrically widened toward older values, in line with lower inheritance and/or higher erosion rate (Figures S6-S9 in supplementary material).

4.2.2 Interpreted ages

The results from the age inversions performed on the various profiles on either side of the Tiklik fault are consistent with the correlation established from their morphological analysis (Section 3). The inversion of depth profiles A and D from T2 terrace remnants converges to remarkably consistent age intervals of 135 ± 10 ka and 133 +10/-11 ka, respectively (Model 1, Table 2, Figure 7). These ages are slightly older than those retrieved for terraces labelled T3 ~130 km further west in Pishan [*Guilbaud et al.*, 2017], but remain compatible with the known regional climatic evolution, in particular with wetter regional periods as documented from the Kesang's Cave in the northern Tian Shan [*H Cheng et al.*, 2012]. Even though climatic forcing has been most probably similar at this regional scale, the upstream drainage basins of the Karakash and Pishan rivers are dissimilar, being significantly more extensive and glaciated in its upstream portions in the case of the Karakash River. We propose that these differences explain the slightly different results in the timing of river aggradation and incision, and from there in the timing of terrace abandonment between these two sites, following the findings of [*Malatesta et al.*, 2017] on the variable responses of rivers to a same regional climatic forcing during glacial-interglacial periods. A common age interval of 125-143 ka will be hereafter considered for all terraces T2 along the Karakash River (Table 3).

The situation is not as simple in the case of the inversion of depth profiles B and C into terrace remnants of T3, with ages of 258 +13/-14 and 318 +32/-30 ka, respectively (Model 1, Table 2, Figure 7). The age of 258 +13/-14 ka obtained from profile B fits into the same reasoning as that previously exposed for profiles A and D into terraces T2: this age is slightly older than that derived for terraces labelled T4 in Pishan, but is in line with the known regional climatic evolution. However, such is not the case for profile C, with a slightly older and inconsistent age (given uncertainties) when compared to that from profile B, questioning the possibility that the sampled terrace remnant might be part of an older T4 level. This is even more pronounced when the deepest sand sample WK17-CN57 is not considered in the inversions, because of its different granulometry or its anomalous $^{26}Al/^{10}Be$ ratio (Table 2). However, when erosion is inverted (Model 2), the best-fit solution favors a non-realistic null erosion and ages compatible with the idea that profile C was dug into terrace level T3 (Table 2). Results obtained for profile C rely on the inversion of a relatively smaller set of samples (5 samples instead of 7-8 samples for the other profiles; Figure 7), so that results may be highly dependent on the consideration/exclusion of any single one of them. This is in particular critical at shallow depths (<1m), where the exponential decay of ^{10}Be concentrations is here only defined by 2 unique samples constituted of pebbles and cobbles, and therefore with a possible variability in their concentrations, as observed for shallow samples along Profiles A and B of similar granulometry. As a result, the solution to profile C drawn by these fewer samples is clearly not unique, as both

solutions issued from Models 1 and 2 provide the same fit to the data, despite different resultant ages, as long as the other parameters are adjusted (Figure 7). Given this, we have considered the possibility that profile C was in fact sampled into an older T4 terrace level. However, we were not able in this case to find a satisfactory solution for terrace correlation, combining relative ages from mapping and absolute ages from dating. Given all these considerations, we favor the idea that profile C is part of a T3 terrace. Because of limited sampling or because of a locally lower erosion rate, its age could not be well-defined by following the same approach as that of the other profiles. From this, and providing the age solution for profile B (Model 1) as well as one of the solutions for profile C (Model 2), we will hereafter attribute and consider the common age interval of 244-271 ka for terraces T3 along the Karakash River (Table 3).

Terrace level	Interpreted ages (ka)	Base level changes (m)	Sinuosity	Maximum excess incision (sinuosity)	Uplift (m) - average (*extended*)	Fault slip (m) average (*extended*)
Present river	-	-	2.14	-	-	-
T1	30-60	12-30 (*9-36*)	2.14	5.45	16-63 (*16-77*)	34-192 (*33-248*)
T2	125-143	50-71 (*37-86*)	2.08	15.7	79-120 (*64-120*)	169-367 (*131-389*)
T3	244-271	97-136 (*73-163*)	2.03	28.24	146-224 (*116-242*)	311-689 (*239-784*)

Table 3 Characteristics attributed, measured or calculated for the various terrace levels. Interpreted ages cover the time span common to the 2σ age intervals retrieved from the inversion of depth profiles for each terrace level T2 and T3, and is attributed to T1 by comparison to the known regional climatic evolution. Base level changes are calculated by considering these age intervals together with a sedimentation rate of 0.4-0.6 mm/yr. Sinuosity of present-day and paleo-river valleys is determined from Figures 5 and 10. Maximum excess incision related to sinuosity variations is measured upstream of our study area in the case of T2 and T3, but behind the Hotan anticline in the case of T1 (Figure 10). Uplift is retrieved where it is highest above the blind footwall ramps. It is then translated into fault slip using equation (4). For uplift and slip, most probable values are indicated (average), together with values if larger uncertainties are considered (*extended*), corresponding to continuous and dashed boxes in Figures 12 and 13, respectively.

Given the results and interpretations proposed for terraces T2 and T3, and following the idea that terrace abandonment relates to the regional climatic evolution as proposed in Pishan [*Guilbaud et al.*, 2017], we propose that terrace T1 has a probable age of 30-60 ka (Table 3). The proposed time span is here purposely conservatively large to account for the fact that we have no absolute tight age constraints on T1. The reasoning is more difficult to apply with confidence to terrace levels older than T3: in our subsequent analysis, we will therefore mostly rely on terrace levels T1 to T3, which are the best and most continuously preserved along the Karakash River (Figures 5 and 6), as well as those with direct or indirect chronological constraints (Tables 2 and 3).

5 Kinematics of deformation

5.1 General approach

Because the overall geomorphology of the study site is primarily controlled by active tectonics, we expect terrace incision to picture approximately tectonic uplift cumulated since terrace abandonment.

Where terraces are offset by a fault, the vertical fault throw can be easily determined by comparing the position (altitude or incision) of the disrupted markers on either side of it. Over a much larger spatial scale or when the position of the terraces (or equivalent former riverbeds) is not directly observable in the fault footwall, a complementary approach is followed. Following [*Lavé and Avouac*, 2000], the pattern of incremental uplift U since terrace abandonment can be quantified from terrace incision I from:

$$U = I + D - \Delta I \quad (3)$$

where D is the river base level change (positive in the case of sedimentation), and ΔI is the excess incision related to changes in river sinuosity or gradient (positive in the case of an excess of incision) (Figure 8). Uplift is here given relative to the fault footwall (structural uplift). Variations in lithospheric subsidence across the investigated fault systems are neglected given the length scale of these structures relative to that of the whole flexural basin (Figure 1c) and the flexural rigidity of the Tarim Block [*Lyon-Caen and Molnar*, 1984].

Once structural uplift is determined locally across a fault scarp or over a much larger spatial scale, the associated slip on the fault can be assessed using a kinematic model of faulting and folding. In the case of fault-bend folding with bedding-plane slip, as derived here from existing structural constraints on the Hotan anticline [*Baby et al.*, 2022; *X Cheng et al.*, 2017; *X Jiang et al.*, 2013] (Figure 3), it follows that:

$$U = R \,.\, \sin\alpha \quad (4)$$

where R is the incremental slip on the fault plane since terrace abandonment, and α the underlying local fault dip angle reported to the surface [*Bernard et al.*, 2007; *Lavé and Avouac*, 2000] (Figure 8). This approach is applicable to any terrace record, even though spatially discontinuous, as long as the geometry of the underlying active fault is known. Finally, the fault slip rate is derived by comparing incremental slip and terrace ages.

5.2 Kinematics of deformation across the Hotan anticline

5.2.1 Quantifying incremental uplift from terrace incision

To quantify the recent kinematics of the faults underlying the Hotan anticline, we first derive incremental structural uplift from equation (3) (Figure 8) by correcting terrace incision for changes in river base level, gradient and sinuosity.

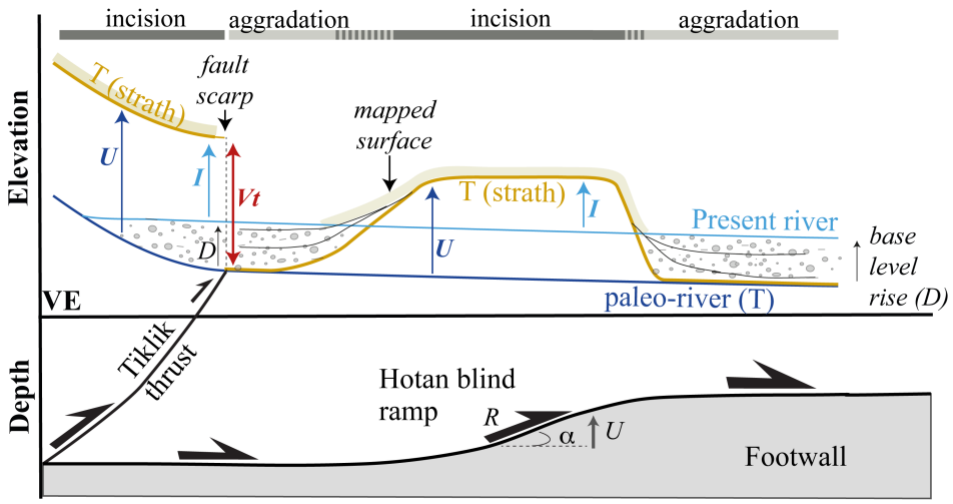

Figure 8 General principle of our morphotectonic approach (after [*Lavé and Avouac*, 2000]). The case of a terrace *T* record is taken as an example. Once the paleo-riverbed corresponding to *T* (dark blue line) is abandoned, it becomes a geomorphic marker (orange line) that is progressively deformed because of uplift *U* above the underlying faults (equation 4). This geomorphic marker is incised (*I*) by the active riverbed (light blue line), or is buried by aggradation as the river base level rises over time (*D*), depending on the local balance between uplift and sedimentation. As such the present-day river stands as a reference line. The deformed former riverbed (orange line) is an erosive surface where uplift and incision prevail (strath), but is a depositional surface where aggradation occurs. Because aggradation may be time-transgressive [*Weldon*, 1986], the aggradational mapped surface in geometrical continuity with the strath terrace *T* may be younger. Uplift can be determined by comparing the terrace record *T* to the geometry of the corresponding former riverbed, and is given here in a structural reference frame relative to the fixed fault footwall. Uplift can be approximated from terrace incision *I*, as long as it is corrected for base level rise *D* (equation 3). Across the Tiklik thrust, the vertical throw V_t since the abandonment of terrace T is here the sum of the incision *I* of the terrace in the thrust hanging wall and of the river base level rise *D* in the thrust footwall. Here the representation of river incision is simplified and does not integrate non-tectonic incision related to river sinuosity or gradient changes over time. Note that elevation (and the corresponding terrace record) is vertically exaggerated (VE) compared to the geometry of structures at depth.

5.2.1.1 River base level

Within our study site, the base level of the Karakash River is the endorheic Tarim foreland basin, immediately north of the Hotan anticline. We do not know of any data on the sedimentation rate in the basin at the time scale of our terrace record, encompassing probable climatically-induced variations during glacial and interglacial periods. To overcome this difficulty, we calculate a long-term sedimentation rate of ~0.5 mm.yr^{-1} over the last 5 Myr from the ~2.5 km thick Plio-Quaternary sediments immediately downstream of the river outlet within the Tarim foreland (Figures 3 and 6). This value should however be considered as a long-term minimum as we do not have the data needed to properly decompact the considered sediment thickness.

Estimating the uncertainties on this value is not straightforward, and we arbitrarily consider a wide possible range of ~0.4-0.6 $mm.yr^{-1}$ for the sedimentation rate at the base level of the Karakash River, with the idea of encompassing the various unknowns on this estimate. Possible time variations in the sedimentation rate at the several 100s kyr time scale of the terrace record should be smoothed out and the large uncertainty (i.e., ± 20%) stands in line with possible average porosity loss during sediment compaction in the Tarim (see supplementary text S2 in [*Laborde et al.*, 2019]). The considered range of sedimentation rates is overall consistent with the rates proposed in the Pishan area ~150 km further west [*Guilbaud et al.*, 2017], and with previous published local values in the region using decompacted well data [*Metivier and Gaudemer*, 1997].

Over a time interval of ~250 kyr, as considered here, the correction for sedimentation at the base level may rise up to ~125 m, a substantial value when compared to the maximum ~75 m of incision of terrace T3 downstream of the Tiklik thrust (Figure 6). The base level correction to be considered for each terrace is calculated and reported in Table 3.

5.2.1.2 River gradient

The present-day gradient of the Karakash River is of 0.7 %. A change in river gradient over time is expressed by: (1) an excess of incision upstream and sedimentation downstream in the case of a decreasing gradient; or (2) an excess of incision downstream and sedimentation upstream for an increasing gradient [*Lavé and Avouac*, 2000]. At the scale of the Hotan anticline, we do not have any evidence for such broad variations, independent of tectonics, in the incision pattern (Figure 6).

To further tentatively track variations in river gradient, we analyse terrace profiles along portions of the river course that are approximately parallel to the axis of the duplex ramps (i.e., perpendicular to section AA') with the idea that they are expected to have endured approximately constant uplift. Residual slopes in such profiles (relative to present river gradient and/or in between various terrace profiles), if existent, could be partly related to changes in river gradient over time [*Poisson and Avouac*, 2004; *Simoes et al.*, 2014].

We here consider the ~15-20 km long portion of the Karakash River flowing southeastward along the backlimb of the Hotan anticline (Figure 9). There, three smaller sections of the river flow approximately eastward, separated by others flowing approximately southward. The three eastward sections are located at different distances across strike (i.e., along section AA'), so that structural uplift may be approximated as constant within each one of them. Within each one of these sections, the profiles of terraces T1 to T2 are observed to be parallel to the present-day river when projected along an east-west axis perpendicular to AA' (red line in the inset of Figure 9), with no particular residual slope that could be related to a change in river gradient. This is also mostly the case for T3, except in the central river segment where a residual slope (relative to the present-day river) is observed. We verified that this slope is in fact an artefact as the highest T3 points sample here the top of a colluvial wedge along a T5-T3 riser (Figure 9). In the case of higher and older terraces, a residual slope is observed, which could be partly due to surface processes (in particular in the central segment) or be real. Given that our analysis will rely only on terraces T1 to T3, we hereafter neglect possible changes in river gradient since T3 abandonment.

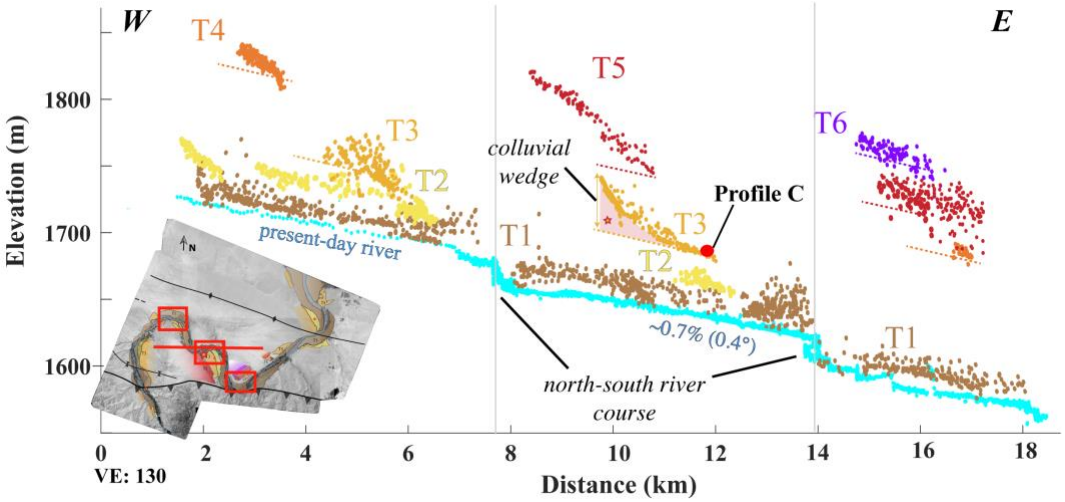

Figure 9 River and terraces along the backlimb of the Hotan anticline. The red frames in the lower left inset locate three segments where the river locally flows in a direction close to that of terrace folding (Figure 5). Within each of these three segments, terrace incision is therefore expected to have operated under a similar uplift rate. These segments are separated by portions of the river flowing in a north-south direction. River and terrace data are projected parallel to the axis of terrace folding (red line in inset map). Dashed colored lines report the local river gradient at the altitude of the terraces. A slight apparent excess gradient is observed for T3 in the case of the central river segment, but this is an artefact as these T3 points sample a colluvial wedge along a T5-T3 riser near Profile C (colored area in graph and small red star on the inset map). Overall, terraces T1 to T3 appear relatively parallel to the present-day river within each one of the east-west flowing segments, indicating that there has been no major change in river gradient since T3 abandonment.

5.2.1.3 River sinuosity

The geomorphological map of Figure 5 is suggestive of changes in valley sinuosity over time, in particular where meanders appear to have been amplified since the abandonment of T5-T3, such as nearby our depth-profiles C and D collected for the dating of T3 and T2, respectively. To put tighter constraints on these changes, we reconstruct river paleo-valleys and define past river valley sinuosities by using our geomorphological map (Figure 5) and by adapting the approach of [*Lavé and Avouac*, 2000] to our field conditions (Figure 10). For these reconstructions, we follow some simple rules: (1) for each time step, equivalent to the time just prior to terrace abandonment, we consider the associated terrace record, (2) the extent of the corresponding paleo-valley is confined within parts of the landscape where elevations are equal to, or lower than, that of the preserved remnants of the considered terrace level, and (3) we consider an average paleo-channel flowing within the middle of the reconstructed paleo-valley and quantify its sinuosity. We call here for a particular attention on the fact that we are only able to reconstruct paleo-valleys and not the various paleo-channels that once flew within these valleys. This nuance between river channels and river valley is illustrated by the present-day Karakash River: the present river flows through various channels, with a seasonal and yearly variability, that will tend to occupy alternatively over time the whole present-day active valley.

In other words, the whole river valley is not fully occupied at any time; extrapolating this observation to the past river record, this signifies that reconstructed past river courses may not flow through all their corresponding terrace remnants at once. The quantified sinuosities rather represent the sinuosities of the river valleys rather than that of the actual river channels. Therefore, for a proper comparison between present and past rivers, we define an average modern river course flowing through the center of the present river valley.

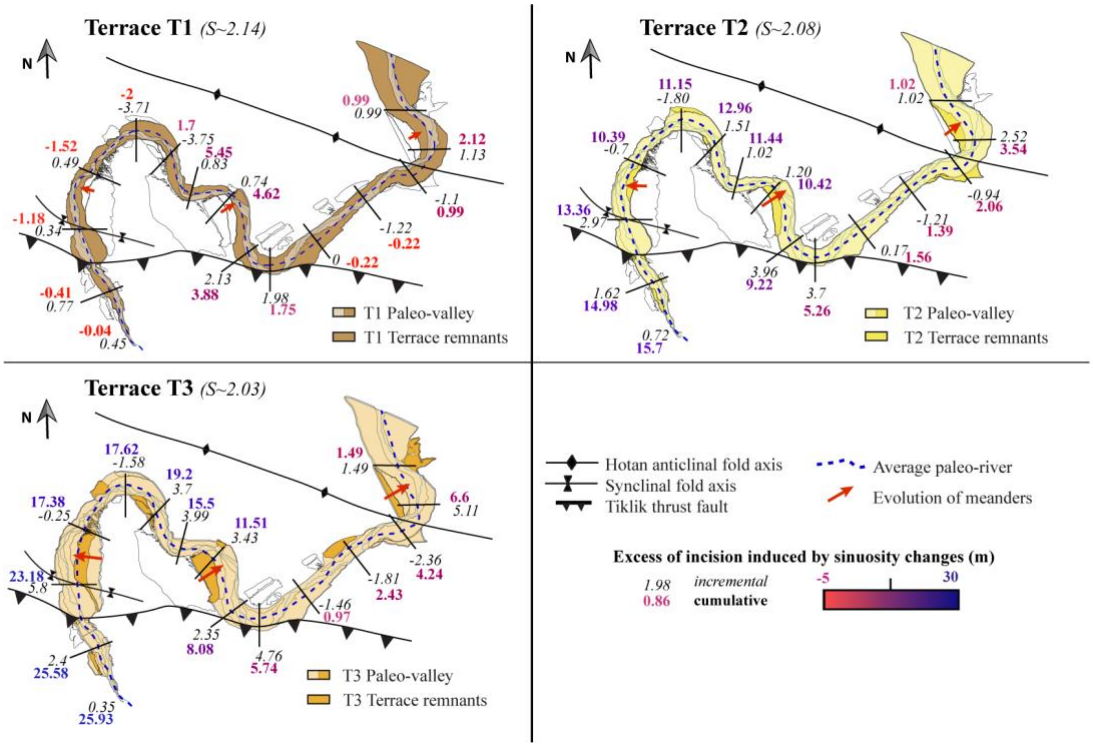

Figure 10 Reconstructed paleo-valleys, evolution of river sinuosity and associated excess incision. Panels represent the paleo-valley (colored areas) reconstructed from remnants of terraces T1 to T3 (deep colors). An average river course (dashed blue line) is determined as if flowing in the center of each paleo-valley. The reconstructed river course is segmented (dark cross-lines), and variations in river sinuosity and associated excess incision are calculated within each segment. Increments of excess incision from one segment to the other are reported (italic dark values, in meters), and cumulative ones (bold colored values, in meters) are determined by integrating all incremental values, upstream from base level.

Figure 10 shows the reconstructed valleys and average river courses for terraces T1 to T3. The paleo-valleys of T4, T5 and T6 could not be reconstructed since terrace remnants are too scarce or most often covered with loess or colluvium (Figures 4-5). The average river valley sinuosity S is derived from:

$$S = \frac{L}{D} \quad (5)$$

where L is the length of the average reconstructed channel and D is the downvalley path. The downvalley path is defined as the shortest direct distance between the considered downstream and upstream points. Here, from the river outlet into the Tarim Basin to the river outlet out of the inner range, we have a direct downvalley path of ~32 km. Calculated sinuosities are reported in Figure 10 and in Table 3. From there, we observe an overall increase in river valley sinuosity over time, from a sinuosity of ~2.03 in the case of T3 river to the present-day value of ~2.14.

The contribution of this increase in sinuosity to incision along the river course can be quantified from:

$$\Delta I_s = G \cdot \left(L_{x,t0} - L_{x,t}\right) \quad (6)$$

where ΔI_s is the excess incision related to changes in sinuosity, G the river gradient (in %), $L_{(x,t0)}$ and $L_{(x,t)}$ the river longitudinal distances at point x for present-day ($t0$) and paleo-rivers at time t, respectively. We remind here that considered river courses are taken from the average course within the center of the reconstructed river valleys. Longitudinal distances are determined upstream from base level, and point x is taken along the present-day river valley profile for reference. More precisely, we discretize the river course in various segments in which we compare average present-day and paleo-rivers to compute increments of ΔI_s from T1 to T3 within these segments (Figure 10). These increments of ΔI_s are then summed and integrated all along the river course to quantify the cumulated value of ΔI_s, upstream from base level.

The results are reported in Figure 10, and in Table 3. In the upstream portions of our study site, variations in sinuosity have resulted in ~25-30 m of excess incision at most over the last ~250 kyr. In fact, the incision of the fill terraces found in this area, just downstream of the Tiklik thrust, correlates well with this excess incision (Figures 11a-b) and may simply result from river sinuosity variations over time.

5.2.1.4 Incremental uplift

Incremental uplift since terrace abandonment is determined using equation (3) by following the long-distance profile of the Karakash River upstream from base level (Figure 11). All incision values are considered. Cumulative excess incision related to changes in sinuosity is attributed an arbitrary ~10% uncertainty, in the high range of the relative variation in sinuosity since T3 and by comparison to previous work [*Lavé and Avouac*, 2000] (Table 3). Corrections for base level integrate both the possible range of sedimentation rates, as well as the age intervals attributed to each terrace level (Table 3). Minimum uplift is determined for each related incision value by considering the minimum correction for base level (calculated from the minimum sedimentation rate of 0.4 mm/yr and the lower bound of attributed age) and the maximum excess incision related to sinuosity changes - and conversely, for maximum uplift. Overall, the range of values for calculated uplifts is most probably too large as uncertainties are most certainly conservatively overestimated.

Our computations reveal that base level changes contribute the most significantly to uplift, when compared to incision. As an example, incision related to the uplift of terrace T3 is of ~60 m in the zone of highest uplift behind the Hotan anticline (nearby depth-profile C, 28 km upstream from base level, Figure 11), when correcting the measured ~75 m incision (Figure 11a) for the ~15 m of incision related to variations in river sinuosity since T3 abandonment (Figure

11b). Comparatively, sedimentation at the base level amounts to ~125 m (Table 3, Figure 11c), that is ~2/3 of the total ~185 m uplift (Figure 11d).

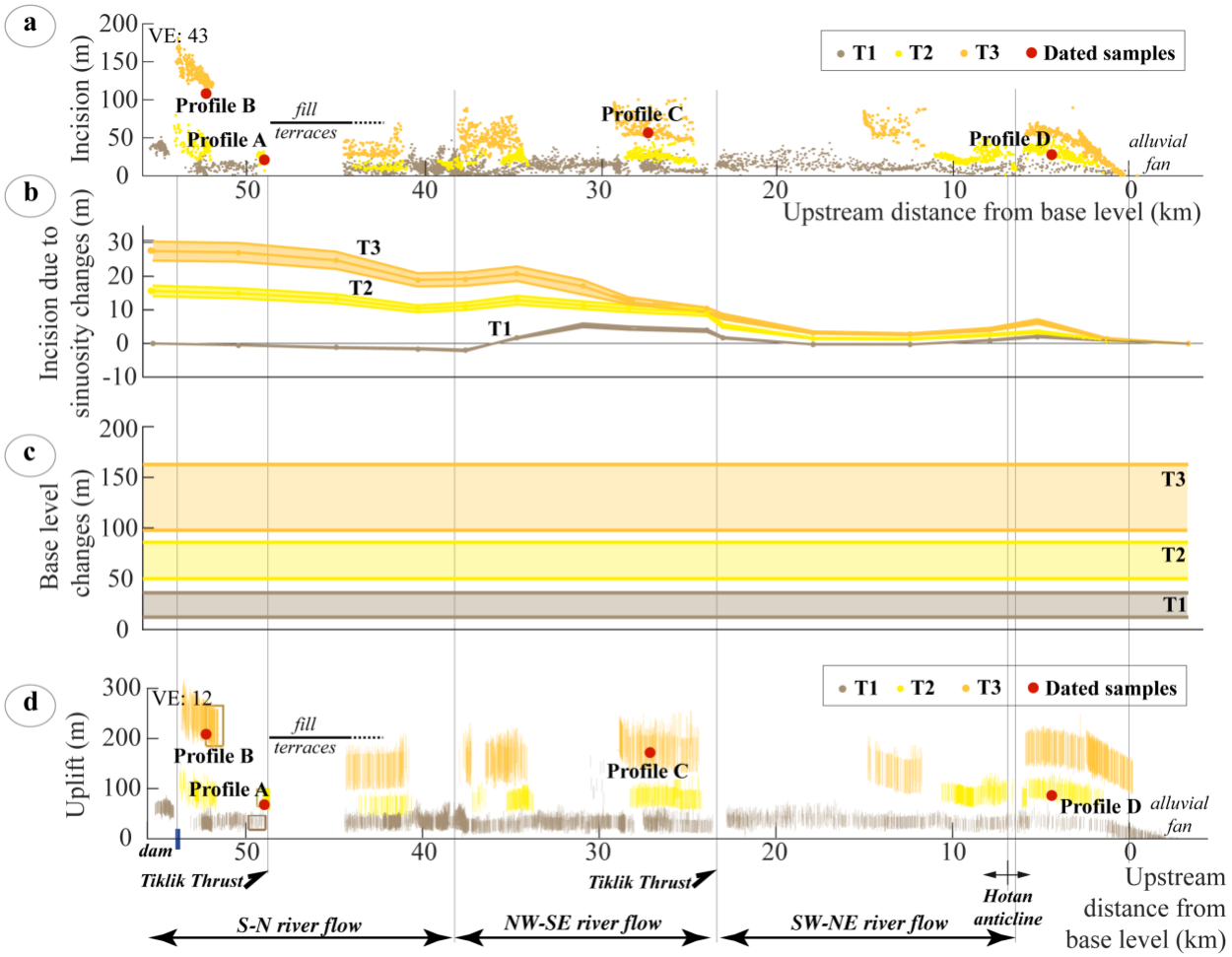

Figure 11 From terrace incision to structural uplift. Only the strath terraces of levels T1 to T3 are considered, along the long-distance river profile upstream from base level. Location of sampled depth profiles (Profiles A to D) are reported, together with that of main structural features encountered along the Karakash River course, in addition to the main directions of river flow, for reference. (a) Terrace incision as in Figure 6b, but reported here along the river course. (b) Cumulative excess of incision related to changes in river sinuosity over time (Figure 10). (c) Changes in base level, as deduced from the sedimentation rate and the interpreted ages of terrace abandonment (Table 3). (d) Structural uplift, calculated following equation (3) by correcting terrace incision (Figure 11a) from sedimentation at the base level (Figure 11c), and from incision related to sinuosity changes (Figure 11b). Vertical lines represent the range of uplift values found when considering minimum and maximum corrections for non-tectonic incision. Boxes in the hanging wall of the Tiklik thrust (to the left) indicate the values used to quantify the maximum vertical offset across this fault (Figure 14c).

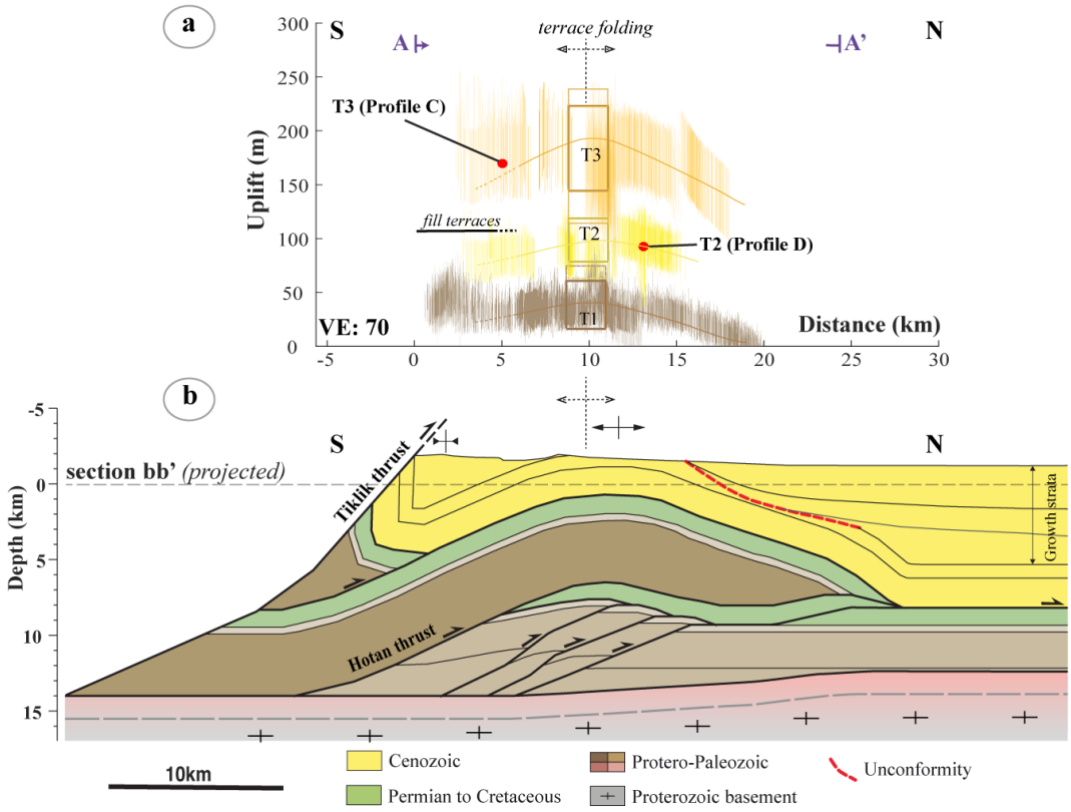

Figure 12 Structural uplift of river terraces (a) compared to the sub-surface structure of the Hotan anticline (b). Uplift is calculated from equation (3), as in Figure 11, but is here projected along section AA' (Figure 5). Because of possible lateral structural variations and because the limit between fill and strath terraces is not precisely constrained (Figure 5), the terraces along the northward flowing river segment, after the river flows out of the mountain range, are not considered here. Boxes indicate the range of uplift values considered for terraces T1 to T3 to determine the recent uplift and slip rates (Figure 13). A larger extent to these boxes is possible, in particular for terraces T2 and T3 (dashed lines), because of the higher uncertainties when deriving terrace incision in large river meanders. Only cross-section bb' is here projected along section AA' for reference

Uplift is then projected along section AA', perpendicular to suspected active structures (Figure 12). Because the limit between fill and strath terraces is not precisely defined from our field observations, we do not consider here the terraces located along the northward flowing river segment, immediately downstream of where the river flows out of the mountain range (Figure 5). A broad zone of uplift is found, indicative of anticlinal folding for the three terrace levels T1 to T3. The zone of highest incision delineated in Figure 6 by km 10 coincides with where uplift is also highest even after the various corrections applied to terrace incision (Figure 12). The forelimb of terrace anticlinal folding is well-defined, from km 10 to 20 along section AA' (Figure 12). Conversely, the backlimb of this anticline is not as well-depicted from km 0 to 10. This may relate to the fact that there may be stronger lateral structural variations along the backlimb, with the existence of a syncline at the back of the Hotan anticline to the west that disappears eastward (Figure 3). Also, we cannot exclude the possibility that the Hotan thrust has

been active over the time span of the terrace record and contributed to broad, even though possibly limited, uplift in this area. Overall, terrace anticlinal folding spatially coincides well to the first order with the ramps of the footwall duplex, confirming the idea that these structures have been active over the time span covered by the uplifted terraces.

5.2.2 Fault slip rate on the Hotan footwall duplex

We extract the range of maximum uplift for terrace levels T1 to T3 above the footwall duplex ramps (boxes in Figure 12), and compare it to terrace ages (Figure 13a). On average, the maximum uplift rate above the footwall ramps has been of 0.5-0.9 mm/yr over the last ~250 kyr. This range of uplift rate values could possibly be extended to ~0.4-1.0 mm/yr when accounting for the largest uncertainties on uplift estimates (dashed boxes on Figures 12-13).

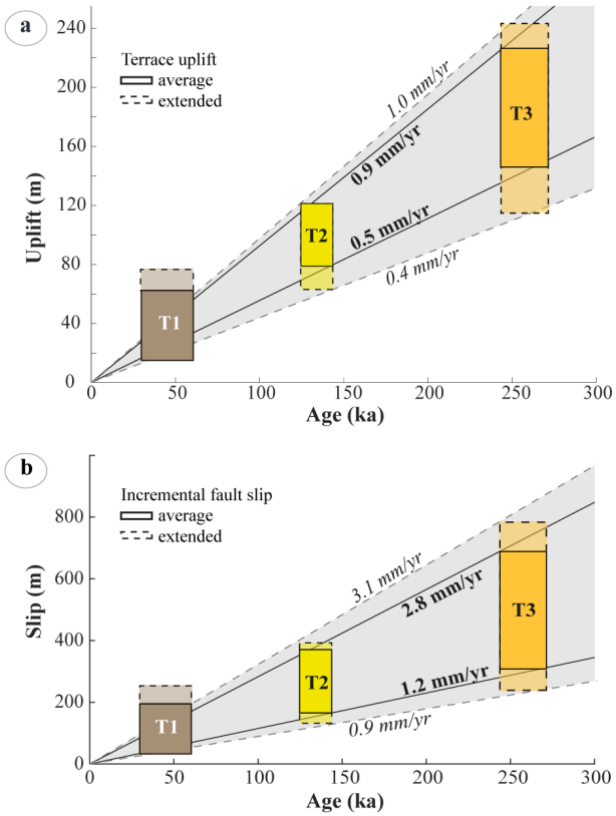

Figure 13 Uplift (a) and incremental fault slip (b) compared to terrace age. The range of considered terrace uplift is taken from the uplift determined above the ramps of the footwall duplex (boxes on Figure 12). The considered range of values can be extended when considering the largest uncertainties in uplift estimates (dashed boxes, here and Figure 12). Incremental fault slip is determined from terrace uplift and the dip angle of the underlying ramps following equation (4). We recall that only terraces T2 and T3 were dated, the age of T1 being estimated from regional considerations.

Terrace uplift is used to derive the incremental fault slip from equation (4) (Figure 13b). Because the pattern of terrace uplift is not sufficiently defined in detail, in particular in the backlimb of the anticline, we only consider uplift where it is maximum (boxes in Figure 12),

away from possible growth kink bands in the terrace record. The dip angles of the underlying blind duplex ramps are all measured to ~23-24°S on average (within the range 18-29°S) from available structural cross-sections projected along the direction of section AA' (Figure 12). The dip angles of the footwall ramps slightly increase from the most frontal to the most internal ones. However, all dip angles remain within a comparable value, so that we simplify the system and assimilate the duplex to one single ramp with an identical average dip angle of 18-29°S. Using equation (4), incremental fault slip is deduced from terrace uplift for each level T1-T3 (Figure 13b). Maximum fault slip values are determined from maximum uplift and minimum fault dip angle values, and conversely for minimum fault slip, so that the range of fault slip represented by the boxes on Figure 13b is probably too wide but conservative. These various results are reported on Table 3. When incremental slip is compared to terrace ages, an average fault slip rate of 1.2-2.8 mm/yr is found over the last ~250 kyr, a rate possibly from 0.9 to 3.1 mm/yr when accounting for the larger uncertainties on incision and uplift values (dashed boxes on Figure 13).

The broad pattern of terrace uplift does not allow to derive the detailed kinematics of the blind duplex ramps (Figure 12), i.e. whether all ramps are active or not, and how slip is partitioned between them. The fault slip rate of 1.2-2.8 mm/yr determined here is that on the overall duplex system, independently of the number and location of actual active ramps. This slip rate is that transmitted from the deeper Cambrian decollement at the back to the footwall duplex, and from there to the shallow Paleogene decollement northward and upward into the Tarim Basin.

5.3 Slip rate on the Tiklik thrust

The Tiklik fault is active, as indicated by the ~14 m high scarp where it crosses the Karakash River (Figure 4e). This scarp separates terrace levels T2 and T1 on the hanging-wall and footwall of the fault, respectively. In addition, it should be reminded that terraces immediately downstream of the Tiklik fault scarp were identified as fill terraces (Figure 4e), in contrast with the strath terraces observed in the hanging wall of the thrust fault or further downstream toward the Hotan anticline. These geomorphic features are not directly comparable as they indicate lateral changes in the river behaviour, from incision to aggradation.

First, we consider the northward flowing Karakash River segment to the west of our investigated area where the fault scarp is observed (Figure 14a). We laterally extrapolate the geometry of the top of the various terrace levels T1 to T3 on either side of the Tiklik thrust (Figure 14a) to quantify their apparent vertical offset, and combine these data with the fault scarp measured in the field (Figure 14b). From there, we derive a possible fault offset of ~4 m across T1, even though not clearly measurable. We get values of ~10 m and ~83 m for the offsets of T2 and T3, respectively (Figure 14b). When combined to terrace ages, we find an average vertical displacement rate of ~0.2-0.3 mm/yr, with a faster rate of ~0.6 mm/yr between T2 and T3 when compared to the rate of <0.1 mm/yr since T2 (Figure 14c). However, we cannot exclude the fact that the top of the fill terraces in lateral geometric continuity with the identified and dated strath terrace levels are not precisely of the same age, as fill terraces have been documented elsewhere to be time-transgressive [*Weldon*, 1986] (Figure 8). The above values may therefore represent apparent offsets and should be considered as minimizing the actual vertical throw across the Tiklik thrust.

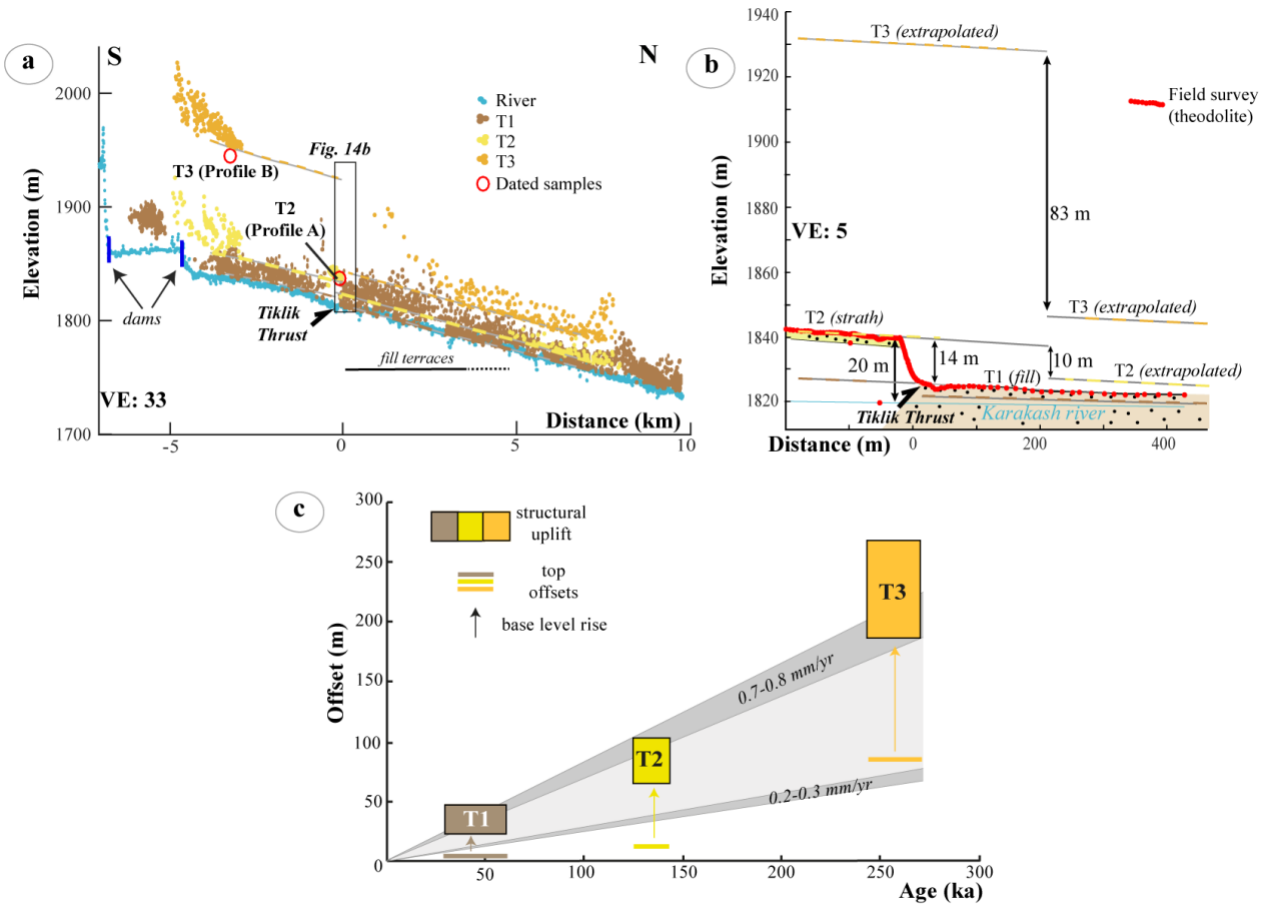

Figure 14 Analysis of terrace offsets across the Tiklik thrust. (a) River and terrace profiles, along the northward flowing segment of the Karakash River to the west of our study site (Figure 5). Elevation data are projected parallel to section AA', which is also approximately orthogonal to the Tiklik thrust. The dashed colored lines, following the color code of terrace data, extrapolate the geometry of the terrace surfaces towards the Tiklik thrust. Box locates Figure 14b. (b) Zoom into the area around the Tiklik fault scarp. A topographic theodolite profile (red points) documents the fault scarp, as well as the thickness of the T2 deposits or the elevation of the river in the fault hanging wall. These data are complemented by topographic data from available DEMs, in this area or extrapolated to it (dashed colored lines, from Figure 14a). Terraces are strath terraces on the hanging wall of the Tiklik fault, with <5m thick deposits, and are observed to be fill terraces in the fault footwall. (c) Vertical offsets across the Tiklik thrust, compared to terrace ages. Color-code represents terrace levels T1 to T3. Horizontal thick lines correspond to the offset of terrace surfaces extrapolated to the fault scarp (from Figures 14a-b). These values should be taken as minimum estimates of the actual fault offsets. Boxes represent the structural uplift of terraces, relative to the Tarim fixed footwall, as quantified in Figure 11d. These values should be taken as maximum estimates of the actual fault offsets. Altogether the uplift rate of the Tiklik thrust over its footwall is estimated to 0.2-0.8 mm/yr.

Indeed, the former riverbed, in continuity with a dated and investigated strath terrace level, is most probably buried within the fill terraces or below the present-day river in the

footwall of the Tiklik thrust. This burial amounts at most to the rise in river base level since terrace abandonment, in the case that there is no structural uplift of the Tiklik footwall behind the uplifting Hotan anticline during the considered time span. This situation is illustrated in Figure 8. In this case, the vertical throw of the paleo-river remnant across the Tiklik thrust can be calculated by adding the amount of base level rise in the footwall to that of terrace incision in the hanging wall, provided that this incision is corrected for non-tectonic parameters such as changes in river sinuosity and gradient. This calculation is equivalent to that of the structural uplift of terrace remnants in the hanging wall of the Tiklik thrust relative to the Tarim footwall, as illustrated in Figure 11. From this, we get maximum vertical throws of 20.7-44.8 m, 64.7-99.9 m and 186.5-265.0 m across the Tiklik thrust for terrace levels T1, T2 and T3, respectively (boxes in Figure 11d). When combined with terrace ages, we get an average maximum uplift rate of 0.7-0.8 mm/yr over the Tiklik thrust, with possible but limited evidence for variations of this rate over time (Figure 14c).

We cannot exclude a slight structural uplift of the immediate Tiklik footwall with respect to the Tarim footwall, behind the active ramps of the footwall duplex, or related to the Hotan thrust if still active. As such, we remind that the latter uplift values should be taken as maximizing the actual vertical throw of terraces across the Tiklik thrust and the derived uplift rate. The difference between this uplift rate and the formerly derived rate of 0.2-0.3 mm/yr from the offset of terrace surfaces resides in the ~0.5 mm/yr rise in base level at the fault footwall (Figure 14c).

To summarize, our data indicate an uplift rate in the range of 0.2-0.8 mm/yr over the Tiklik thrust over the last ~250 kyr (Figure 14c). The balanced cross-sections of [*Baby et al.*, 2022] indicate that the thrust dips 45-50°S. From equation (4), we therefore get that the Tiklik thrust has slipped at a rate of 0.3-1.1 mm/yr on average over this time period. In the details, with the available data, we cannot exclude that fault slip has not been steady over time, with higher rates from T3 to T2, i.e. from ~250 ka to ~130 ka -, and limited fault displacement since ~50-100 ka (Figure 14c).

6 Discussion

6.1 Kinematics of thrusting of the Tiklik Thrust

6.1.1 Uncertainties on our results

The Tiklik fault is segmented on various branches further west, at places even hidden below loess deposits (Figure 2a), and terminates rapidly further east towards the Altyn-Tagh strike-slip fault system (Figure 1). As such, field conditions are limited to provide direct fault slip rate estimates at sites other than the one investigated here, where the fault is well marked in the landscape by a scarp. One of the difficulties encountered here, though, lies in the fact that geomorphic markers on either side of the scarp are not directly comparable, with strath and fill terraces on the hanging-wall and footwall, respectively (Figure 14b). We overcome this difficulty by considering two extreme cases when analysing the terrace record, conservatively enclosing the fault slip rate within a minimum and a maximum value (Figure 14c).

6.1.2 Comparison to previous estimates

Along the Yurunkash River, ~50 km east of the fault scarp investigated here, apatite fission-track (AFT) ages from the broad basement anticline overthrusting the Tiklik fault record ~4-9 km of exhumation since the Late Oligocene, with proposed higher earlier rates up to the Early Miocene and more moderate exhumation since then [*X Cheng et al.*, 2017]. In more details, sample KLKS-7 of [*X Cheng et al.*, 2017], taken within the immediate hanging wall of the Tiklik thrust, has an AFT central age of ~22.5 Ma. This age is not well resolved as the sample did not pass the χ^2 test, possibly indicating that it was within the AFT partial annealing zone when exhumation initiated ~22.5 Myr ago. It is presently located ~300 m above the Tarim Basin base level, a value neglected hereafter with respect to estimates on exhumation and burial since 22.5 Ma. Considering a ~20° C/km geotherm, this sample suggests locally ~3-6 km of exhumation of the hanging wall of the Tiklik thrust above the base level for erosion since 22.5 Ma. On the footwall side of the thrust, the corresponding ~22.5 Ma old sedimentary horizon is presently buried at an estimated depth of ~6 km below base level along the mountain front (Figure 3). Altogether, this suggests a total vertical throw of ~9-12 km across the Tiklik thrust since ~ 22.5 Ma, a value in line with the possible minimum structural uplift of basement rocks on either side of the Tiklik thrust when considering that basement is at the surface in the hanging wall (Figure 2) and at a minimum depth of ~10 km in the footwall (Figure 3). This suggests an average long-term structural uplift rate of ~0.4-0.6 mm/yr over that time span. When considering the ~45-50°S dip angle of the fault down to the depth of ~10 km retrieved from balanced cross-sections (Figure 3), this translates into a long-term fault slip rate of ~0.5-0.9 mm/yr. These results are comparable to the rates derived here over a much shorter time span of ~250 kyr (Figure 14c). It suggests that the Tiklik Thrust has been active most probably continuously since the Miocene.

6.1.3 Contribution of the Tiklik thrust to crustal shortening

We documented here for the first time the recent slip rate on the Tiklik thrust, consistent with the long-term ~0.5-0.9 mm/yr rate deduced from thermochronological data and structural reasoning. Even though this fault is documented to dip at ~45-50°S down to a depth of ~10 km (Figure 3), it is expected to flatten at depth below the inner range (Figure 1c). Given this geometry, the ~0.5-0.9 mm/yr slip rate is used as a proxy for the shortening rate accommodated by the thrust. Over the last ~20 Myr, the Tiklik thrust has therefore absorbed a possible cumulated crustal shortening of ~10-18 km. This value is to be added to the shortening taken by the blind structures of the Western Kunlun foothills, which may reach values of 64 km as along section aa' across the Hotan anticline and Tiklik thrust [*Baby et al.*, 2022]. When compared to the total Cenozoic shortening of ~55-100 km estimated across the Western Kunlun Range by crustal mass balance budgets [*Baby et al.*, 2022; *Laborde et al.*, 2019], this confirms the idea that most of the crustal shortening has been absorbed in the foothills [*Baby et al.*, 2022], with some contribution of the Tiklik thrust at the front of the inner range.

6.2 Kinematics of shortening and active deformation across the Hotan anticline

6.2.1 Uncertainties on our results

Using the terrace uplift record (Figure 12), we obtained a 1.2-2.8 mm/yr fault slip rate on overall Hotan duplex system (Figure 13b). Most uncertainties on the data and hypotheses used to

derive this rate have been already discussed, step by step, while progressively reaching this result.

We were not able to derive the detailed kinematics of the blind duplex ramps, and the broad uplift pattern may be indicative that several of the duplex ramps are (or have been recently) active, in particular the most frontal ones, as proposed in Pishan further west [*Y Zhang et al.*, 2023]. Because the dip angle values of the various ramps derived from structural sections are comparable, and because the overall slip rate is to be partitioned onto the various active ramps, we simplified the duplex system into an analog single structure slipping at the total rate transmitted from the deeper Cambrian decollement into the shallower Paleocene one. We recognize that the most internal ramps are slightly steeper than the most frontal ones and could contribute more to the recorded uplift, from a simple geometrical argument (Figure 8). However, based on mechanical arguments, we may also consider that the overall slip partitioning is most favorable onto the more shallowly dipping frontal ramps. We believe, however, that these details only slightly impact the overall slip rate value retrieved here, and that they are already encompassed within the large conservative uncertainties on our estimates, in particular when considering a broad range of dip angles for the considered analog single ramp.

We also simplified our analysis by considering that tectonic deformation is cylindrical, even though there are evidence for lateral structural variations along the Hotan anticline (Figure 2) [*Baby et al.*, 2022]. However, [*Baby et al.*, 2022] found that these variations were in fact mostly related to the eastward progressive initiation of the blind duplex in the footwall of the Hotan thrust, and that the total shortening, the age of deformation inception and from there the long-term shortening rate across the whole Hotan anticline did not vary significantly along strike. At the scale of the investigated area, which extends over ~25-30 km along strike (Figure 5), major structural changes mostly rely on the presence of a syncline at the back of the duplex only along the western section bb', and in the eastward decreasing cumulated deformation of the duplex (Figure 3). Despite these variations and the extent of the area, we find that the pattern of terrace incision and uplift projects well onto a single broad antiform that correlates with the underlying duplex (Figures 6b-c and 12). This signifies that the lateral structural changes of the blind duplex and the potential lateral variations in its overall slip rate, if existent, are not sufficient to be resolved by the ~250 kyr long terrace record.

Finally, it should be reminded that terrace uplift is here mostly dominated by the significant amount of base level changes (Figure 11), determined from sedimentation rates over the last ~5 Myr, considered laterally constant since we have no indication for lateral or temporal changes in these rates in available cross-sections (Figure 3). Any variation in the pattern of terrace uplift related to the previously discussed unknowns are therefore expected to be smoothed by this substantial correction for base level, and should therefore be considered as encompassed within the conservatively derived uncertainties.

6.2.2 Reconciling the kinematics of the Hotan anticline over various time scales: evidence for the recent activity of the Hotan thrust to the east?

A 1.2-2.8 mm/yr slip rate is derived for the Hotan blind duplex, over a time span of ~250 kyr, with a range of rates that could be conservatively extended to values from 0.9 to 3.1 mm/yr (Figure 13b). Given the large uncertainties on this estimate (Figure 13b), these values are only an average and we cannot rule out any temporal variability within the ~250 kyr time span of the terrace record. These values are in any case significantly higher than the long-term <0.5 mm/yr

shortening rate proposed over the last ~8-9 Myr on the same duplex system from structural cross-sections [*Baby et al.*, 2022]. We have re-considered in detail the data used and the methods followed to reach each one of these results, independently, and did not find any particular reason to favor one more than the other as both analyses were found robust.

One possible explanation lies in the fact that these results encompass a different time duration. If the fault system alternates periods of tectonic quiescence and activity, rates may be highly variable over a shorter time scale, even though they are expected to average over time to the geological long-term value. In other terms, if applicable here, this would suggest that the Hotan duplex system has been particularly active over the last ~250 kyr, with rates 3 to 6 times faster than the geological longer-term (Myr time scale) rate of <0.5 mm/yr – also suggesting ~100 kyr long periods of relative inactivity prior to ~250 ka. Episodic fault activity and related variable slip rates have been documented in various contexts since the first observations by Wallace [*Wallace*, 1987], and were attributed to variations in fault stresses or properties related to external climatic forcing (e.g. [*Calais et al.*, 2010; *Chéry and Vernant*, 2006; *Hetzel and Hampel*, 2005; *Luttrell and Sandwell*, 2010]), to variations in the strength of the fault zone or of the lithosphere, and/or to fault interactions (e.g. [*Chéry et al.*, 2001; *Chéry and Vernant*, 2006; *Dolan et al.*, 2007; *Dolan and Meade*, 2017; *Gunderson et al.*, 2018; *Peltzer et al.*, 2001]). However, such episodic fault activity has been documented in most cases over shorter millennial time scales (i.e. from geodetic time scales to few 1-10s kyrs). If real, the variations in rates documented in Hotan would therefore take place over a much longer time span than most often documented on continental active faults, and may call for other causal intrinsic processes, possibly related to the initiation and accretion of each duplex slice (e.g. [*Hoth et al.*, 2007; *Menant et al.*, 2020]), or to variable strain partitioning on connected thrusts [*Gunderson et al.*, 2018].

Interestingly, even though the 1.2-2.8 mm/yr rate derived over the last ~250 kyr is significantly higher than the one proposed over the last ~8-9 Myr by [*Baby et al.*, 2022], it coincidently compares well with the longer-term geological average of ~2.2-2.5 mm/yr when considering the 35-40 km total shortening across the Hotan anticline and the 16 Ma time of deformation initiation [*Baby et al.*, 2022] (Figure 15). We recall here that [*Baby et al.*, 2022] hypothesized that thrusting over the Hotan thrust fully ended with the initiation of footwall duplexing, using this change in tectonic style as a marker of ongoing deformation. However, this change in tectonic style may not have been sharp in time but progressive, raising the possibility that basement thrusting has remained active together with footwall duplexing for a certain time, during a transitional period, as long as the basement thrust has not been significantly deformed by the underlying duplex. This situation would imply that not all the shortening attributed to the Hotan thrust from cross-sections had been consumed prior to footwall duplexing, but that some remained to be accommodated afterwards. Indeed, if this had been the case, ~10-15 km of shortening on the Hotan thrust needs to have been absorbed after the footwall duplex initiated, during a ~5-8 Myr long transitional period, to keep the long-term average shortening rate constant at ~2 mm/yr (Figure 15).

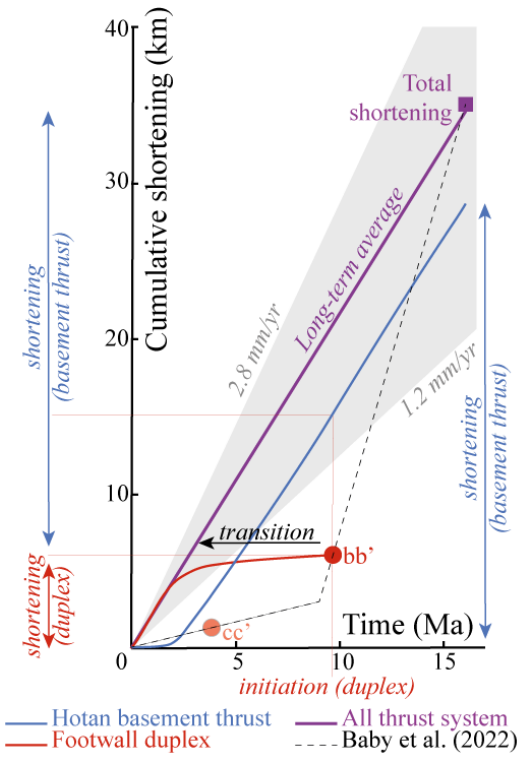

Figure 15 Long-term kinematics of shortening across the Hotan anticline, re-evaluated from our results on fault slip rates over the last ~250 kyr. The case of structural cross-section bb' [*Baby et al.*, 2022] is illustrated here. The data on total shortening and time of overall deformation initiation (purple square) across the anticline is reported, together with the shortening accommodated by the footwall duplex and its timing of initiation (red circle). In case the initiation of thrusting on the Hotan thrust abruptly ends when duplexing initiates, such data on section bb' and other sections studied by [*Baby et al.*, 2022] (such as cc' reported here in light red) indicate fast initial shortening rates, decelerating to slower rates by 8-9 Myr (dashed lines). However, in case deformation is progressively transferred from the Hotan thrust (blue line) to the footwall duplex (red line), over time during a transitional period (arrow), it might be possible that the overall shortening rates remain constant over time, at the long-term geological rate (purple line). The slip rate determined over the last ~250 kyr from terrace uplift is illustrated by the grey area.

Figure 15 illustrates our latter reasoning for section bb', to the west of the area investigated here. When also applied to section cc' further east, it raises the question as to whether the Hotan thrust remains presently active along this section, given the fact that the duplex initiated only ~4 Myr ago here [*Baby et al.*, 2022]. We have no evidence for significant lateral variations in terrace folding and uplift along the Karakash River, suggesting that the recent kinematics of the footwall duplex is laterally comparable over structural sections bb' and cc', given the resolution of our data. If still active, the Hotan thrust is therefore expected to only accommodate a limited slip rate along section cc', not resolvable from our terrace analysis. Further east (section dd' of [*Baby et al.*, 2022], east of Hotan City and of the Yurunkash River), the footwall duplex is absent and we might speculate that the Hotan thrust is here active at a rate

of, at most, the value estimated from the folded terraces along the Karakash River, or maybe less, as the overall Hotan anticline vanishes eastward (Figure 2).

To summarize, even though we cannot rule out episodic fault slip on the structures forming the Hotan anticline at the 1s-100s kyr time scale, we favor the idea that our rate estimates and those by [*Baby et al.*, 2022] can be reconciled by considering a progressive transfer of slip and deformation from the Hotan thrust to the various ramps forming the footwall duplex. A similar situation, with a progressive forward transfer of deformation between structures, has been also proposed for the Yecheng-Pishan anticline, based on the similar observation that the recent slip rate derived from terraces is higher than the rate derived from only the most recent and frontal blind duplex ramp, even though the recent and long-term average rates are consistent [*Guilbaud et al.*, 2017] – an idea further corroborated in Pishan by the broad terrace pattern [*Y Zhang et al.*, 2023]. In the westernmost portions of the Hotan anticline, we therefore expect that only the duplex is presently active, as cumulative deformation of the basement thrust mechanically impedes slip on it. However, at the eastern termination of the anticline, this thrust is only slightly deformed - or even the unique structure beneath the Hotan anticline – and is therefore expected to be active. The transition between these two styles of active structures beneath the Hotan anticline is expected to be somewhere nearby section cc' of [*Baby et al.*, 2022], or slightly further east (Figure 2).

The deceleration of shortening rates across the Hotan anticline ~8-9 Myr ago proposed by [*Baby et al.*, 2022] could therefore be an artefact, resulting from the progressive transfer of deformation from the Hotan thrust to the ramps of the footwall duplex, in time and in space, in a complex system where all structures are blind (Figure 15). The regional kinematic reorganization deduced by [*Baby et al.*, 2022] from this deceleration is therefore also to be questioned, even though other detailed investigations, on other structures or locally in Hotan from better-resolved seismic data on growth strata or from higher and older fluvial terraces, would be needed to fully resolve this issue. In any case, the comparison between rates of deformation at various time scales, from long-term geological estimates to more recent Quaternary data, proves to be insightful by overcoming the limits of each approach to better reveal the presently active structures, their lateral extent and their slip rates.

6.3 Active deformation and seismic segmentation along the mountain front of the Western Kunlun range

Geomorphology indicates that the Tiklik thrust and the blind ramps of the duplex below the Hotan anticline are active, and therefore possibly seismic. This is also the case for the other blind ramps, connecting the Cambrian to the Paleogene decollements all along the Western Kunlun foothills, such as below the Yecheng-Pishan anticline [*Guilbaud et al.*, 2017; *J Xu et al.*, 2020]. A slip rate of 0.5 to 3.9 mm/yr has been proposed over the last ~300-500 kyr on the frontal blind ramp below the Pishan anticline, with most probable values of ~2-2.5 mm/yr when comparing all published estimates [*Guilbaud et al.*, 2017; *J Xu et al.*, 2020]. These rates are consistent with our findings in Hotan (Figures 13b), indicating that there may not be significant lateral variations in the recent slip rate on the blind ramps all along the Western Kunlun foothills, at least from Pishan to Hotan, and within the resolution of available geomorphic data.

Even though slip rates have consistent values and are accommodated by frontal ramps that have comparable structural positions all along the mountain front, there may be a strong structural and kinematic lateral segmentation in the way recent deformation is absorbed. Indeed,

geomorphology indicates that the most frontal blind ramp below the Pishan anticline, which ruptured during the 2015 Pishan earthquake, is most probably the only one to be presently active [*Guilbaud et al.*, 2017; *J Xu et al.*, 2020; *Y Zhang et al.*, 2023]. In Hotan, we cannot discard the possibility that several of the blind footwall ramps are active together (Figure 12b) and that there may be some lateral variations in the actual active ramps below the anticline, in a context where these ramps have been propagating forward into the Tarim foreland basin and eastward towards the lateral termination of the anticline [*Baby et al.*, 2022]. In fact, the exact lateral extent of each blind ramp, either in Hotan or all along the mountain foothills, is unknown. In addition, as discussed in section 6.2.2, the blind Hotan thrust could remain active at places, in particular along a <40 km long segment east of the section cc' across the anticline (Figure 2). Altogether, this indicates that active deformation is taken by one or several different active blind structures all along the mountain front, even though all these structures have a similar structural position by connecting the Cambrian and the Paleogene decollements, and even though they accommodate together a comparable slip rate at the time scale of several seismic cycles.

This situation results in the fact that the kinematics of active deformation is probably more segmented along the mountain foothills than suspected from surface geology (Figure 2), as slip is distributed on various of the blind structures that all have a limited lateral extension. Because seismic ruptures may be subdued by structural complexities, as observed in other contexts (e.g., [*Cubas et al.*, 2022; *Hubbard et al.*, 2016; *King and Nabelek*, 1985; *Wesnousky*, 2006]), such segmentation in the way active deformation is absorbed all along the Western Kunlun foothills may limit the magnitude of the earthquakes that release the cumulated crustal stresses, at least partly. As a matter of fact, the recorded historical seismicity is rather moderate, with ~10-15 thrust earthquakes with magnitudes Mw5-6 since the 1950's (US Geological Survey, 2023, Earthquake Catalog), the 2015 Mw 6.4 Pishan earthquake being the largest recent event recorded in the area (Figure 1).

[*Guilbaud et al.*, 2017] determined that an earthquake like Pishan is expected to rupture the same patch every ~200 years, given the average ~40 cm coseismic slip [*He et al.*, 2016; *Wen et al.*, 2016] and the ~2 mm/yr long-term slip rate on the frontal blind ramps. A more integrated view on the seismicity over the whole length of the Western Kunlun foothills may be provided by comparing the potency rate (integral of the fault slip rate over the fault area) over this region to the coseismic potency of the Pishan earthquake (coseismic slip over the ruptured area) (e.g., [*Simoes et al.*, 2007]). We get a potency rate of ~9.10^6 m^3/yr over the whole ~ 300 km long foothills from Hotan to Yecheng, by considering ~15 km wide blind ramps slipping over the long-term at a rate of ~2 mm/yr. Given the ~40 x 20 km^2 patch that ruptured during the Pishan earthquake with an average coseismic slip of ~40 cm [*He et al.*, 2016; *Wen et al.*, 2016], this earthquake is found to have released a potency of ~$3.8.10^8$ m^3. Given these results, we find that Pishan-like earthquakes are expected to occur every ~35 years all along the foothills – or longer in case slip is not released only during earthquakes. This recurrence time is slightly higher than that suggested from observations since the 1950s from global catalogs (US Geological Survey, 2023, Earthquake Catalog), even though the ~60-70 years time window of observation is probably too short to conclude on a possible deficit of Mw6 (or higher) earthquakes.

While the Tiklik thrust reaches the surface, the blind structures below the various anticlines forming the foothills connect upward onto the Paleogene decollement. As such, slip is transmitted northward and reaches the surface at the Mazar Tagh deformation front (Figure 1c). This situation kinematically implies that the Mazar Tagh thrust sheet is also active [*Guilbaud et*

al., 2017], with a slip rate of similarly ~2-2.5 mm/yr. In contrast with the structural and kinematic segmentation of the foothills, the geometry of the active Mazar Tagh thrust sheet appears remarkably simple, with a ~150-180 km wide and ~350 km long continuously shallowly dipping basal decollement (Figures 1b-c), only slightly deformed locally at places [*Chen et al.*, 2022]. In other contexts, wide and smooth fault geometries have been proposed to favor the rupture of mega-earthquakes (e.g., [*Bletery et al.*, 2016; *Cubas et al.*, 2022]). If interseismically locked, the Mazar Tagh thrust sheet could therefore possibly slip during rare but major earthquakes, as hinted by its dimensions and its structural simplicity, with recurrence times of at least ~1.6-2 kyr [*Guilbaud et al.*, 2017]. Such situation would suggest the possibility of a bimodal seismic behavior, as proposed for instance in the Himalayas [*Bilham*, 2019; *Dal Zilio et al.*, 2019], with on one hand relatively frequent moderate earthquakes that rupture the segmented deeper blind structures of the foothills and that transmit crustal stresses upward, and on the other hand rare major earthquakes rupturing the wide frontal Mazar Tagh thrust sheet. Further elucidating this question will require in the future to document the interseismic mechanical behavior of the Mazar Tagh thrust and explore the geological record of potential past major earthquakes in the region.

7 Conclusions

We analysed the incision of terraces along the Karakash River, where this river crosses the Hotan anticline along the eastern foothills of the Western Kunlun mountain range (Figure 5). From samples collected in the field within depth-profiles for in-situ produced ^{10}Be cosmogenic isotope dating, we determined the ages of two main recent terrace levels (Figure 7). From there, we quantified structural uplift (Figure 11) and the slip on the underlying blind structures since these terraces were abandoned. These various results indicate a slip rate of 1.2-2.8 mm/yr on the blind ramps of a duplex beneath the Hotan anticline over the last ~250 kyr (Figures 12-13). In addition, the Tiklik thrust, which separates the inner range from the foothills, forms a clear morphologic scarp that disrupts the terrace record. Our analysis and age results suggest that this thrust slipped at a rate of 0.3-1.1 mm/yr over the same time period (Figure 14).

The slip rate determined on the blind ramps beneath the Hotan anticline over the last ~250 kyr is 3-6 times faster than the average shortening and slip rates derived across the same structures over the last ~8-9 Myr from structural sections [*Baby et al.*, 2022]. We propose that this discrepancy reflects the progressive transfer of deformation from the Hotan basement thrust to the footwall duplex, over a probable time span of ~5 Myr after the duplex initiates (Figure 15). This may suggest that the Hotan thrust remains active east of our study area, where the blind duplex is absent or incipient.

When compared to existing data further west in Pishan [*Guilbaud et al.*, 2017; *J Xu et al.*, 2020], our findings reveal that the blind structures all along the mountain foothills are active and slip at an overall rate of ~2 mm/yr. However, in the details, this kinematics is expected to endure a certain geometric segmentation, because of the possible partitioning of slip among several of the most frontal ramps, and because of the possibly limited lateral geometric extent of each structure. The ~2 mm/yr slip rate is then transferred upward and northward onto the shallowly dipping Paleogene decollement, all the way to the Mazar Tagh deformation front. This ~150-180 km wide structure has a simple structural geometry that contrasts with the kinematic segmentation suggested for the blind ramps forming the mountain front (Figure 1). We suggest that this segmentation may explain partly the moderate seismicity recorded all along the

mountain front. From there, we also question the possibility of a bimodal seismicity in the case of the Western Kunlun, as proposed in other contexts (e.g. [*Bilham*, 2019; *Cubas et al.*, 2022; *Dal Zilio et al.*, 2019]), with rare large (M >8) earthquakes rupturing the Mazar Tagh thrust sheet.

Acknowledgments

CG benefited from a PhD grant from the Ministère de l'Enseignement Supérieur et de la Recherche (MESR). This study was initiated thanks to a financial support from the Institut National des Sciences de l'Univers - Centre National de la Recherche Scientifique (INSU – CNRS) ALEAS (PI: MS) and SYSTER (PI: LB) programs, from the Institut de physique du globe de Paris (IPGP - PI: MS), and from a travel support from the Program Hubert Curien Xu Guangqi (PI: MS). It then benefited from the financial support of the Agence Nationale de la Recherche (ANR SLOWDEF, grant ANR-18-CE31-0008, PI: MS), and from the support of the China Geological Survey (grant DD20221630).
We thank the ASTER Team (G. Aumaître, K. Keddadouche, F. Zaïdi) for the AMS measurements performed at the ASTER French national facility in CEREGE (Centre Européen de Recherche et d'Enseignement des Géosciences de l'Environnement, Aix-en-Provence). ASTER is supported by the Institut National des Sciences de l'Univers - Centre National de la Recherche Scientifique (INSU - CNRS) and Institut de Recherche et Développement (IRD), member of University of Aix-Marseille platforms and REGEF networks (Réseau Géochimique et Expérimental Français, https://www.regef.fr). We also thank ITES (UMR 7063 Université de Strasbourg/CNRS) for access to various facilities, and R. Boutin for ICP-MS measurements. Finally, the writing of this manuscript benefitted from the thoughtful comments of two anonymous reviewers. This study contributes to the IdEx Université de Paris ANR-18-IDEX-0001. It initiated a long time ago thanks to the scientific impulse by late Paul Tapponnier.

Open Research

Pléiades satellite imagery (https://earth.esa.int/eogateway/missions/pleiades, last access: January 2018) was obtained through the ISIS program of the CNES under an academic license and is not available for open distribution. On request, the DEMs calculated from this imagery can be provided to any academic researcher, but only after approval from the CNES (contact: isis-pleiades@cnes.fr, with copy to simoes@ipgp.fr and referring to this paper). Numerical computations for the DEMs were performed using the free and open-source MicMac software suite [*Rosu et al.*, 2015; *Rupnik et al.*, 2017] freely available at https://micmac.ensg.eu/index.php (last access: April 2018). We completed our topographic data with the ALOS World 3D – 30m digital elevation model provided by the Japanese Aerospace Exploration Agency freely accessible at https://www.eorc.jaxa.jp/ALOS/en/aw3d30/index.htm (last access: April 2018). We also refer in this work to the US Geologigal Survey Earthquake Catalog, freely accessible at https://earthquake.usgs.gov/earthquakes/search/ (last accessed: January 2024). The data collected in this study is provided throughout the main text and in the supplementary material.

References

Ackerer, J., F. Chabaux, J. Van der Woerd, D. Viville, E. Pelt, E. Kali, C. Lerouge, P. Ackerer, R. di Chiara Roupert, and P. Ne Grel (2016), Regolith evolution on the millennial timescale from combined UeTheRa isotopes and in situ cosmogenic 10Be analysis in a weathering profile (Strengbach catchment, France), Earth and Planetary Science Letters, 453, 33-43.

Ainscoe, E., J. Elliott, A. Copley, T. Craig, T. Li, B. Parsons, and R. Walker (2017), Blind thrusting, surface folding, and the development of geological structure in the Mw 6.3 2015 Pishan (China) earthquake, *Journal of Geophysical Research: Solid Earth*, *122*(11), 9359-9382, doi:10.1002/2017JB014268.

Allegre, C. o., V. Courtillot, P. Tapponnier, A. Hirn, M. Mattauer, C. Coulon, J. Jaeger, J. Achache, U. Schärer, and J. Marcoux (1984), Structure and evolution of the Himalaya–Tibet orogenic belt, *Nature*, *307*(5946), 17-22.

ALOS World 3D - 30m (AW3D30) (April 2018) [Dataset].
https://www.eorc.jaxa.jp/ALOS/en/dataset/aw3d30/aw3d30_e.htm

Anderson, R. S., J. L. Repka, and G. S. Dick (1996), Explicit treatment of inheritance in dating depositional surfaces using in situ 10Be and 26Al, *Geology*, *24*(1), 47-51, doi:10.1130/0091-7613(1996)024<0047:ETOIID>2.3.CO;2.

Baby, G., M. Simoes, L. Barrier, C. Guilbaud, H. Li, and J. van der Woerd (2022), Kinematics of Cenozoic shortening of the Hotan anticline along the northwestern margin of the Tibetan Plateau (Western Kunlun, China). *Tectonics*, *41*, e2021TC006928, doi:10.1029/2021TC006928.

Balco, G. (2017), Production rate calculations for cosmic-ray-muon-produced 10Be and 26Al benchmarked against geological calibration data, *Quaternary Geochronology*, *39*, 150-173, doi:10.1016/j.quageo.2017.02.001.

Balco, G., and C. W. Rovey (2008), An isochron method for cosmogenic-nuclide dating of buried soils and sediments, *American Journal of Science*, *308*(10), 1083-1114, doi:10.2475/10.2008.02.

Balco, G., J. O. Stone, N. A. Lifton, and T. J. Dunai (2008), A complete and easily accessible means of calculating surface exposure ages or erosion rates from 10Be and 26Al measurements., Quaternary Geochronology, 3, 174-195.

Belmont, P., F. Pazzaglia, and J. C. Gosse (2007), Cosmogenic 10Be as a tracer for hillslope and channel sediment dynamics in the Clearwater River, western Washington State, *Earth and Planetary Science Letters*, *264*(1-2), 123-135, doi:10.1016/j.epsl.2007.09.013.

Benedetti, L., P. Tapponnier, G. C. King, B. Meyer, and I. Manighetti (2000), Growth folding and active thrusting in the Montello region, Veneto, northern Italy, *Journal of Geophysical Research: Solid Earth*, *105*(B1), 739-766, doi:10.1029/1999JB900222.

Bernard, S., J. P. Avouac, S. Dominguez, and M. Simoes (2007), Kinematics of fault-related folding derived from a sandbox experiment., *Journal of Geophysical Research*, *112*(B3), doi:10.1029/2005JB004149.

Bevington, P. R., and D. K. Robinson (2003), Data reduction and error analysis, *McGrawâ€“Hill, New York*.

Bilham, R. (2019), Himalayan earthquakes: a review of historical seismicity and early 21st century slip potential, *Geological Societyof London, Special Publications*, *483*, 423-482, doi:10.1144/SP483.1.

Blayney, T., G. Dupont-Nivet, Y. Najman, J. N. Proust, N. Meijer, P. Roperch, E. R. Sobel, I. Millar, and Z. Guo (2019), Tectonic evolution of the Pamir recorded in the Western Tarim Basin (China): Sedimentologic and magnetostratigraphic analyses of the Aertashi section, *Tectonics*, *38*(2), 492-515, doi:10.1029/2018TC005146.

Bletery, Q., A. M. Thomas, A. W. Rempel, L. Karlstrom, A. Sladen, and L. De Barros (2016), Mega-earthquakes rupture flat megathrusts, *Science*, *354*(6315), 1027-1031, doi:10.1126/science.aag0482.

Bollinger, L., P. Henry, and J.-P. Avouac (2006), Mountain building in the Nepal Himalaya: Thermal and kinematic model., *Earth and Planetary Science Letters*, *244*(58-71).

Borchers, B., S. Marrero, G. Balco, M. Caffee, B. Goehring, N. Lifton, K. Nishiizumi, F. Phillips, J. Schaefer, and J. Stone (2016), Geological calibration of spallation production rates in the CRONUS-Earth project, *Quaternary Geochronology*, *31*, 188-198, doi:10.1016/j.quageo.2015.01.009.

Bosboom, R., G. Dupont-Nivet, A. Grothe, H. Brinkhuis, G. Villa, O. Mandic, M. Stoica, W. Huang, W. Yang, and Z. Guo (2014), Linking Tarim Basin sea retreat (west China) and Asian aridification in the late Eocene, *Basin Research*, *26*(5), 621-640, doi:10.1111/bre.12054.

Braucher, R., E. T. Brown, D. L. Bourlès, and F. Colin (2003), In situ produced 10Be measurements at great depths: implications for production rates by fast muons, *Earth and Planetary Science Letters*, *211*(3-4), 251-258, doi:10.1016/S0012-821X(03)00205-X.

Braucher, R., P. Del Castillo, L. Siame, A. J. Hidy, and D. L. Bourlès (2009), Determination of both exposure time and denudation rate from an in situ-produced 10Be depth profile: A mathematical proof of uniqueness. Model sensitivity and applications to natural cases, *Quaternary Geochronology*, *4*(1), 56-67, doi:10.1016/j.quageo.2008.06.001.

Braucher, R., S. Merchel, J. Borgomano, and D. L. Bourlès (2011), Production of cosmogenic radionuclides at great depth: A multi element approach, *Earth and Planetary Science Letters*, *309*(1-2), 1-9, doi:10.1016/j.epsl.2011.06.036.

Brown, E. T., E. J. Brook, G. M. Raisbeck, F. Yiou, and M. D. Kurz (1992), Effective attenuation lengths of cosmic rays producing 10Be AND 26Al in quartz: Implications for exposure age dating, *Geophysical Research Letters*, *19*(4), 369-372, doi:10.1029/92GL00266.

Brown, E. T., J. M. Edmond, G. M. Raisbeck, and F. Yiou (1991), Examination of surface exposure ages of Antarctic moraines using in situ produced 10Be and 26Al. , Geochimica et Cosmochimica Acta, 55(8), 2269-2283, doi:10.1016/0016-7037(91)90103-C.

Burbank, D., A. Meigs, and N. Brozović (1996), Interactions of growing folds and coeval depositional systems, *Basin Research*, *8*(3), 199-223, doi:10.1046/j.1365-2117.1996.00181.x.

Calais, E., A. M. Freed, R. V. Van Arsdale, and S. Stein (2010), Triggering of New Madrid seismicity by late-Pleistocene erosion, *Nature*, *466*, 608-611, doi:10.1038/nature09258.

Cao, K., G.-C. Wang, M. Bernet, P. van der Beek, and K.-X. Zhang (2015), Exhumation history of the West Kunlun Mountains, northwestern Tibet: Evidence for a long-lived, rejuvenated orogen, *Earth and Planetary Science Letters*, *432*, 391-403, doi:10.1016/j.epsl.2015.10.033.

Carretier, S., V. Regard, and C. Soual (2009), Theoretical cosmogenic nuclide concentration in river bed load clasts: Does it depend on clast size?, *Quaternary Geochronology*, *4*(2), 108-123, doi:10.1016/j.quageo.2008.11.004.

Charreau, J., C. Gumiaux, J.-P. Avouac, R. Augier, Y. Chen, L. Barrier, S. Gilder, S. Dominguez, N. Charles, and Q. Wang (2009), The Neogene Xiyu formation, a diachronous prograding gravel wedge at front of the Tianshan: climatic and tectonic implications., *Earth and Planetary Science Letters*, *287*(3-4), 298-310.

Charreau, J., et al. (2017), Denudation outpaced by crustal thickening in the eastern Tianshan, *Earth and Planetary Science Letters*, *479*, 179-191, doi:10.1016/j.epsl.2017.09.025.

Chen, H.-L., Y. Zhang, X. Cheng, X. Lin, H. Deng, X. Shi, Y. Li, H. Wu, C. Li, and S. Yang (2022), Using migrating growth strata to confirm a ~230-km-long detachment thrust in the southern Tarim Basin., *Journal of Structural Geology*, doi:10.1016/j.jsg.2021.104488.

Cheng, H., P. Z. Zhang, C. Spotl, R. L. Edwards, Y. J. Cai, D. Z. Zhang, W. C. Sang, M. Tan, and Z. S. An (2012), The climatic cyclicity in semiarid-arid central Asia over the past 500,000 years., *Geophysical Research Letters*, *39*(L01705), doi:10.1029/2011GL050202.

Cheng, X., H. Chen, X. Lin, L. Wu, and J. Gong (2017), Geometry and kinematic evolution of the Hotan-Tiklik segment of the western Kunlun thrust belt: Constrained by structural analyses and apatite fission track thermochronology, *The Journal of Geology*, *125*(1), 65-82, doi:10.1086/689187.

Chéry, J., S. Carretier, and J.-F. Ritz (2001), Postseismic stress transfer explains time clustering of large earthquakes in Mongolia, *Earth and Planetary Science Letters*, *194*(1-2), 277-286, doi:10.1016/S0012-821X(01)00552-0.

Chéry, J., and P. Vernant (2006), Lithospheric elasticity promotes episodic fault activity, *Earth and Planetary Science Letters*, *243*, 211-217, doi:10.1016/j.epsl.2005.12.014.

Chmeleff, J., F. von Blanckenburg, K. Kossert, and D. Jakob (2010), Determination of the 10Be half-life by multicollector ICP-MS and liquid scintillation counting., *Nuclear Instruments and Methods in Physics Research Section B: Beam Interactions with Materials and Atoms*, *268*(2), 192-199, doi:10.1016/j.nimb.2009.09.012.

Cubas, N., P. Agard, and R. Tissandier (2022), Earthquake ruptures and topography of the Chilean margin controlled by plate interface deformation, *Solid Earth*, *13*(3), 779-792, doi:10.5194/se-13-779-2022.

Dal Zilio, L., Y. van Dinther, T. Gerya, and J. P. Avouac (2019), Bimodal seismicity in the Himalaya controlled by fault friction and geometry, *Nature Communications*, *10*(48), doi:10.1038/s41467-018-07874-8.

Dolan, J. F., D. D. Bowman, and C. G. Sammis (2007), Long-range and long-term fault interactions in Southern California, *Geology*, *35*(9), 855-858, doi:10.1130/G23789A.1.

Dolan, J. F., and B. J. Meade (2017), A Comparison of Geodetic and Geologic Rates Prior to Large Strike-Slip Earthquakes: A Diversity of Earthquake-Cycle Behaviors?, *Geochemistry, Geophysics, Geosystems*, *18*, 4426-4436, doi:10.1002/2017GC007014.

Dubille, M., and J. Lavé (2015), Rapid grain size coarsening at sandstone/conglomerate transition: similar expression in Himalayan modern rivers and Pliocene molasse deposits, *Basin Research*, *27*(1), 26-42, doi:10.1111/bre.12071.

England, P., and G. Houseman (1989), Extension during continental convergence, with application to the Tibetan Plateau, *Journal of Geophysical Research: Solid Earth*, *94*(B12), 17561-17579.

Gosse, J. C., and F. M. Phillips (2001), Terrestrial in situ cosmogenic nuclides: theory and application, *Quaternary Science Reviews*, *20*(14), 1475-1560, doi:10.1016/S0277-3791(00)00171-2.

Grandin, R., M. Vallée, C. Satriano, R. Lacassin, Y. Klinger, M. Simoes, and L. Bollinger (2015), Rupture process of the Mw=7.9 2015 Gorkha earthquake (Nepal): insights into Himalayan megathrust segmentation., *Geophysical Research Letters*, *42*, doi:10.1002/2015GL066044.

Guilbaud, C., M. Simoes, L. Barrier, A. Laborde, J. Van der Woerd, H. Li, P. Tapponnier, T. Coudroy, and A. Murray (2017), Kinematics of active deformation across the Western Kunlun mountain range (Xinjiang, China) and potential seismic hazards within the southern Tarim basin, *Journal of Geophysical Research*, *122*, doi:10.1002/2017JB014069.

Gunderson, K. L., D. J. Anastasio, F. J. Pazzaglia, and K. P. Kodama (2018), Intrinsically Variable Blind Thrust Faulting, *Tectonics*, *37*, 1454-1471, doi:10.1029/2017TC004917.

Hancock, G. S., R. S. Anderson, O. A. Chadwick, and R. C. Finkel (1999), Dating fluvial terraces with 10Be and 26Al profiles: application to the Wind River, Wyoming. , Geomorphology 27, 41-60.

He, P., Q. Wang, K. Ding, M. Wang, X. Qiao, J. Li, Y. Wen, C. Xu, S. Yang, and R. Zou (2016), Source modelof the 2015 Mw 6.4 Pishan earthquake constrained by InSAR and GPS: insight into blind rupture in the western Kunlun Shan., *Geophysical Research Letters*, *43*(4), doi:10.1002/2015GL067140.

Hetzel, R., and A. Hampel (2005), Slip rate variations on normal faults during glacial–interglacial changes in surface loads., *Nature*, *435*, 81-84, doi:10.1038/nature03562.

Hidy, A. J., J. C. Gosse, J. L. Pederson, J. P. Mattern, and R. C. Finkel (2010), A geologically constrained Monte Carlo approach to modeling exposure ages from profiles of cosmogenic nuclides: An example from Lees Ferry, Arizona, *Geochemistry Geophysics Geosystems*, *11*(9), doi:10.1029/2010GC003084.

Hoth, S., A. Hoffmann-Rothe, and N. Kukowski (2007), Frontal accretion: An internal clock for bivergent wedge deformation and surface uplift, *Journal of Geophysical Research*, *112*(B06), doi:10.1029/2006JB004357.

Hubbard, J., R. Almeida, A. Foster, S. N. Sapkota, P. Burgi, and P. Tapponnier (2016), Structural segmentation controlled the 2015 Mw 7.8 Gorkha earthquake rupture in Nepal., *Geology*, *44*(8), 639-642.

Hubbard, J., and J. H. Shaw (2009), Uplift of the Longmen Shan and Tibetan plateau, and the 2008 Wenchuan (M = 7.9) earthquake, *Nature*, *458*(12 March 2009), 194-197.

Jiang, X., Z.-X. Li, and H. Li (2013), Uplift of the West Kunlun Range, northern Tibetan Plateau, dominated by brittle thickening of the upper crust., *Geology*, *41*(4), 439-442.

Jiang, X.-D., and Z.-X. Li (2014), Seismic reflection data support episodic and simultaneous growth of the Tibetan Plateau since 25 Myr, *Nature Communications*, *5*(5453), doi:10.1038/ncomms6453.

Kapp, P., and P. G. DeCelles (2019), Mesozoic–Cenozoic geological evolution of the Himalayan-Tibetan orogen and working tectonic hypotheses, *American Journal of Science*, *319*(3), 159-254.

King, G. C. P., and J. Nabelek (1985), Role of Fault Bends in the Initiation and Termination of Earthquake Rupture, *Science*, *228*(4702), 984-987, doi:10.1126/science.228.4702.98.

Kohl, C. P., and K. Nishiizumi (1992), Chemical isolation of quartz for measurement of in-situ-produced cosmogenic nuclides. , Geochimica et Cosmochimica Acta, 56(9), 3583-3587, doi:10.1016/0016-7037(92)90401-4.

Korschinek, G., et al. (2010), A new value for the half-life of 10Be by Heavy-Ion Elastic Recoil Detection and liquid scintillation counting, *Nuclear Instruments and Methods in Physics Research Section B: Beam Interactions with Materials and Atoms*, *268*(2), 187-191, doi:10.1016/j.nimb.2009.09.020.

Laborde, A., L. Barrier, M. Simoes, H. Li, T. Coudroy, J. van der Woerd, and P. Tapponnier (2019), Cenozoic deformation of the Tarim Basin and surrounding ranges (Xinjiang, China): a regional overview., *Earth Science Reviews*, *197*, 102891, doi:10.1016/j.earscirev.2019.102891.

Lacassin, R., F. Valli, N. Arnaud, P.-H. Leloup, J.-L. Paquette, L. Haibing, P. Tapponnier, M.-L. Chevalier, S. Guillot, and G. Maheo (2004), Large-scale geometry, offset and kinematic evolution of the Karakorum fault, Tibet, *Earth and Planetary Science Letters*, *219*(3-4), 255-269.

Lal, D. (1991), Cosmic ray labeling of erosion surfaces: in situ nuclide production rates and erosion models, *Earth and Planetary Science Letters*, *104*(2-4), 424-439, doi:10.1016/0012-821X(91)90220-C.

Lasserre, C., G. Peltzer, F. Crampé, Y. Klinger, J. van der Woerd, and P. Tapponnier (2005), Coseismic deformation of the 2001 Mw = 7.8 Kokoxili earthquake in Tibet, measured by synthetic aperture radar interferometry, *Journal of Geophysical Research*, *110*(B12408), doi:10.1029/2004JB003500,.

Lavé, J., and J. P. Avouac (2000), Active folding of fluvial terraces across the Siwaliks Hills, Himalayas of central Nepal, *Journal of Geophysical Research*, *105*(B3), 5735-5770.

Li, T., J. Chen, L. Fang, Z. Chen, J. A. Thompson, and C. Jia (2016), The 2015 Mw 6.4 Pishan earthquake: seismic hazards of an active blind wedge thrust system at the Western Kunlun range front, Nothwest Tibetan plateau., *Seismological Research Letters*, *87*(3), doi:10.1785/0220150205.

Liu-Zeng, J., et al. (2009), Co-seismic ruptures of the 12 May 2008, Ms 8.0 Wenchuan earthquake, Sichuan: East–west crustal shortening on oblique, parallel thrusts along the eastern edge of Tibet., *Earth and Planetary Science Letters*, *286*(3-4), 355-370, doi:**10.1016/j.epsl.2009.07.017**.

Long, S. P., and D. M. Robinson (2021), Construction of the Lesser Himalayan–Subhimalayan thrust belt: The primary driver of thickening, exhumation, and high elevations in the Himalayan orogen since the middle Miocene, *Geology*, *49*(11), 1283–1288, doi:10.1130/G48967.1.

Lu, R., X. Xu, D. He, B. Liu, X. Tan, and X. Wang (2016), Co-seismic and blind fault of the 2015 Pishan Mw 6.5 earthquake: implications for the sedimentary-tectonic framework of the western Kunlun mountains, northern Tibetan plateau., *Tectonics*, *35*, 956-964, doi:10.1002/2015TC004053.

Lupker, M., J. Lavé, C. France-Lanord, M. Christl, D. Bourlès, J. Carcaillet, C. Maden, R. Wieler, M. Rahman, and D. Bezbaruah (2017), 10 Be systematics in the Tsangpo-Brahmaputra catchment: the cosmogenic nuclide legacy of the eastern Himalayan syntaxis, *Earth Surface Dynamics*, *5*(3), 429-449, doi:10.5194/esurf-5-429-2017.

Luttrell, K., and D. Sandwell (2010), Ocean loading effects on stress at near shore plate boundary fault systems, *Journal of Geophysical Research*, *115*(B8), doi:10.1029/2009JB006541.

Lyon-Caen, H., and P. Molnar (1984), Gravity anomalies and the structure of Western Tibet and the southern Tarim Basin., *Geophysical Research Letters*, *11*(12), 1251-1254.

Malatesta, L. C., et al. (2017), Lag and mixing during sediment transfer across the Tian Shan piedmont caused by climate-driven aggradation–incision cycles, *Basin Research*, 1-23, doi:10.1111/bre.12267.

Marrero, S. M., F. M. Phillips, B. Borchers, N. Lifton, R. Aumer, and G. Balco (2016), Cosmogenic nuclide systematics and the CRONUScalc program, *Quaternary Geochronology*, *31*, 160-187, doi:10.1016/j.quageo.2015.09.005.

Matte, P., P. Tapponnier, N. Arnaud, L. Bourjot, J. P. Avouac, P. Vidal, L. Qing, P. Yusheng, and W. Yi (1996), Tectonics of Western Tibet, between the Tarim and the Indus., *Earth and Planetary Science Letters*, *142*, 311-330.

Mattern, F., and W. Schneider (2000), Suturing of the Proto-and Paleo-Tethys oceans in the western Kunlun (Xinjiang, China), *Journal of Asian Earth Sciences*, *18*(6), 637-650, doi:10.1016/S1367-9120(00)00011-0.

Menant, A., S. Angiboust, T. Gerya, R. Lacassin, M. Simoes, and R. Grandin (2020), Transient stripping of subducting slabs controls periodic forearc uplift, *Nature Communications*, *11*(1823), doi:10.1038/s41467-020-15580-7.

Meriaux, A.-S., F. J. Ryerson, P. Tapponnier, J. van der Woerd, R. C. Finkel, X. Xu, Z. Xu, and M. W. Caffee (2004), Rapid slip along the central Altyn Tagh Fault: Morphochronologic evidence from Cherchen He and Sulamu Tagh, *Journal of Geophysical Research*, *109*, B06401, doi:10.1029/2003JB002558.

Metivier, F., and Y. Gaudemer (1997), Mass transfer between eastern Tien Shan and adjacent basins (central Asia): constraints on regional tectonics and topography., *Geophysical Journal International*, *128*, 1-17.

MicMac (April 2018) [Software]. https://micmac.ensg.eu/index.php.

Pan, J., H. Li, Z. Sun, J. Pei, J. Si, L. Barrier, J. van der Woerd, Z. Qiu, F. Wu, and L. Zhang (2010), Deformation features of the Mazartagh fold-thrust belt, south central Tarim Basin and ist tectonic significances, *Chinese Journal of Geology (in chinese)*, *45*, 1038-1056.

Peltzer, G., F. Crampé, S. Hensley, and P. Rosen (2001), Transient strain accumulation and fault interaction in the Eastern California shear zone, *Geology*, *29*(11), 975-978, doi:10.1130/0091-7613(2001)029<0975:TSAAFI>2.0.CO;2.

Perrineau, A., J. Van der Woerd, Y. Gaudemer, J. Liu-Zeng, R. Pik, P. Tapponnier, R. Thuizat, and R. Zheng (2011), Incision rate of the Yellow River in Northeastern Tibet constrained by 10Be and 26Al cosmogenic isotope dating of fluvial terraces: implications for catchment evolution and plateau building., Geological Society of London Special Publication, 353, 189-219.

Phillips, R. J., and M. P. Searle (2007), Macrostructural and microstructural architecture of the Karakoram Fault: Relationship between magmatism and strike-slip faulting, *Tectonics*, *26*(3).

Pitard, P., A. Replumaz, M.-L. Chevalier, P.-H. Leloup, M. Bai, M.-P. Doin, C. Thieulot, X. Ou, M. Balvay, and H. Li (2021), Exhumation History Along the Muli Thrust—Implication for Crustal Thickening Mechanism in Eastern Tibet., *Geophysical Research Letters*, *48*(14), e2021GL093677, doi:10.1029/2021GL093677.

Pléiades ESA Archive (January 2018) [Dataset]. https://earth.esa.int/eogateway/missions/pleiades.

Poisson, B., and J. P. Avouac (2004), Holocene hydrological changes inferred from alluvial stream entrenchment in North Tian Shan (Northwestern China), *The Journal of Geology*, *112*(2), 231-249.

Repka, J. L., R. S. Anderson, and R. C. Finkel (1997), Cosmogenic dating of fluvial terraces, Fremont River, Utah, *Earth and Planetary Science Letters*, *152*(1-4), 59-73, doi:10.1016/S0012-821X(97)00149-0.

Replumaz, A., R. Lacassin, P. Tapponnier, and P.-H. Leloup (2001), Large river offsets and Plio-Quaternary dextral slip rate on the Red River fault (Yunnan, China), *Journal of Geophysical Research: Solid Earth*, *106*(B1), 819-836.

Rosu, A.-M., M. Pierrot-Deseilligny, A. Delorme, R. Binet, and Y. Klinger (2015), Measurement of ground displacement from optical satellite image correlation using the free open-source software MicMac, *ISPRS Journal of Photogrammetry and Remote Sensing*, *100*, 48-59.

Royden, L. H., and e. al (1997), Surface deformation and lower crustal flow in eastern Tibet., *Science*, *276*, 788-790.
Rupnik, E., M. Daakir, and M. P. Deseilligny (2017), MicMac–a free, open-source solution for photogrammetry, *Open Geospatial Data, Software and Standards*, *2*(1), 1-9, doi:10.1186/s40965-017-0027-2.
Saint-Carlier, D., J. Charreau, J. Lavé, P.-H. Blard, S. Dominguez, J. P. Avouac, W. Shengli, and A. Team (2016), Major temporal variations in shortening rate absorbed along a large active fold of the southeastern Tianshan piedmont (China), *Earth and Planetary Science Letters*, *434*, 333-348, doi:10.1016/j.epsl.2015.11.041.
Simoes, M., and J.-P. Avouac (2006), Investigating the kinematics of mountain building in Taiwan from the spatiotemporal evolution of the foreland basin and western foothills., *Journal of Geophysical Research*, *111*(B10401), doi:10.1029/2005JB004209.
Simoes, M., J. P. Avouac, and Y.-G. Chen (2007), Slip rates on the Chelungpu and Chushiang thrust faults inferred from a deformed strath terrace along the Dungpuna river, west central Taiwan., *Journal of Geophysical Research*, *112*(B03S10), doi:10.1029/2005JB004200.
Simoes, M., Y.-G. Chen, D. P. Shinde, and A. K. Singhvi (2014), Lateral variations in the long-term slip rate of the Chelungpu fault, Central Taiwan, from the analysis of deformed fluvial terraces., *Journal of Geophysical Research*, *119*, doi:10.1002/2013JB010057.
Sobel, E. R., and T. A. Dumitru (1997), Thrusting and exhumation around the margins of the western Tarim basin during the India-Asia collision, *Journal of Geophysical Research: Solid Earth*, *102*(B3), 5043-5063, doi:10.1029/96JB03267.
Stone, J. O. (2000), Air pressure and cosmogenic isotope production, *Journal of Geophysical Research*, *105*(B10), 23753-23759, doi:10.1029/2000JB900181.
Sun, T., J. Qi, Q. Ni, P. Ma, C. Han, Q. Li, and P. Gong (2019), The influence of syntectonic sedimentation on thrust belt deformation: a kinematic model example from the triangle zone within the Western Kunlun thrust belt, *International Journal of Earth Sciences*, *108*(4), 1121-1136, doi:10.1007/s00531-019-01697-8.
Tapponnier, P., B. Meyer, J. P. Avouac, G. Peltzer, Y. Gaudemer, G. Shunmin, X. Hongfa, Y. Kelun, C. Zhitai, and C. Shuahua (1990), Active thrusting and folding in the Qilian Shan, and decoupling between upper crust and mantle in northeastern Tibet, *Earth and Planetary Science Letters*, *97*(3-4), 382-403.
Tapponnier, P., X. Zhiqin, F. Roger, B. Meyer, N. Arnaud, G. Wittlinger, and Y. Jingsui (2001), Oblique stepwise rise and growth of the Tibet Plateau, *Science*, *294*, 1671-1677.
US Geologigal Survey Earthquake Catalog (January 2024) [Dataset]. https://earthquake.usgs.gov/earthquakes/search/ .
Vallée, M., M. Landès, N. M. Shapiro, and Y. Klinger (2008), The 14 November 2001 Kokoxili (Tibet) earthquake: High-frequency seismic radiation originating from the transitions between sub-Rayleigh and supershear rupture velocity regimes, *Journal of Geophysical Research*, *113*(B7), doi:10.1029/2007JB005520.
Van Der Woerd, J., F. Ryerson, P. Tapponnier, A. S. Meriaux, Y. Gaudemer, B. Meyer, R. Finkel, M. Caffee, Z. Guoguang, and X. Zhiqin (2000), Uniform slip-rate along the Kunlun Fault: Implications for seismic behaviour and large-scale tectonics, *Geophysical Research Letters*, *27*(16), 2353-2356.
Wallace, R. E. (1987), Grouping and migration of surface faulting and variations in slip rates on faults in the Great Basin province, *Bulletin of the Seismological Society of America*, *77*(3), 868-876, doi:10.1785/BSSA0770030868.
Wang, C.-Y., H.-L. Chen, X.-G. Cheng, and K. Li (2013), Evaluating the role of syn-thrusting sedimentation and interaction with frictional detachment in the structural evolution of the SW Tarim Basin, NW China: insights from analogue modeling., *Tectonophysics*, *608*, 642-652.
Wang, E., J. Wan, and J. Liu (2003), Late Cenozoic geological evolution of the foreland basin bordering the West Kunlun range in Pulu area: Constraints on timing of uplift of northern margin of the Tibetan Plateau, *Journal of Geophysical Research: Solid Earth*, *108*(B8), doi:10.1029/2002JB001877.
Wang, H., M. Liu, J. Cao, X. Shen, and G. Zhang (2011), Slip rates and seismic moment deficits on major active faults in mainland China., *Journal of Geophysical Research*, *116*(B02405), doi:10.1029/2010JB007821.
Wei, H.-H., Q.-R. Meng, L. Ding, and Z.-Y. Li (2013), Tertiary evolution of the western Tarim basin, northwest China: a tectono-sedimentary response to northward indentation of the Pamir salient., *Tectonics*, *32*, 558-575, doi:10.1002/tect20046.
Weldon, R. J. (1986), The Late Cenozoic Geology of Cajon Pass; Implications for Tectonics and Sedimentation along the San Andreas Fault., California Institute of Technology, Pasadena, CA.
Wen, Y., C. Xu, Y. Liu, and G. Jiang (2016), Deformation and source parameters of the 2015 Mw 6.5 earthquake in Pishan, Western Chine, from Sentinel-1A and ALOS-2 data., *Remote Sensing*, *8*(134), doi:10.3390/rs8020134.
Wesnousky, S. G. (2006), Predicting the endpoints of earthquake ruptures, *Nature*, *444*, 358-360, doi:10.1038/nature05275.

Wittlinger, G., J. Vergne, P. Tapponnier, V. Farra, G. Poupinet, M. Jiang, H. Su, G. Herquel, and A. Paul (2004), Teleseismic imaging of subducting lithosphere and Moho offsets beneath western Tibet., *Earth and Planetary Science Letters*, *221*, 117-130.

Xu, J., J. Chen, R. Arrowsmith, T. Li, B. Zhang, N. Di, and W. Pang (2020), Growth model and tectonic significance of the Guman fold along the Western Kunlun Mountain Front (Xinjiang, China) derived from terrace deformation and seismic data, *Frontiers in Earth Science*, *8*, 485, doi:10.3389/feart.2020.590043.

Xu, X., X. Wen, G. Yu, G. Chen, Y. Klinger, J. Hubbard, and J. H. Shaw (2009), Coseismic reverse- and oblique-slip surface faulting generated by the 2008 Mw 7.9 Wenchuan earthquake, China *Geology*, *37*(6), 515-518, doi:10.1130/G25462A.1.

Yang, Y., C.-Q. Liu, J. van der Woerd, S. Xu, L.-F. Cui, Z.-Q. Zhao, Q.-L. Wang, G.-D. Jia, and F. Chabaux (2019), New constraints on the late Quaternary landscape evolution of the eastern Tibetan Plateau from 10Be and 26Al in-situ cosmogenic nuclides, *Quaternary Science Reviews*, *220*, 244-262, doi:10.1016/j.quascirev.2019.07.020.

Yin, A., Y.-Q. Dang, L.-C. Wang, W.-M. Jiang, S.-P. Zhou, X.-H. Chen, G. E. Gehrels, and M. W. McRivette (2008), Cenozoic tectonic evolution of Qaidam basin and its surrounding regions (Part 1): The southern Qilian Shan-Nan Shan thrust belt and northern Qaidam basin, *Geological Society of America Bulletin*, *120*(7-8), 813-846.

Yin, A., and T. M. Harrison (2000), Geologic evolution of the Himalayan-Tibetan orogen, *Annual review of earth and planetary sciences*, *28*(1), 211-280.

Zhang, P. Z., P. Molnar, and X. Xu (2007), Late Quaternary and present-day rates of slip along the Altyn Tagh Fault, northern margin of the Tibetan Plateau., *Tectonics*, *26*, TC5010, doi:doi:10.1029/2006TC002014.

Zhang, Y., H. Chen, X. Shi, R. Almeida, R. Walker, X. Lin, X. Cheng, H. Deng, Z. Chen, and X. Hu (2023), Reconciling patterns of long-term topographic growth with coseismic uplift by synchronous duplex thrusting., *Nature Communications*, *14*, 8073, doi:10.1038/s41467-023-43994-6.

Zheng, H., X. Wei, R. Tada, P. D. Clift, B. Wang, F. Jourdan, P. Wang, and M. He (2015), Late Oligocene - early Miocene birth of the Taklimakan Desert., *Proceedings of the National Academy of Science*, *112*(25), 7662-7667.

Zuza, A. V., X. Cheng, and A. Yin (2016), Testing models of Tibetan Plateau formation with Cenozoic shortening estimates across the Qilian Shan–Nan Shan thrust belt, *Geosphere*, *12*(2), 501-532.

Tectonics, https://doi.org/10.1029/2024TC008284

Supporting Information for

Kinematics of Active Deformation and Possible Segmentation of Seismic Slip along the Foothills of the Western Kunlun (China).

C. Guilbaud[1], M. Simoes[1], J. Van der Woerd[2], G. Baby[1,3], L. Barrier[1], H. Li[4,5], and J. Pan[4,5]

[1] Université Paris Cité, Institut de physique du globe de Paris, CNRS, F-75005 Paris, France

[2] Université de Strasbourg, CNRS, ENGESS, Institut Terre et Environnement de Strasbourg, UMR 7063, F-67000 Strasbourg, France.

[3] Physical Science and Engineering Division, King Abdullah University of Science and Technology, Thuwal, Saudi Arabia

[4] Key Laboratory of Continental Dynamics of Ministry of Natural Resources, Institute of Geology, Chinese Academy of Geological Sciences, 100037 Beijing, China

[5] Jiangsu Donghai Continental Deep Borehole Crustal Activity National Observation and Research Station, 222300 Jiangsu, China

Contents of this file

Additional Supporting Information (Files uploaded separately)

Introduction

This file contains additional information on the geomorphology of the Karakash River (Figure S1), analytical procedures followed to analyze collected samples (Text S1 and Table 2), accompanied by a table with complete analytical data on each sample (Table S1, uploaded separately). Further details on the age inversion procedures and models are provided (Text S2), and possible trade-offs between inverted parameters are illustrated by additional figures (Figures S2 to S9).

Figure S1. Long-distance profile of the Karakash river

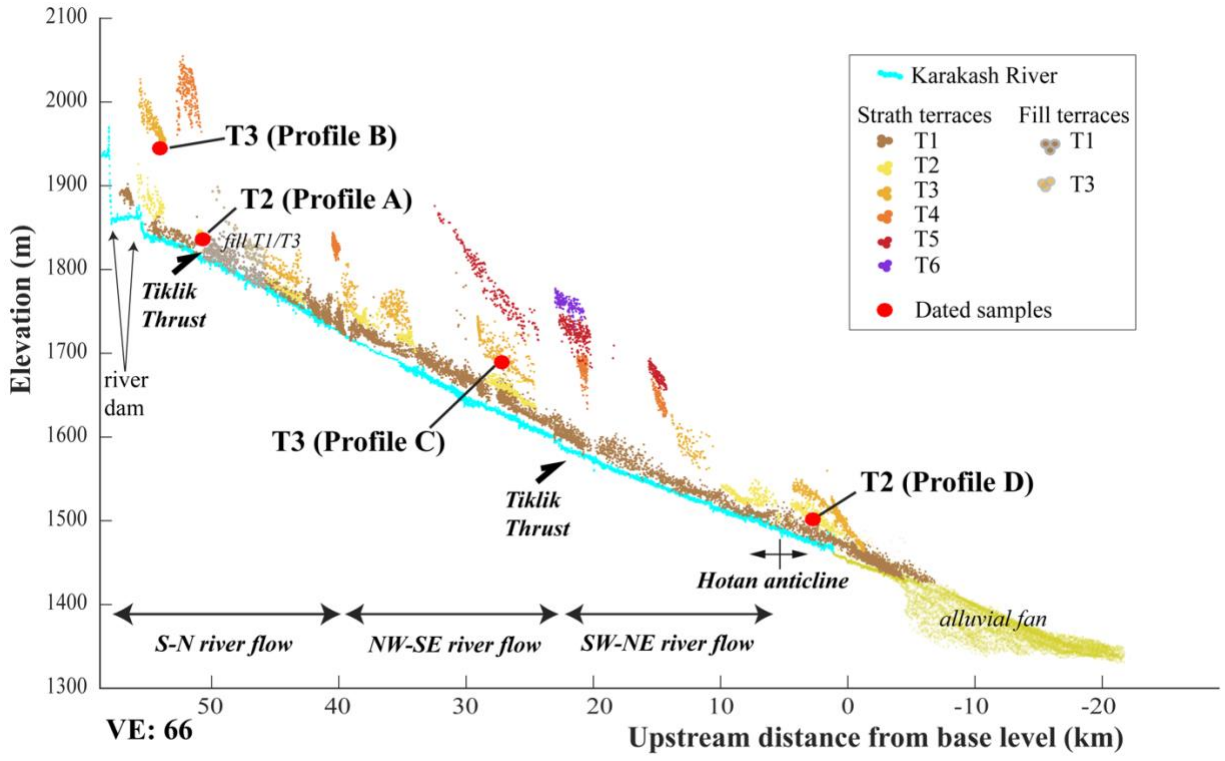

Figure S1. Long-distance profile of the Karakash River and associated terraces. Distances are indicated upstream from base level. Terrace levels are color-coded as in the map of Figure 5 and profiles of Figure 6. Location of sampled depth profiles (A to D) are reported together with correlated terrace levels. Various structural features encountered along the Karakash River course are reported for reference.

Text S1. Analytical procedures

Samples have been prepared and analyzed in the course of several years (2006 to 2020, after field campaigns in 2003, 2005, 2017 and 2019), in different laboratories (see Table S1 for analytical details), including *Institut Terre et Environnement de Strasbourg* (ITES, Strasbourg, France), *Centre Européen de Recherche et d'Enseignement des Géosciences de l'Environnement* (CEREGE, Aix-en-Provence, France) and *Purdue Rare Isotope Measurement Laboratory* (PRIME Lab, Purdue University, USA). These laboratories have different quartz isolation and purification protocols that we briefly describe below.

To isolate the quartz-rich fraction contained in the samples, all samples were crushed, sieved, and leached in concentrated hydrochloric acid. Quartz is then isolated and purified by several low concentrated fluoric and nitric acid leaches (at ITES and PRIME Lab) or hydrochloric and hexafluoric acid leaches followed by sequential fluoric acid leaches (CEREGE). This is to dissolve aluminum-rich feldspar minerals, etch the exterior portion of the quartz crystals in order to remove atmospheric ^{10}Be adsorbed on the mineral surfaces, and reduce the total amount of aluminum Al [*Brown et al.*, 1991; *Gosse and Phillips*, 2001; *Kohl and Nishiizumi*, 1992].

About 0.2-0.5 mg of ^{9}Be carrier was added to the purified quartz that was then dissolved in concentrated fluoric acid. Preparing the samples for ^{26}Al measurements implied that after dissolution, total Al was measured in the sample solutions. ^{27}Al carrier is then added if the total mass of Al is less than 2 mg. Nuclides were then chemically separated using ion exchange columns. After precipitation, $Be(OH)_2$ and $Al_2(OH)_3$ were heated at 750°C to obtain BeO and Al_2O_3.

The ^{10}Be/^{9}Be and ^{26}Al/^{27}Al ratios were then measured at ASTER (CEREGE), except for 2 samples (KA03-1A and KA03-1B) that were measured at the *Center for Accelerator Mass Spectrometry* at *Lawrence Livermore National Laboratory* (CAMS – LLNL, Livermore, USA) (see Table S1). Finally, the ratios were converted to ^{10}Be or ^{26}Al concentrations using the measured total Be or Al concentrations prior to chemical separation (Tables 1 and S1). As we do not have ^{26}Al/^{27}Al ratios for all samples, only those available are presented in Tables 1 and S1. They provide additional information on the quality of the analytical processing and can help point out possible exposure complexities (see main text).

The obtained AMS ratios were overall at least one order of magnitude larger than those of the analytical blanks (Table S1). It is therefore unlikely that large errors were introduced due to the processing of the various samples in different laboratories.

Table S1 (uploaded separately). Complete sampling and analytical data for all the samples collected in depth profiles A to D. These data are provided in an accompanying Excel file, where the first sheet (*Table Notice*) provides additional information on some of the columns of the second sheet (*Data*) where all data are reported. See Figure 5 for location of samples, and Figure 7 for a representation of concentrations of in-situ produced ^{10}Be along all depth-profiles. A simplified version of this table is provided in the main text (Table 1).

Text S2. Profile inversions and age interpretations.

In this study, we used the time constant scaling scheme "St" [*Lal*, 1991; *Stone*, 2000] with a production rate of 4.01±0.33 atoms/g/yr at sea level and at high latitudes to constrain the local ^{10}Be production rate at our study site. We use here the CRONUS-Earth online calculator (v3, last consulted on December 2022; http://hess.ess.washington.edu/math/v3/v3_age_in.html) (e.g. [*Balco et al.*, 2008; *Borchers et al.*, 2016; *Marrero et al.*, 2016]), and find values ranging from 11.87 (profile D) to 16.17 atoms/g/yr (profile B). Assuming the present river base level to represent the topographic level at the beginning of folding, taking into account the time-changing elevation of the sampled sites, those rates drop to values ranging from 11.71 to 14.94 atoms/g/yr, respectively. To model the data, we used attenuation lengths of ~160, 1500 and 4320 g/cm^2 for neutrons, slow muons and fast muons, respectively [*Balco*, 2017; *Braucher et al.*, 2011; *Marrero et al.*, 2016].

Before inverting for the ages of each depth profile, we determined the density to be used for modeling (e.g., [*Ackerer et al.*, 2016; *Hancock et al.*, 1999; *Perrineau et al.*, 2011]). Although the four terraces we sampled belong to the same river system and are distributed over a relatively small area, they have somewhat different granulometries, ranging from cobbles to sand (see Figure 7). Densities were measured in the lab or in the field for each profile, as well as estimated by in-depth cross-section photograph analyses and/or by inverting our sample concentrations as a function of depth (Table S2). Based on these estimates, we decided to use a constant density of 2.3 for the profiles mostly comprised of cobbles and pebbles (profiles A, B and C) and a density of 1.6 for the remaining profile (D) mostly comprised of sand and smaller gravels.

Sampled profiles (terrace level)	Measured density (laboratory/field)	Estimated density (profile analysis from photographs)	Estimated density (inversion of concentration profiles)	Density used in age inversions
A (T2)	-	2.37-2.25-2.21	2.5	2.3
B (T3)	-	2.62-2.59-2.58	2.0	2.3
C (T3)	2.34	2.37-2.25-2.21	2- 2.2	2.3
D (T2)	1.6	-	1.3-1.5	1.6

Table S2. Densities measured and/or estimated for each depth profile, and values considered in our age inversions.

We then modelled our profiles using two different approaches:

- A first model (Model 1), with a fixed erosion value set at 0.001 mm/yr (or 1 mm/kyr) corresponding to a local long-term estimate (sample at saturation for more than 1 Myr) on a nearby drainage basin (see [*Guilbaud et al.*, 2017]) and a constant

density. The two remaining parameters (age and inheritance) are then inverted in a specific range of values (see Table 2). The best solution is a parameter couple of age and inheritance, which displays the minimum chi-squared value (Figures S2-S5). Results from this model are favored in our interpretations.

- A second model (Model 2), with all three parameters (age, erosion, inheritance) inverted in a specific range of values (see Table 2) and a constant density. In this case, the best solution determined is therefore a combination of age, inheritance, and erosion, which displays the minimum chi-squared value (Figures S6-S9). Results from this model are mostly considered as informative of the space of possible solutions and of possible parameter trade-offs.
- Errors for each parameter are computed for error yields of 2-sigma (blue zone in Figures S2-S9), 1-sigma (green zone in Figures S2-S9) and χ^2min+1 (yellow zone in Figures S2-S9, a criterium classically used in age inversions (e.g., [*Yang et al.*, 2019]). Additional details on these inversions are illustrated in Figures S2 to S9.

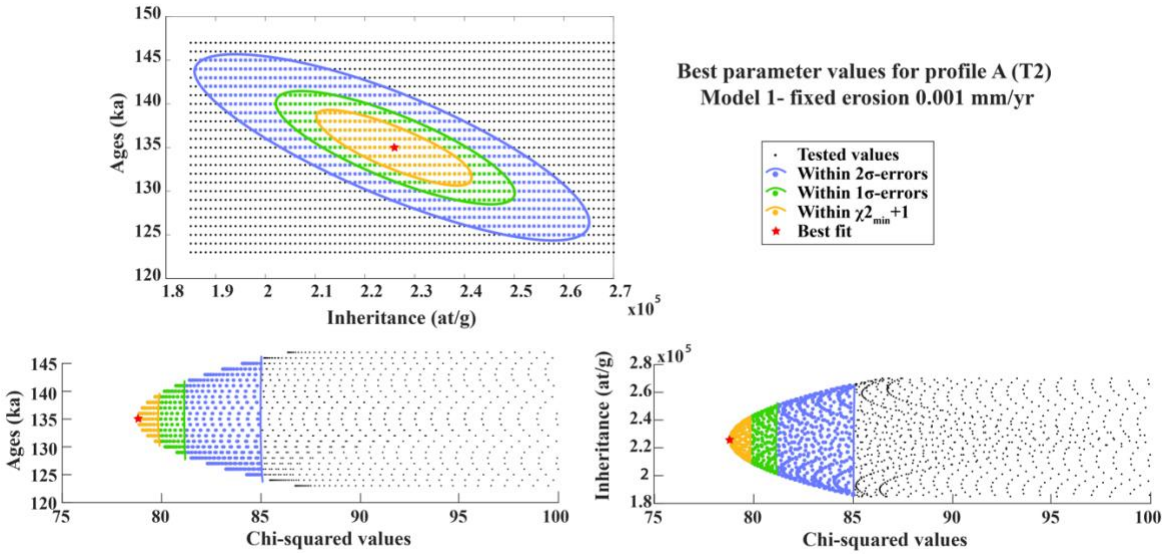

Figure S2. Inversion results for depth-profile A (interpreted as related to terrace level T2), in the case of Model 1 (fixed erosion). Age and inheritance are inverted and the solution is represented by the red star. Various confidence intervals are represented by different colored areas. Top left: trade-off between age and inheritance. Bottom: calculated χ^2 for the explored range of ages (left) and inheritance (right).

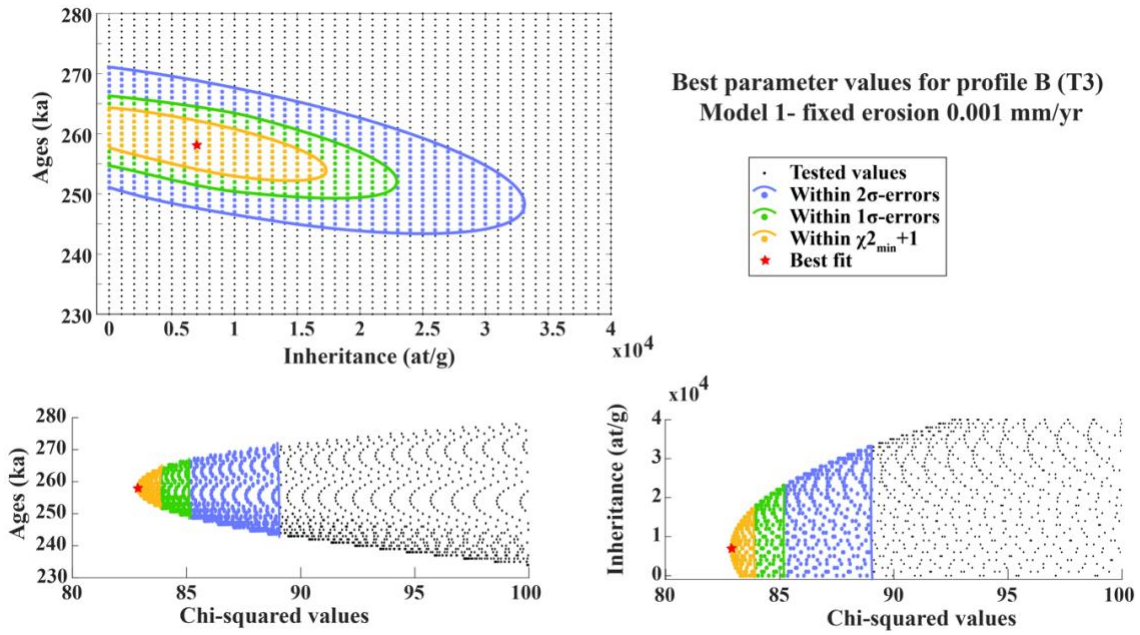

Figure S3. Inversion results for depth-profile B (interpreted as related to terrace level T3), in the case of Model 1 (fixed erosion). Age and inheritance are inverted and the solution is represented by the red star.
Various confidence intervals are represented by different colored areas. Top left: trade-off between age and inheritance. Bottom: calculated χ^2 for the explored range of ages (left) and inheritance (right).

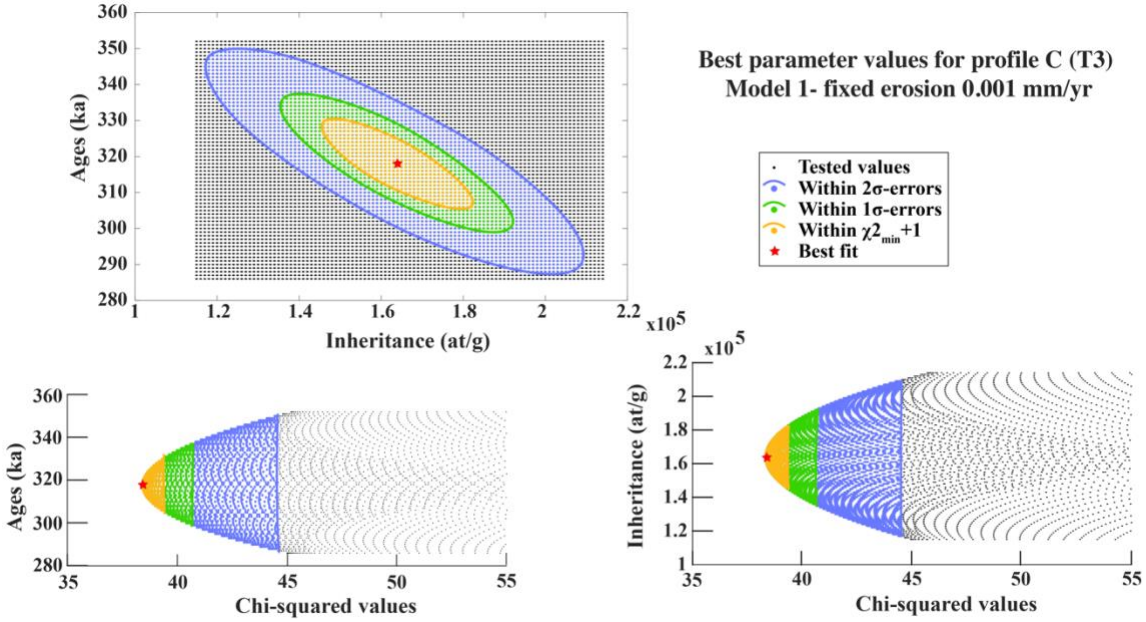

Figure S4. Inversion results for depth-profile C (interpreted as related to terrace level T3), in the case of Model 1 (fixed erosion). Age and inheritance are inverted and the solution is represented by the red star. Various confidence intervals are represented by different colored areas. Top left: trade-off between age and inheritance. Bottom: calculated χ^2 for the explored range of ages (left) and inheritance (right).

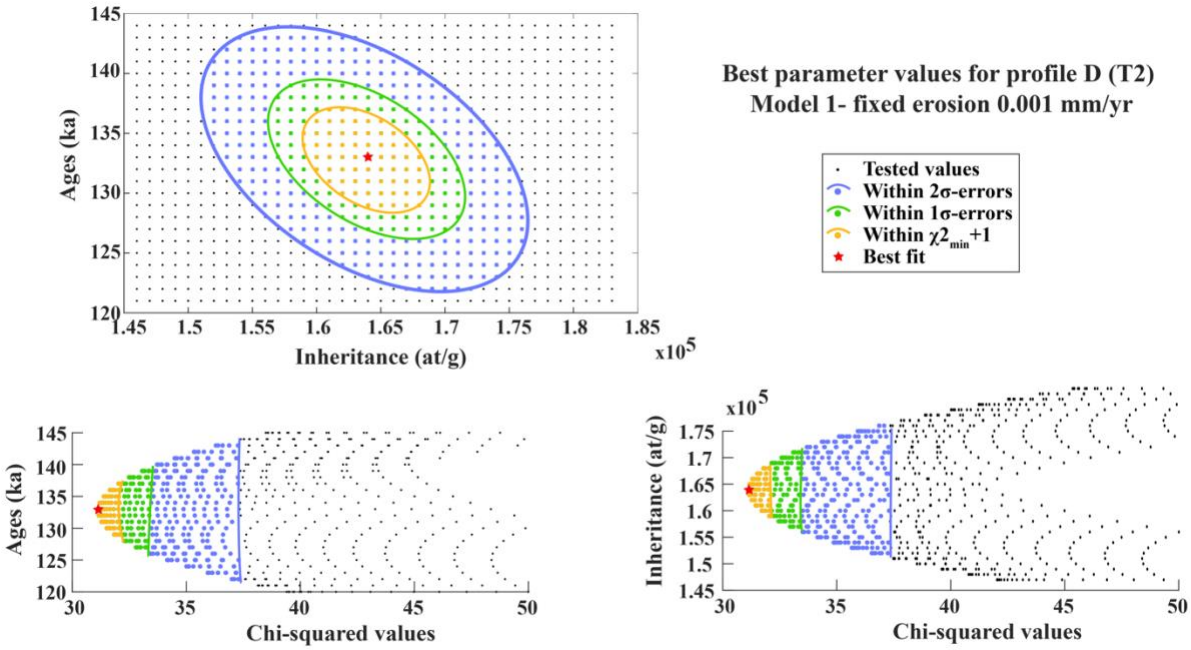

Figure S5. Inversion results for depth-profile D (interpreted as related to terrace level T2), in the case of Model 1 (fixed erosion). Age and inheritance are inverted and the

solution is represented by the red star. Various confidence intervals are represented by different colored areas. Top left: trade-off between age and inheritance. Bottom: calculated χ^2 for the explored range of ages (left) and inheritance (right).

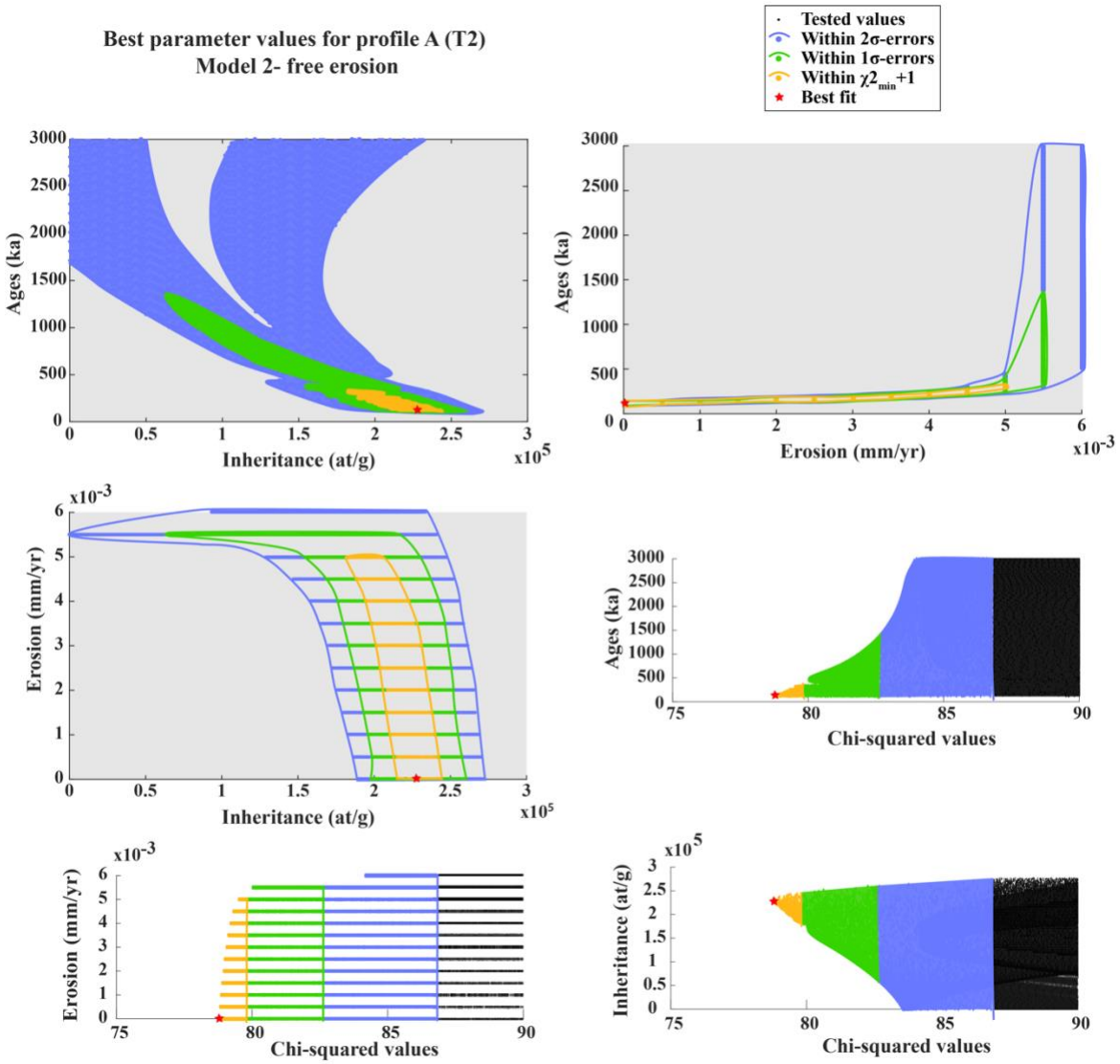

Figure S6. Inversion results for depth-profile A (interpreted as related to terrace level T2), in the case of Model 2. Erosion, age, and inheritance are inverted, and the best solution is represented by the red star. Various confidence intervals are represented by different colored areas. From top to bottom, and from left to right:
* Top left panels: trade-offs between parameters, as illustrated in 2-dimensions for an easier reading (age vs. inheritance, age vs. erosion, and erosion vs. inheritance).
* Bottom right panels: calculated χ^2 for the explored range of ages, erosion, and inheritance.

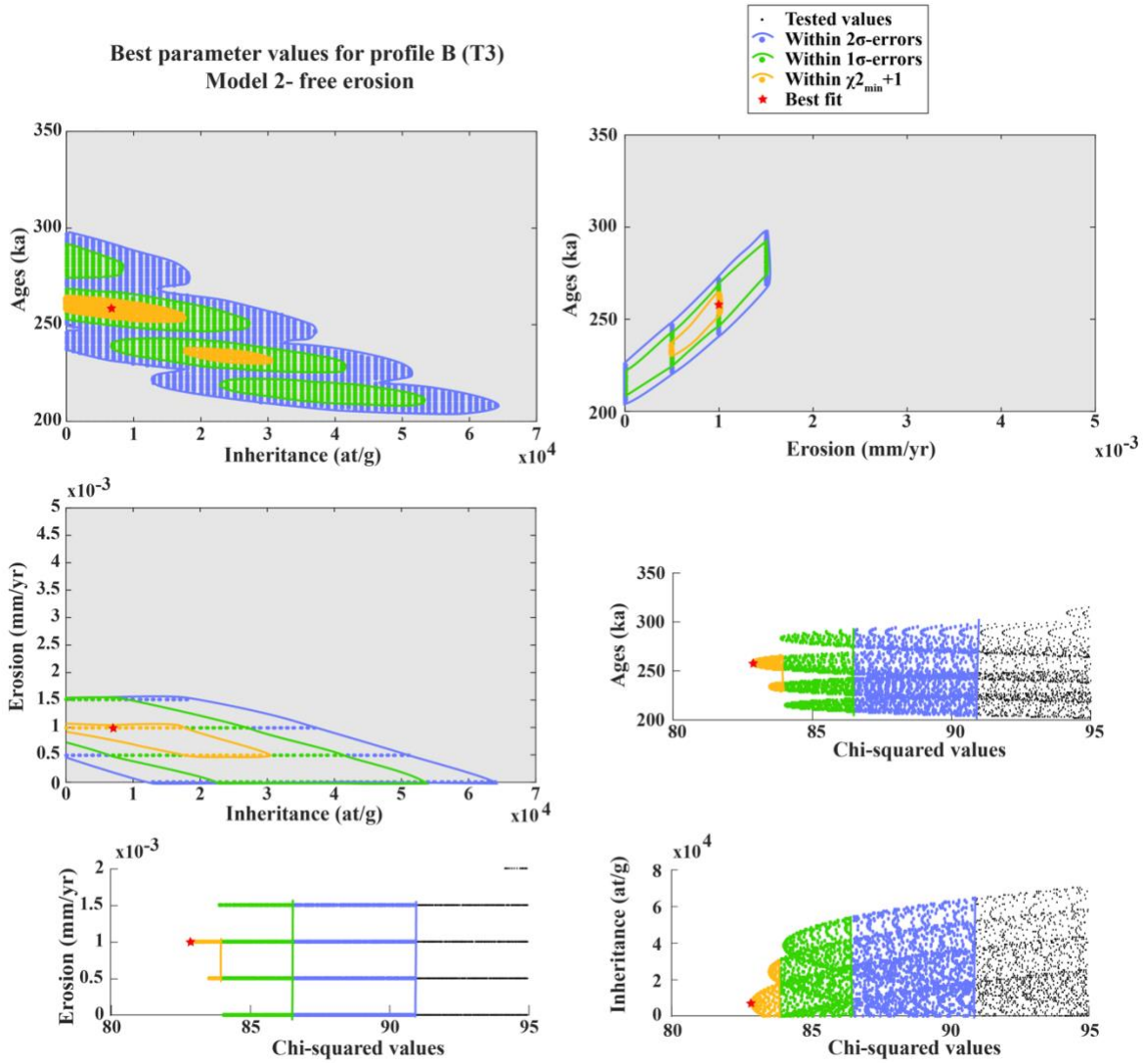

Figure S7. Inversion results for depth-profile B (interpreted as related to terrace level T3), in the case of Model 2. Erosion, age, and inheritance are inverted, and the best solution is represented by the red star. Various confidence intervals are represented by different colored areas. From top to bottom, and from left to right:

* Top left panels: trade-offs between parameters, as illustrated in 2-dimensions for an easier reading (age vs. inheritance, age vs. erosion, and erosion vs. inheritance).

* Bottom right panels: calculated χ^2 for the explored range of ages, erosion, and inheritance.

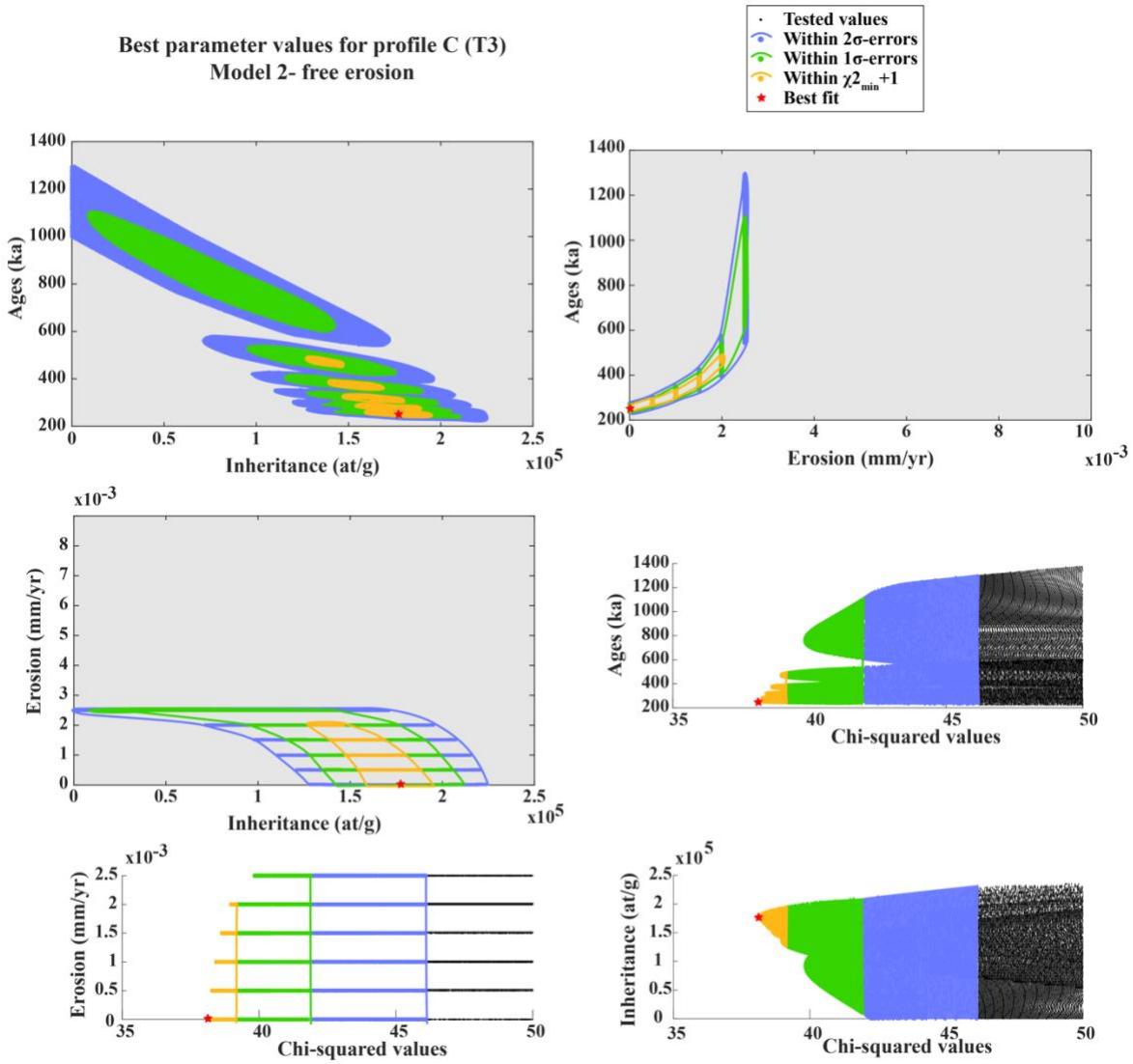

Figure S8. Inversion results for depth-profile C (interpreted as related to terrace level T3), in the case of Model 2. Erosion, age, and inheritance are inverted, and the best solution is represented by the red star. Various confidence intervals are represented by different colored areas. From top to bottom, and from left to right:
* Top left panels: trade-offs between parameters, as illustrated in 2-dimensions for an easier reading (age vs. inheritance, age vs. erosion, and erosion vs. inheritance).
* Bottom right panels: calculated χ^2 for the explored range of ages, erosion, and inheritance.

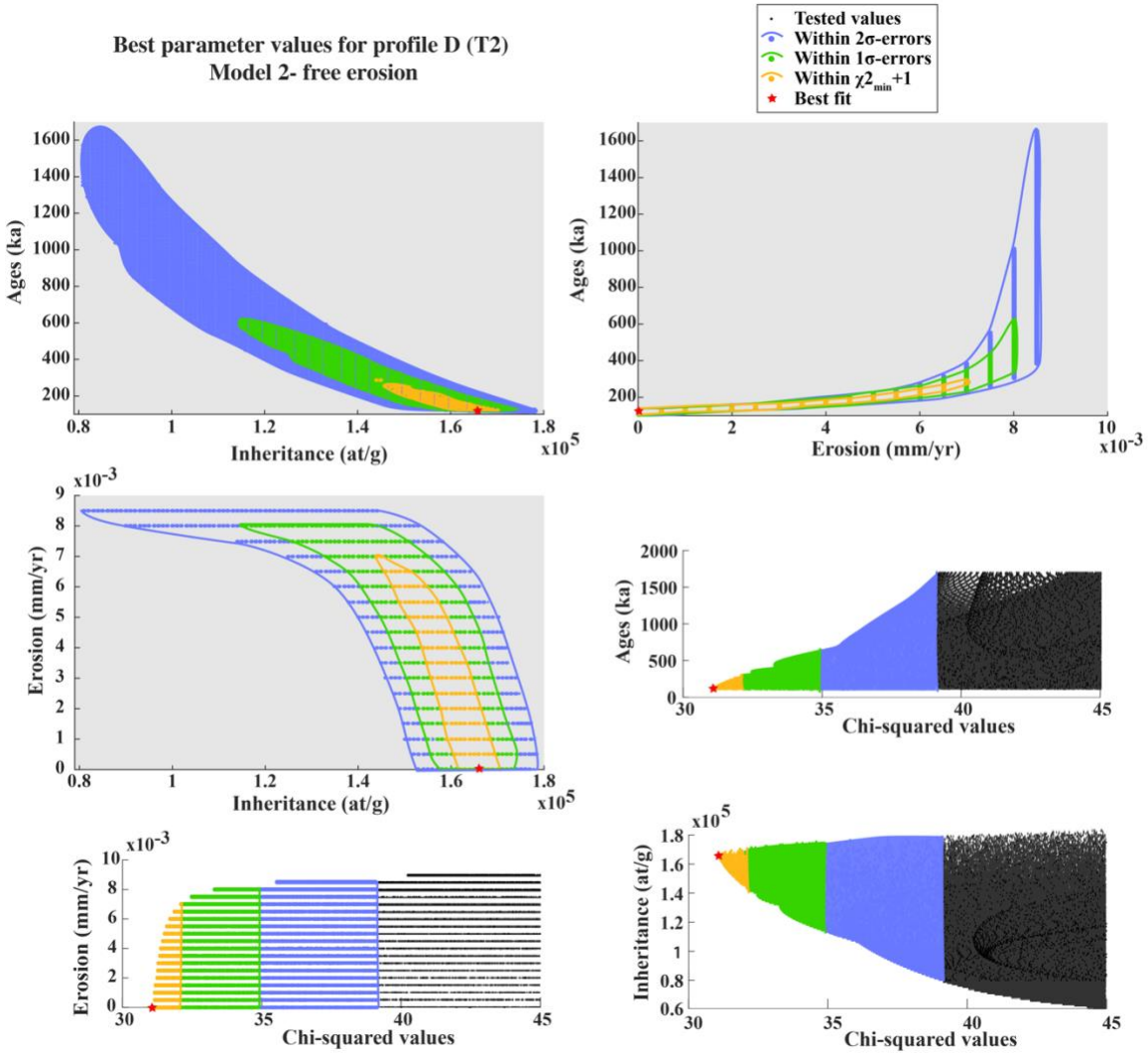

Figure S9. Inversion results for depth-profile D (interpreted as related to terrace level T2), in the case of Model 2. Erosion, age, and inheritance are inverted, and the best solution is represented by the red star. Various confidence intervals are represented by different colored areas. From top to bottom, and from left to right:
* Top left panels: trade-offs between parameters, as illustrated in 2-dimensions for an easier reading (age vs. inheritance, age vs. erosion, and erosion vs. inheritance).
* Bottom right panels: calculated χ^2 for the explored range of ages, erosion, and inheritance.

References

Ackerer, J., F. Chabaux, J. Van der Woerd, D. Viville, E. Pelt, E. Kali, C. Lerouge, P. Ackerer, R. di Chiara Roupert, and P. Ne Grel (2016), Regolith evolution on the millennial timescale from combined UeTheRa isotopes and in situ cosmogenic 10Be analysis in a weathering profile (Strengbach catchment, France), Earth and Planetary Science Letters, 453, 33-43.

Balco, G. (2017), Production rate calculations for cosmic-ray-muon-produced 10Be and 26Al benchmarked against geological calibration data, Quaternary Geochronology, 39, 150-173, doi:10.1016/j.quageo.2017.02.001.

Balco, G., J. O. Stone, N. A. Lifton, and T. J. Dunai (2008), A complete and easily accessible means of calculating surface exposure ages or erosion rates from 10Be and 26Al measurements., Quaternary Geochronology, 3, 174-195.

Borchers, B., S. Marrero, G. Balco, M. Caffee, B. Goehring, N. Lifton, K. Nishiizumi, F. Phillips, J. Schaefer, and J. Stone (2016), Geological calibration of spallation production rates in the CRONUS-Earth project, Quaternary Geochronology, 31, 188-198, doi:10.1016/j.quageo.2015.01.009.

Braucher, R., S. Merchel, J. Borgomano, and D. L. Bourlès (2011), Production of cosmogenic radionuclides at great depth: A multi element approach, Earth and Planetary Science Letters, 309(1-2), 1-9, doi:10.1016/j.epsl.2011.06.036.

Brown, E. T., J. M. Edmond, G. M. Raisbeck, and F. Yiou (1991), Examination of surface exposure ages of Antarctic moraines using in situ produced 10Be and 26Al. , Geochimica et Cosmochimica Acta, 55(8), 2269-2283, doi:10.1016/0016-7037(91)90103-C.

Gosse, J. C., and F. M. Phillips (2001), Terrestrial in situ cosmogenic nuclides: theory and application, Quaternary Science Reviews, 20(14), 1475-1560, doi:10.1016/S0277-3791(00)00171-2.

Guilbaud, C., M. Simoes, L. Barrier, A. Laborde, J. Van der Woerd, H. Li, P. Tapponnier, T. Coudroy, and A. Murray (2017), Kinematics of active deformation across the Western Kunlun mountain range (Xinjiang, China) and potential seismic hazards within the southern Tarim basin, Journal of Geophysical Research, 122, doi:10.1002/2017JB014069.

Hancock, G. S., R. S. Anderson, O. A. Chadwick, and R. C. Finkel (1999), Dating fluvial terraces with 10Be and 26Al profiles: application to the Wind River, Wyoming. , Geomorphology 27, 41-60.

Kohl, C. P., and K. Nishiizumi (1992), Chemical isolation of quartz for measurement of in-situ-produced cosmogenic nuclides. , Geochimica et Cosmochimica Acta, 56(9), 3583-3587, doi:10.1016/0016-7037(92)90401-4.

Lal, D. (1991), Cosmic ray labeling of erosion surfaces: in situ nuclide production rates and erosion models, Earth and Planetary Science Letters, 104(2-4), 424-439, doi:10.1016/0012-821X(91)90220-C.

Marrero, S. M., F. M. Phillips, B. Borchers, N. Lifton, R. Aumer, and G. Balco (2016), Cosmogenic nuclide systematics and the CRONUScalc program, Quaternary Geochronology, 31, 160-187, doi:10.1016/j.quageo.2015.09.005.

Perrineau, A., J. Van der Woerd, Y. Gaudemer, J. Liu-Zeng, R. Pik, P. Tapponnier, R. Thuizat, and R. Zheng (2011), Incision rate of the Yellow River in Northeastern Tibet constrained by 10Be and 26Al cosmogenic isotope dating of fluvial terraces: implications for catchment evolution and plateau building., Geological Society of London Special Publication, 353, 189-219.

Stone, J. O. (2000), Air pressure and cosmogenic isotope production, Journal of Geophysical Research, 105(B10), 23753-23759, doi:10.1029/2000JB900181.

Yang, Y., C.-Q. Liu, J. van der Woerd, S. Xu, L.-F. Cui, Z.-Q. Zhao, Q.-L. Wang, G.-D. Jia, and F. Chabaux (2019), New constraints on the late Quaternary landscape evolution of the eastern Tibetan Plateau from 10Be and 26Al in-situ cosmogenic nuclides, Quaternary Science Reviews, 220, 244-262, doi:10.1016/j.quascirev.2019.07.020.